Prepapration, Applications and Structural Determination of Nano-porous Materials (II)

Soofin Cheng (鄭 淑 芬)

Department of Chemistry, National Taiwan University
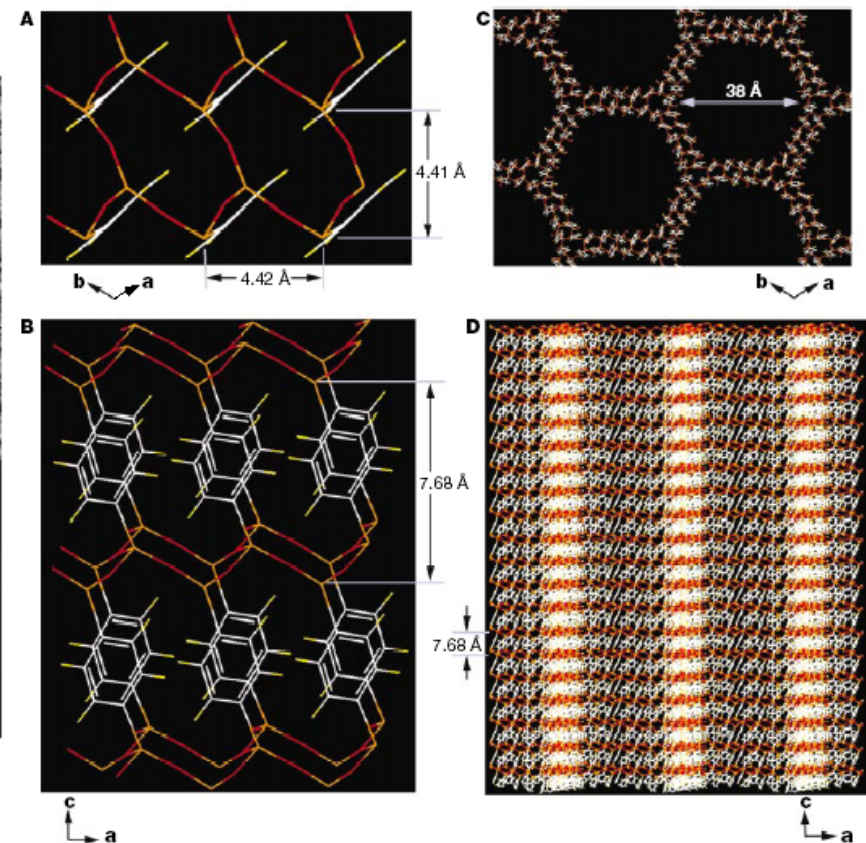
台灣大學化學系

Email: chem1031@ntu.edu.tw

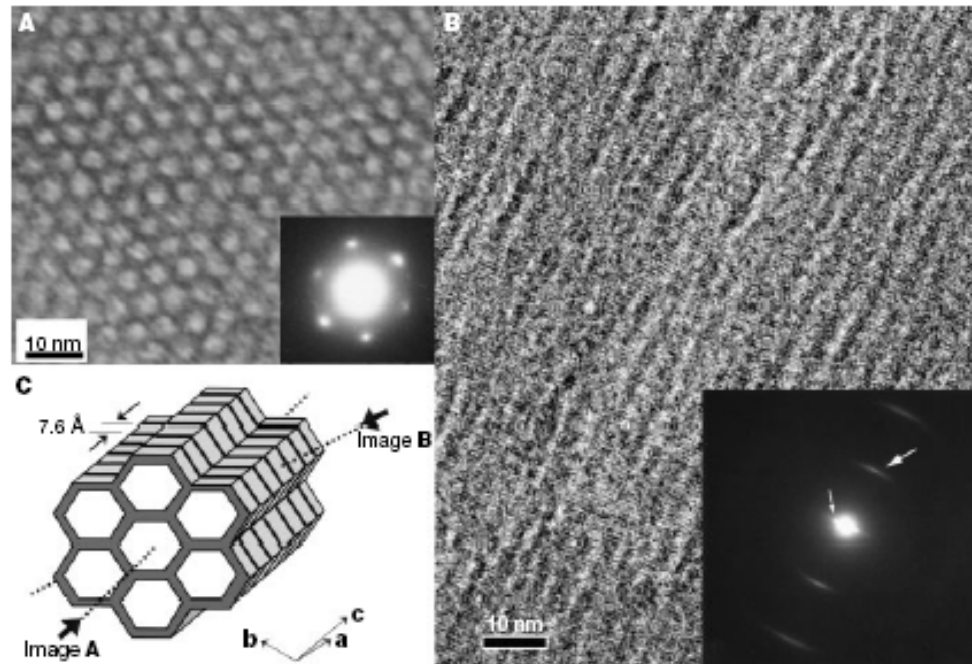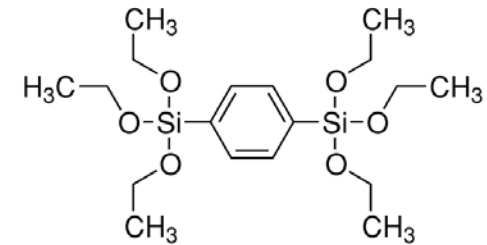# Can Nono-porous Materials be Made of Compounds Other than Silica

An ordered mesoporous organosilica hybrid material with a crystal-like wall structure

Shinji Inagaki*, Shiyou Guan*†, Tetsu Ohsuna‡ & Osamu Terasaki§

Nature, 416 (2002) 304

Figure 3 Structural models of mesoporous benzene–silica. **A, B,** Images of the layered arrangement of $SiO_{1.5}$–C_6H_4–$SiO_{1.5}$ units in the walls. The structure was optimized by minimizing the three-dimensional periodic lattice using the force field COMPASS. **C, D,** Images of the hexagonal lattice constructed with the layered pore-wall structure.

3
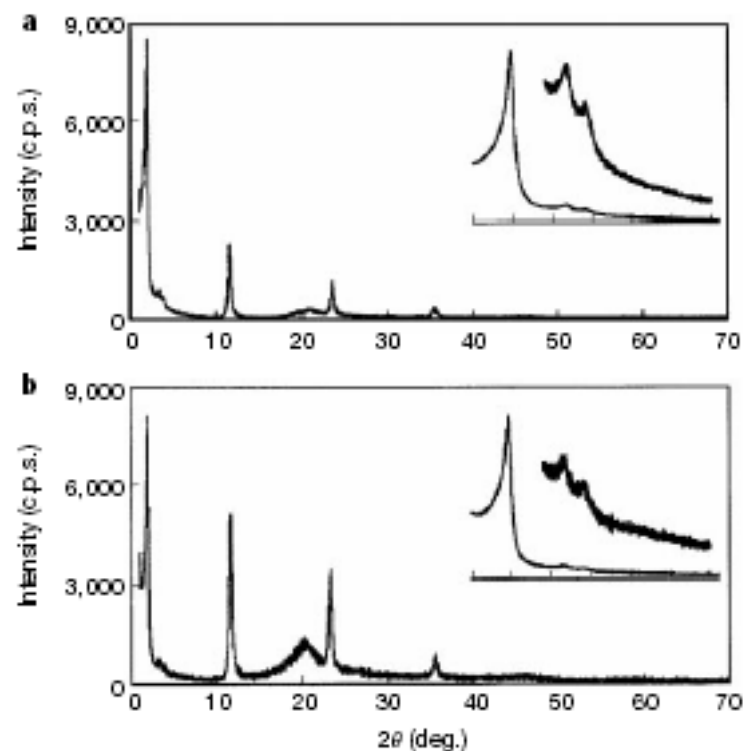
Figure 1 Powder X-ray diffraction patterns of mesoporous benzene–silicas. **a**, Material after removal of surfactants. **b**, As-made material containing surfactants. Patterns in the low-angle region ($1 < 2\theta < 7$) are shown magnified in the insets. These materials have both mesoscale ($d = 45.5$, 26.0 and 22.9 Å) and molecular-scale ($d = 7.6$, 3.8 and 2.5 Å) periodic structures.
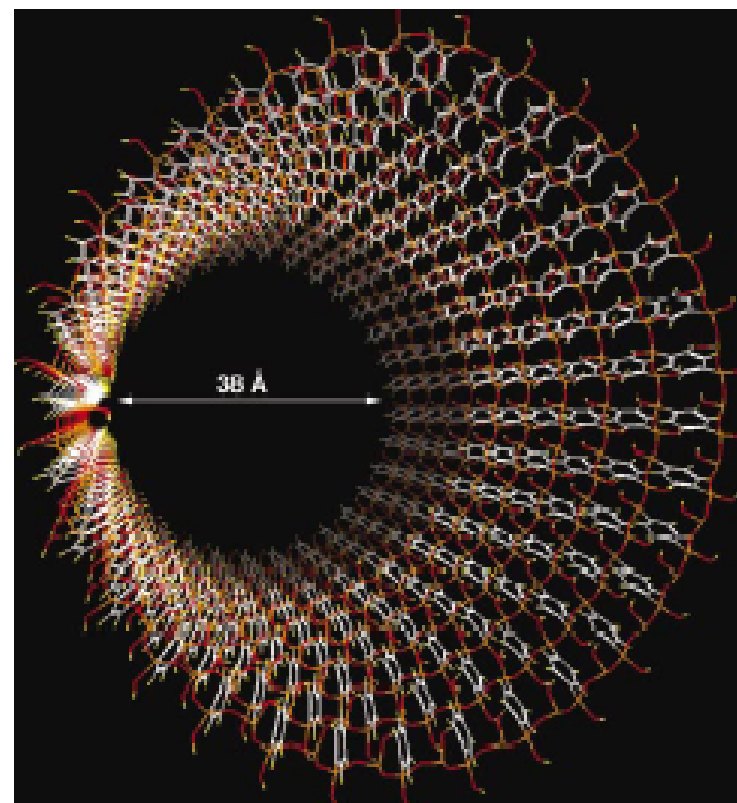

Figure 4 Model showing the pore surface of mesoporous benzene–silica. Benzene rings are aligned in a circle around the pore, fixed at both sides by silicate chains. The silicate is terminated by silanol (Si−OH) at the surface. Hydrophobic benzene layers and hydrophilic silicate layers array alternately at an interval of 7.6 Å along the channel direction. Silicon, orange; oxygen, red; carbon, white; hydrogen, yellow.
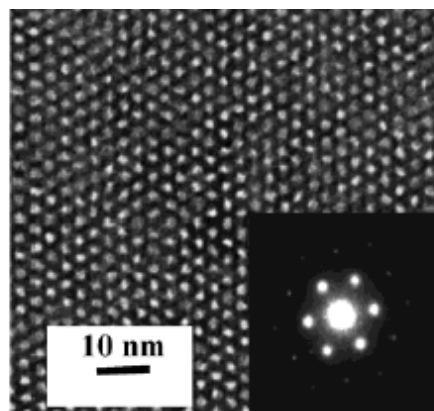
4

Organization of Phenylene-Bridged Hybrid Mesoporous Silisesquioxane with a Crystal-like Pore Wall from a Precursor with Nonlinear Symmetry

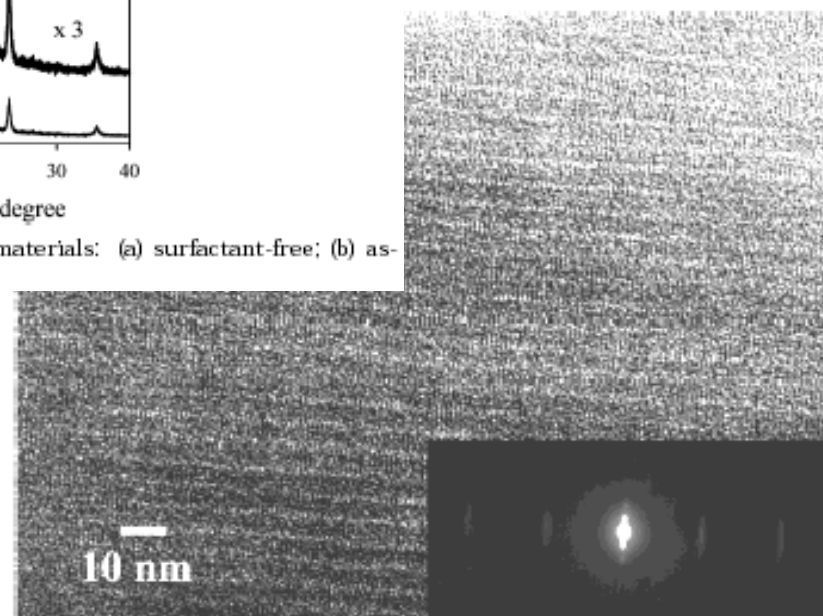Mahendra P. Kapoor,[†] Qihua Yang,[‡,§] and Shinji Inagaki*,[†]
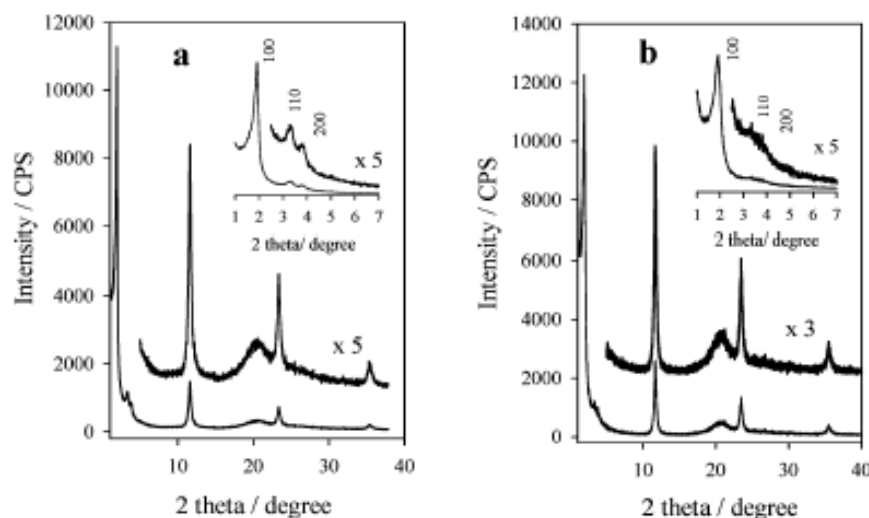
Figure 1. Powder X-ray diffraction patterns of 1,3-benzene-bridged hybrid mesoporous materials: (a) surfactant-free; (b) as-synthesized.

Figure 2. Transmission electron microscope image and electron diffraction pattern (inset) of surfactant-free 1,3-benzene-bridged hybrid mesoporous material.

Figure 3. Transmission electron microscope image and electron diffraction pattern (inset) perpendicular to channels showing many lattice fringes in the pore walls with a spacing of 7.6 Å.
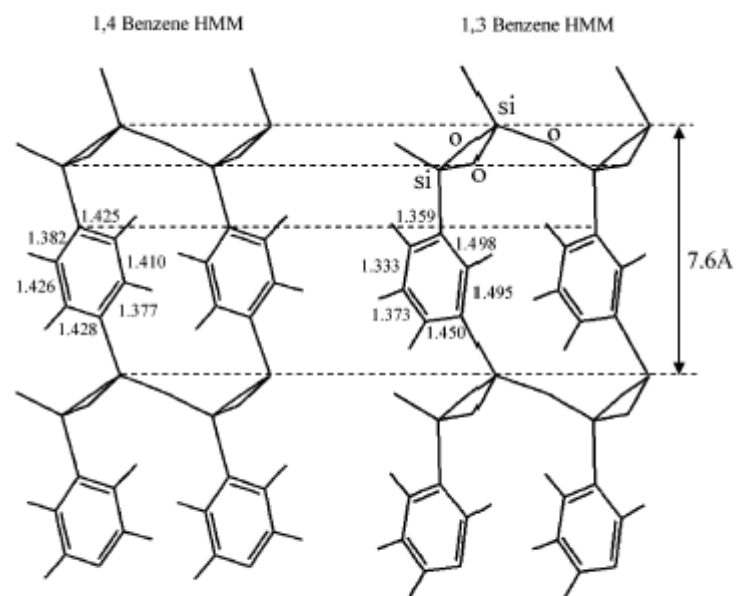
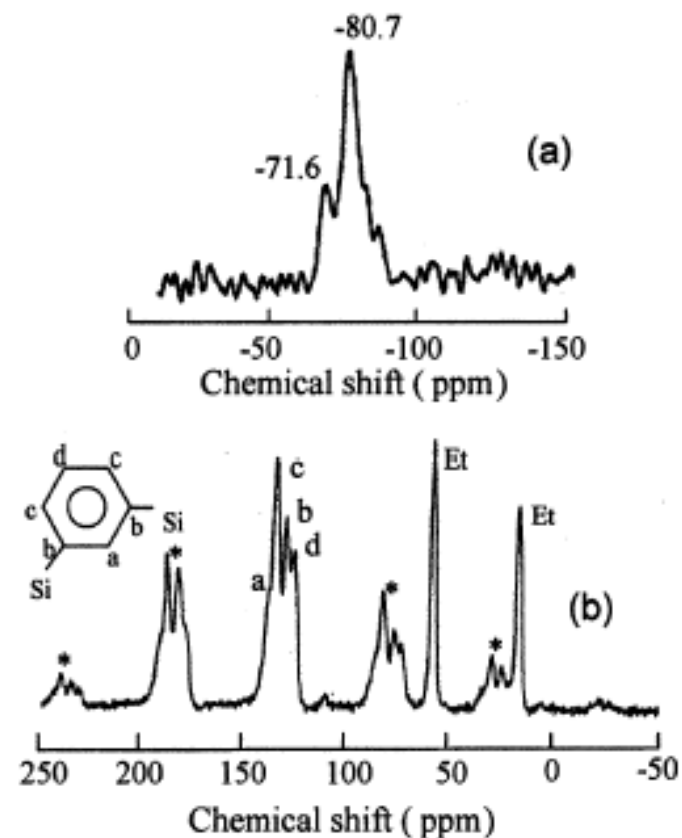**Figure 7.** Simulated structure models of benzene-bridged mesoporous material derived from precursors of different geometries.

Figure 5. (a) ^{29}Si MAS NMR and (b) ^{13}C CP MAS NMR spectra of the surfactant-free 1,3-benzene-bridged hybrid mesoporous material.

Thermal Stability
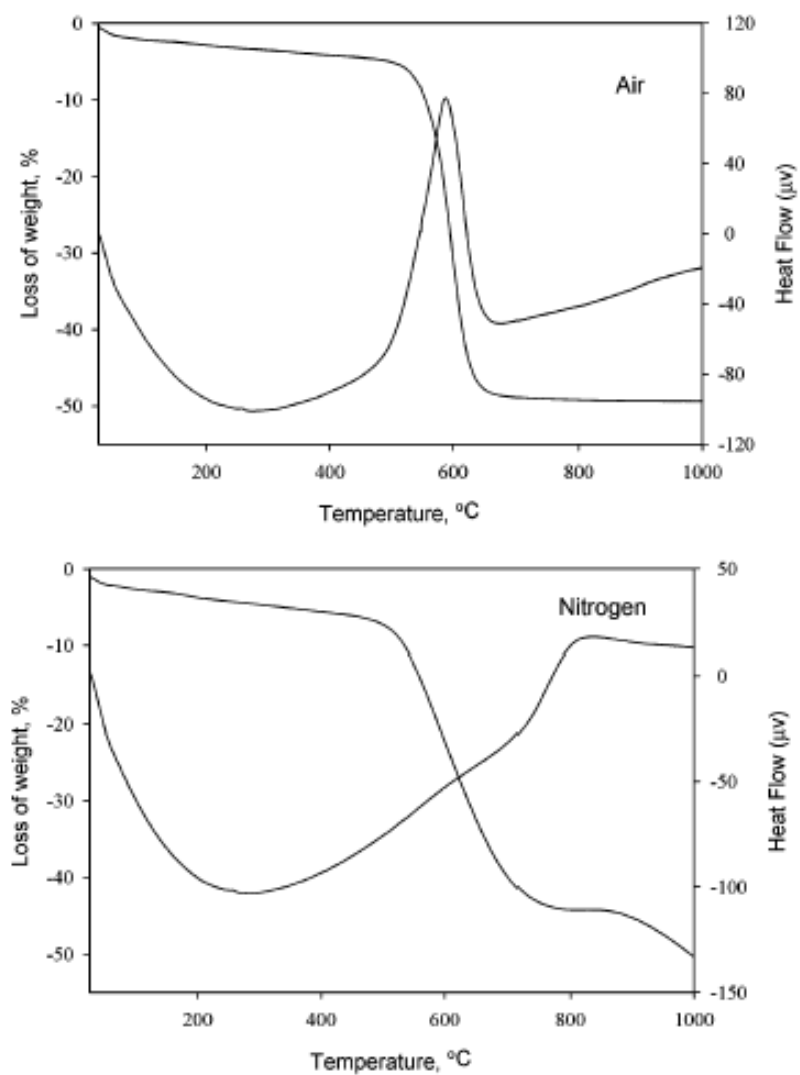
Figure 6. Thermogravimetric analysis of the surfactant-free 1,3-benzene-bridged hybrid mesoporous material under an air and nitrogen atmosphere.

Block Copolymer Templating Syntheses of Mesoporous Metal Oxides with Large Ordering Lengths and Semicrystalline Framework

Peidong Yang,[†] Dongyuan Zhao,[†,‡] David I. Margolese,[†] Bradley F. Chmelka,[‡,§] and Galen D. Stucky*,[†,‡]

Table 1. Syntheses Conditions (Precursor, Temperature, Aging Time) and the Ordering Lengths for the As-Synthesized Mesostructures

system	inorganic precursor	aging temp (°C)	aging time (day)	d (Å)
Zr	$ZrCl_4$	40	1	115
Ti	$TiCl_4$	40	7	123
Sn	$SnCl_4$	40	2	124
Nb	$NbCl_5$	40	2	106
Ta	$TaCl_5$	40	2	110
W	WCl_6	60	15	126
Hf	$HfCl_4$	40	1	124
Ge	$GeCl_4$	40	15	146
V	VCl_4	60	7	111
Zn	$ZnCl_2$	60	30	120
Cd	$CdCl_2$	40	7	111
In	$InCl_3$	60	30	124
Sb	$SbCl_5$	60	30	93
Mo	$MoCl_5$	60	7	100
Re	$ReCl_5$	60	7	121
Ru	$RuCl_3$	40	3	95
Ni	$NiCl_2$	40	2	100
Fe	$FeCl_3$	40	7	116
Cr	$CrCl_3$	40	4	117
Mn	$MnCl_2$	40	7	124
Cu	$CuCl_2$	40	7	98
SiAl	$AlCl_3/SiCl_4$	40	2	120
Si$_2$Al	$AlCl_3/SiCl_4$	40	2	130
ZrTi	$ZrCl_4/TiCl_4$	40	2	110
Al$_2$Ti	$AlCl_3/TiCl_4$	40	7	112
SiTi	$SiCl_4/TiCl_4$	40	3	103
ZrW$_2$	$ZrCl_4/WCl_6$	40	3	140
SnIn	$SnCl_4/InCl_3$	40	30	83

**Table 2. Physicochemical Properties of Mesoporous Metal Oxides Prepared Using $EO_{20}PO_{70}EO_{20}$ as the Structure-Directing Agent[a]**

oxide	inorganic precursor	d_{100}[b] (Å)	wall structure	wall thickness[c] (Å)	nanocrystal size[d] (Å)	pore size (Å)	BET surface area (m^2/g)	BET surface area (m^2/cm^3)	porosity[e]	physical properties
ZrO_2	$ZrCl_4$	106	tetra. ZrO_2	65	20	58	150	884	0.43	dielectric
TiO_2	$TiCl_4$	101	anatase	51	30	65	205	867	0.46	semiconductor
Nb_2O_5	$NbCl_5$	80	Nb_2O_5[f]	40	< 10	50	196	876	0.50	dielectric
Ta_2O_5	$TaCl_5$	70	Ta_2O_5[f]	40	< 10	35	165	1353	0.50	dielectric
WO_3	WCl_6	95	WO_3	50	30	50	125	895	0.48	semiconductor
SnO_2	$SnCl_4$	106	cassiterite	50	30	68	180	1251	0.52	semiconductor
HfO_2	$HfCl_4$	105	amorphous	50	–	70	105	1016	0.52	dielectric
Al_2O_3	$AlCl_3$	186	amorphous	35	–	140	300	1188	0.61	dielectric
SiO_2	$SiCl_4$	198	amorphous	86	–	120	810	1782	0.63	dielectric
$SiAlO_y$	$SiCl_4/AlCl_3$	95	amorphous	38	–	60	310	986	0.59	dielectric
Si_2AlO_y	$SiCl_4/AlCl_3$	124	amorphous	40	–	100	330	965	0.55	dielectric
$SiTiO_y$	$SiCl_4/TiCl_4$	95	amorphous	50	–	50	495	1638	0.63	dielectric
Al_2TiO_y	$AlCl_3/TiCl_4$	105	amorphous	40	–	80	270	1093	0.59	dielectric
$ZrTiO_y$	$ZrCl_4/TiCl_4$	103	amorphous	35	–	80	130	670	0.46	dielectric
ZrW_2O_y	$ZrCl_4/WCl_4$	100	amorphous	45	–	50	170	1144	0.51	NTE[g]

[a] All samples were prepared using ethanol as a solvent, except HfO_2 where butanol was used. [b] d values for samples calcined at 300–600 °C for 5 h in air. [c] Thicknesses measured from TEM experiments. These values are consistent with the values estimated by subtracting the pore diameter from $2d_{100}/\sqrt{3}$. [d] Nanocrystal sizes estimated from X-ray diffraction broadening using the Scherrer formula and the TEM studies. [e] The porosity is estimated from the pore volume determined using the adsorption branch of the N_2 isotherm curve at the $P/P_0 = 0.983$ signal point. [f] Nucleation just started, extremely broad wide-angle diffraction. [g] Materials with negative thermal expansion properties.

9
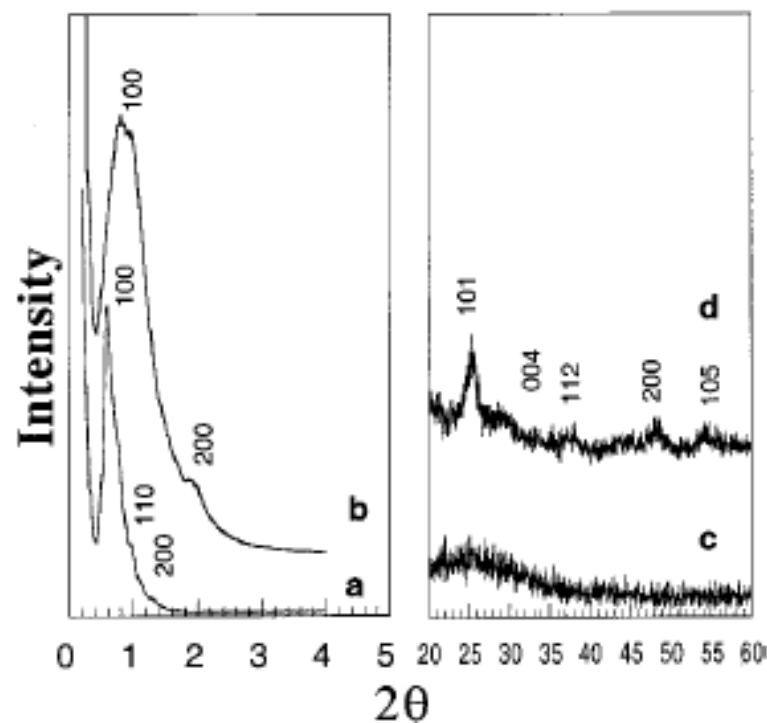
Figure 1. Low-angle and wide-angle X-ray diffraction (XRD) patterns of (a and c) as-synthesized $Ti(O,Cl)/EO_{20}PO_{70}EO_{20}$ composite mesostructure and (b and d) calcined mesoporous TiO_2.
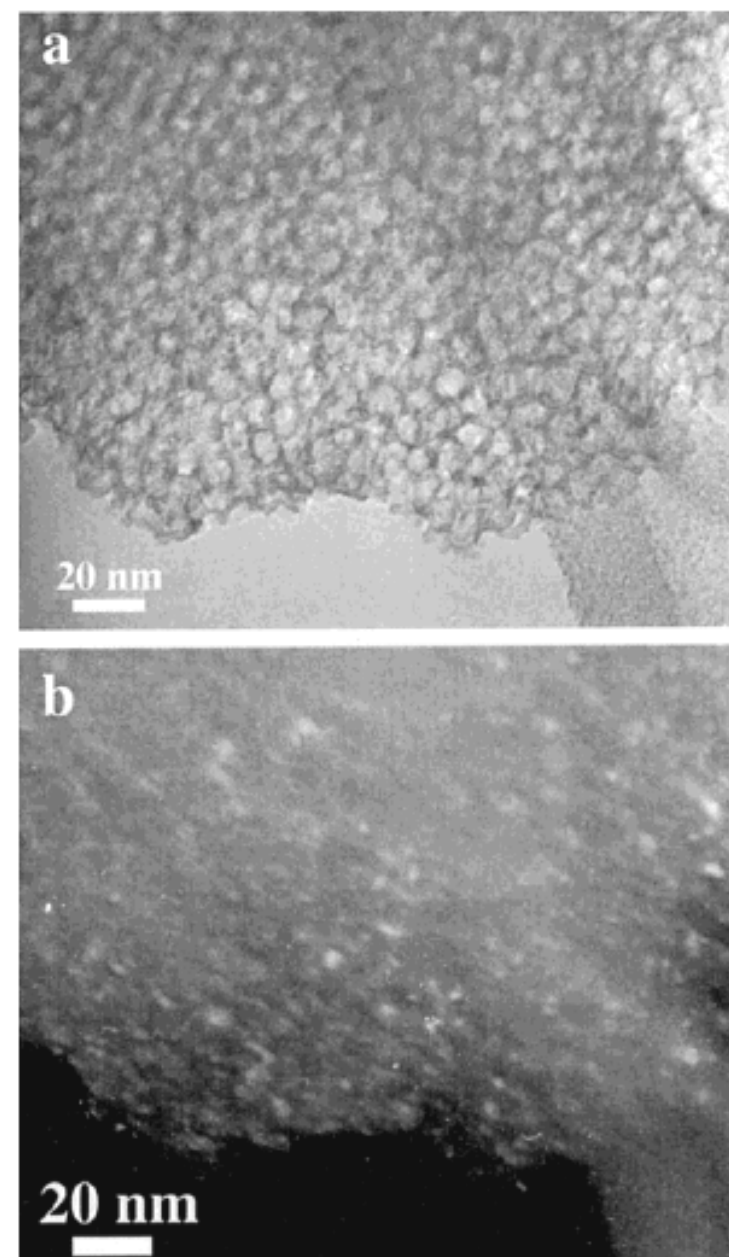


Figure 3. (a) Bright-field TEM image of a thin slice of the hexagonal mesoporous TiO_2 sample. (b) Dark-field image obtained on the same area of the same TiO_2 sample. The bright spots in the image correspond to TiO_2 nanocrystallites.

10
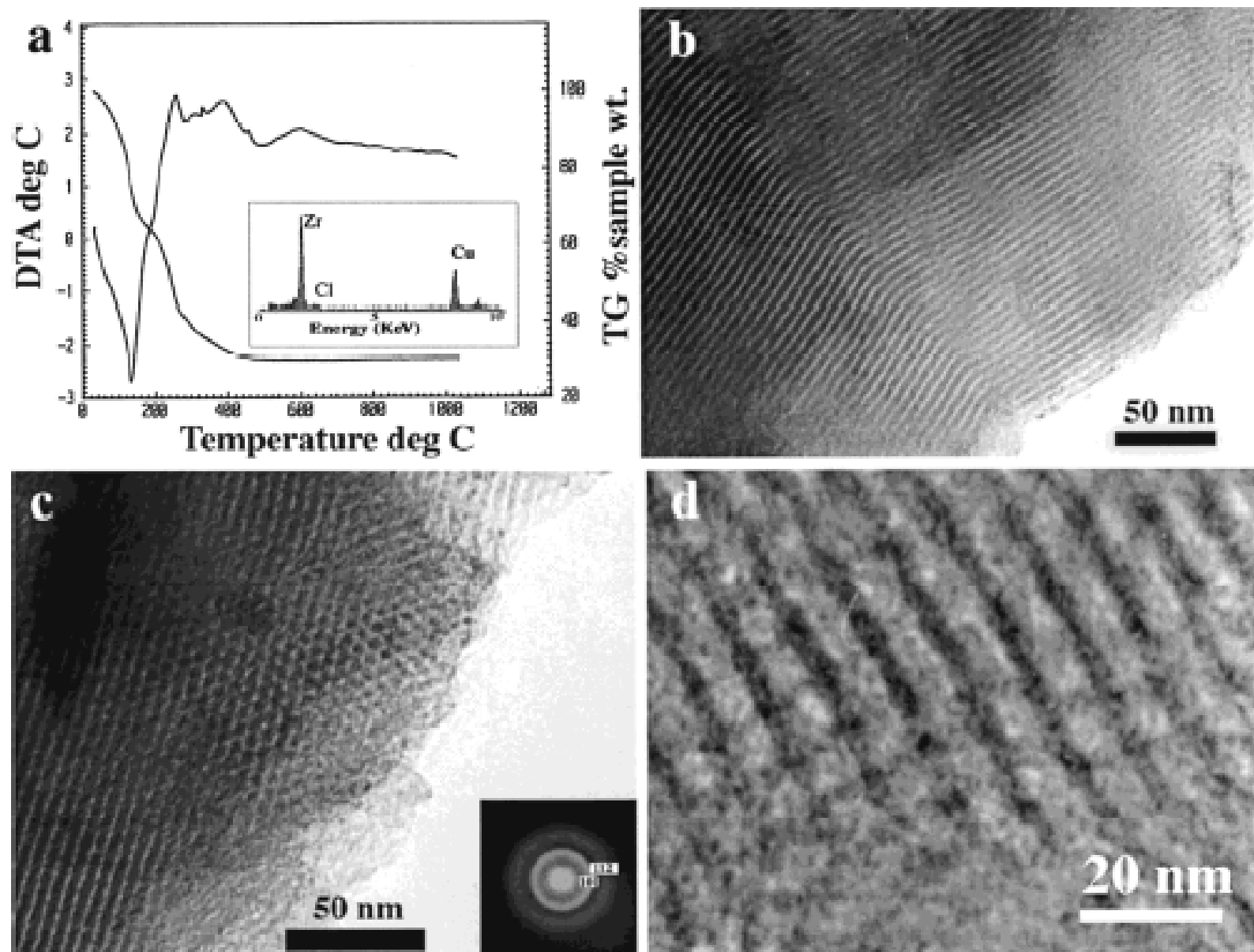
Figure 5. (a) TGA trace recorded for the as-synthesized Zr(O,Cl)/EO$_{20}$PO$_{m}$EO$_{20}$ composites. (b and c) TEM micrographs of two-dimensional hexagonal mesoporous ZrO$_2$ recorded along the [110] and [001] zone axes, respectively. Inset in part c is selected-area electron diffraction pattern obtained on the image area. (d) TEM image of cubic mesoporous ZrO$_2$.
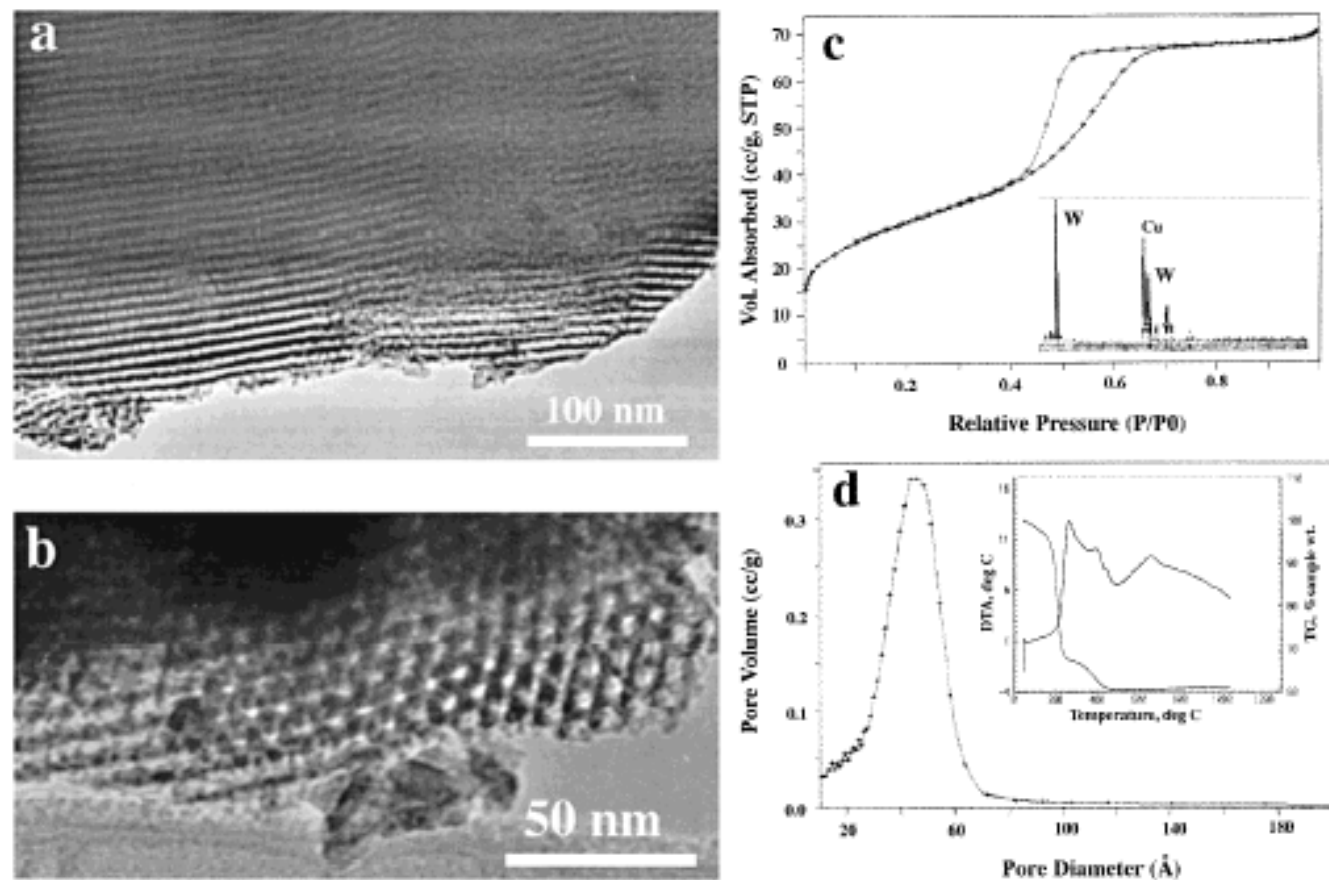
11
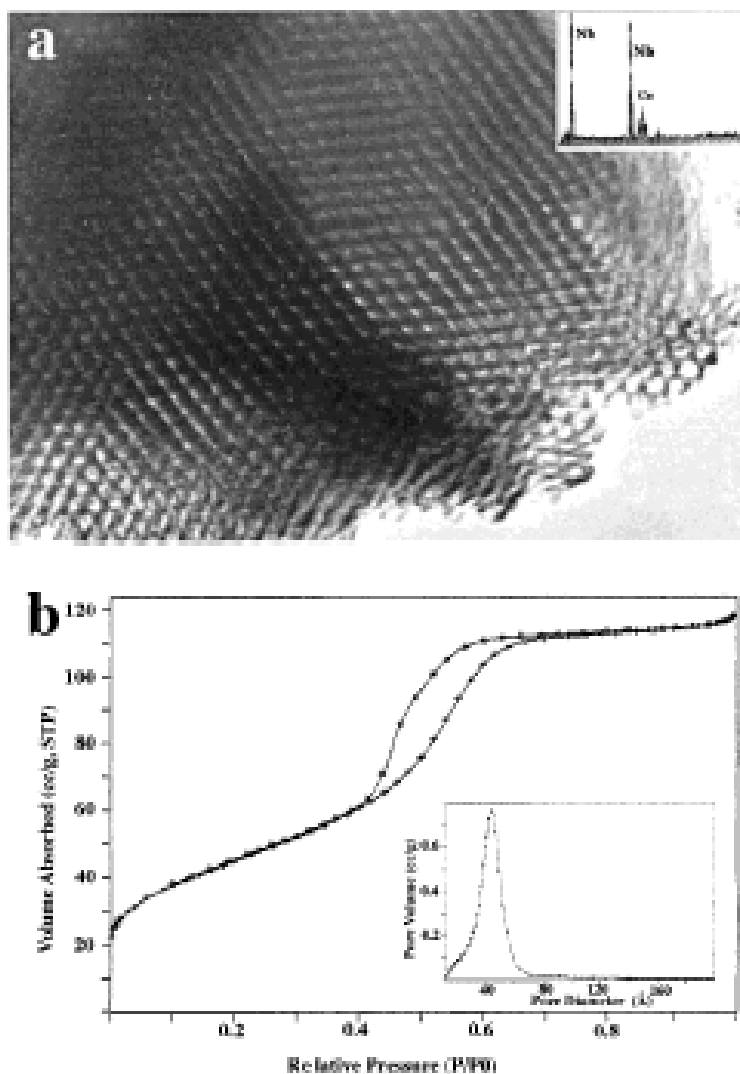
Figure 8. (a) TEM micrograph of two-dimensional hexagonal mesoporous Nb_2O_5 recorded along the [001] zone axis. The corresponding EDX spectrum is shown in the inset. (b) Nitrogen adsorption—desorption isotherms and BJH pore size distribution plot (inset) for calcined Nb_2O_5.
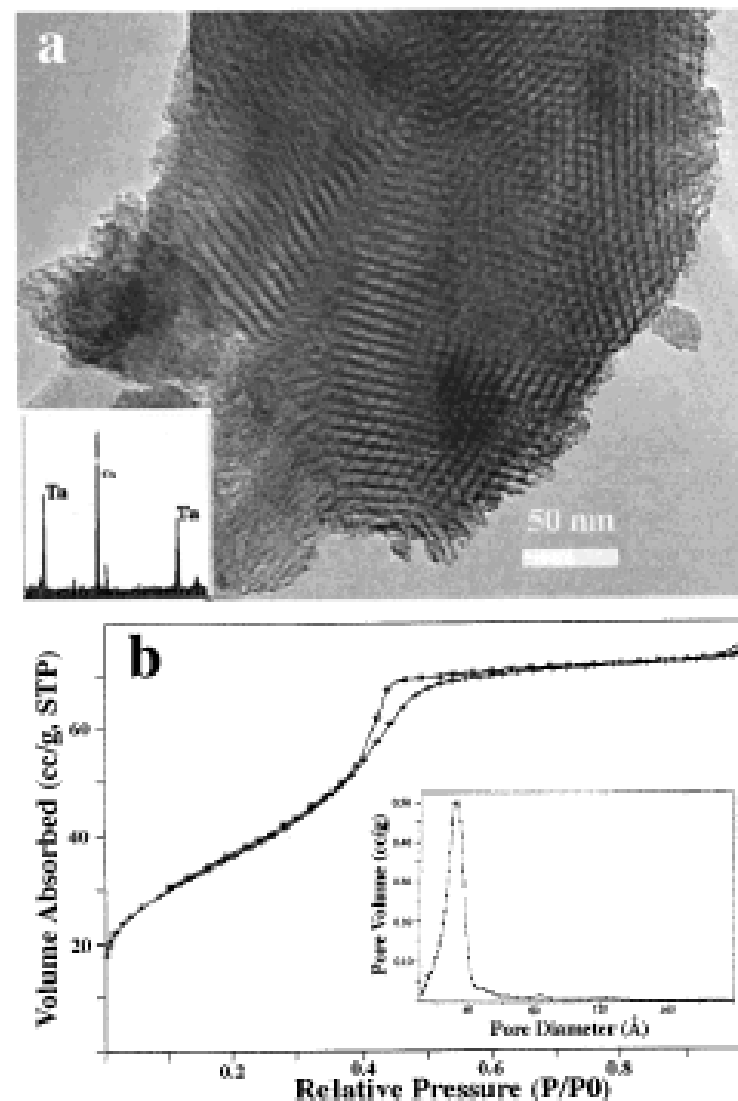
Figure 9. (a) TEM micrograph of two-dimensional hexagonal mesoporous Ta_2O_5 recorded along the [001] zone axis. The corresponding EDX spectrum is shown in the inset. (b) Nitrogen adsorption—desorption isotherms and BJH pore size distribution plot (inset) for calcined Ta_2O_5.

12
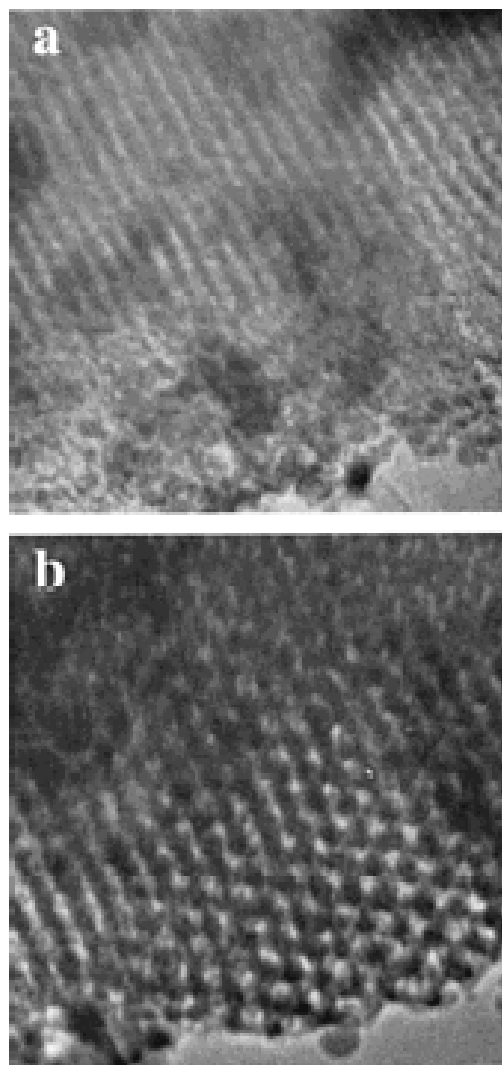
Figure 10. TEM micrographs of two-dimensional hexagonal mesoporous SnO₂ recorded along the [110] (a) and [001] (b) zone axes.


Figure 11. (a and b) TEM micrographs of two-dimensional hexagonal mesoporous WO₃ recorded along the [110] and [001] zone axes. (c and d) Nitrogen adsorption–desorption isotherms and BJH pore size distribution plot for calcined WO₃. Inset in part c is the corresponding EDX spectrum, and in part d the TGA trace obtained on the as-synthesized W(O,Cl)/copolymer composite.

13

Synthesis and photocatalytic properties of highly crystalline and ordered mesoporous TiO₂ thin films

Jing Tang,[a] Yiying Wu,[b] Eric W. McFarland[c] and Galen D. Stucky[*ab]
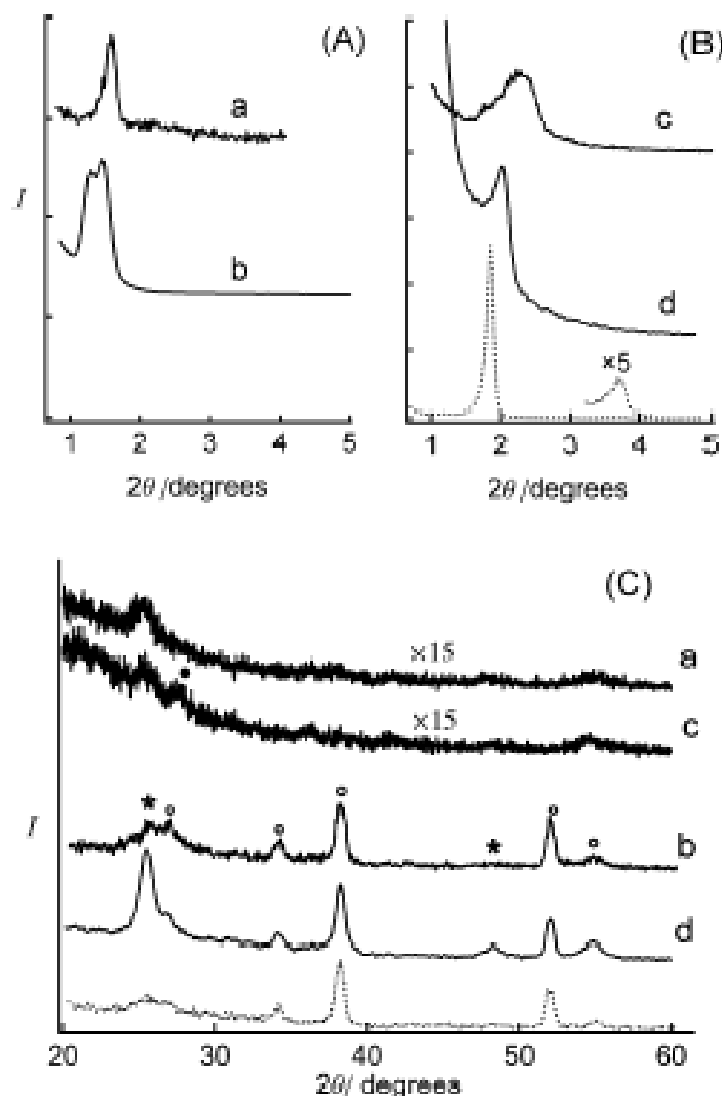
Fig. 1 Small-angle XRD patterns of (A) C–P123–TiO₂ thin films and (B) C–TiO₂ thin films crystallized at (a, c) 750 °C and (b, d) 550 °C. (C) Corresponding wide-angle XRD patterns. Data from starting mesoporous TiO₂ (template removed at 300 °C) were plotted (dotted line) as a reference. Diffraction peaks marked with circles (O) were from conducting substrates (SnO₂:F); peaks marked with asterisks (*) were from anatase. Substrates used for 750 °C calcinations were quartz, and therefore no circles were marked. The peak labelled with a solid circle was from rutile. The X-ray source is Cu Kα.

14
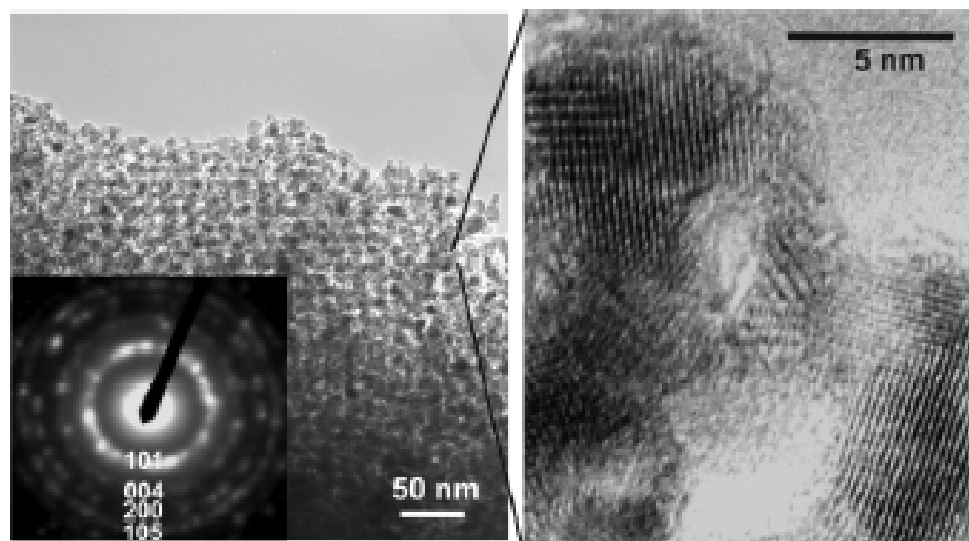
Fig. 2 TEM images of a TiO₂ thin film crystallized at 550 °C with pure post-induced carbon as the confining material. The zoom-in image is also shown on the right. The inset is a selected area electron diffraction pattern (SAED) indexed as the anatase phase.

Fig. 3 Photoconversion efficiencies of (a) C–TiO$_2$, (b) control and (c) C–P123–TiO$_2$ samples at zero-bias and illumination of 40 mW cm^{-2}. Film thickness was 250–300 nm.

15
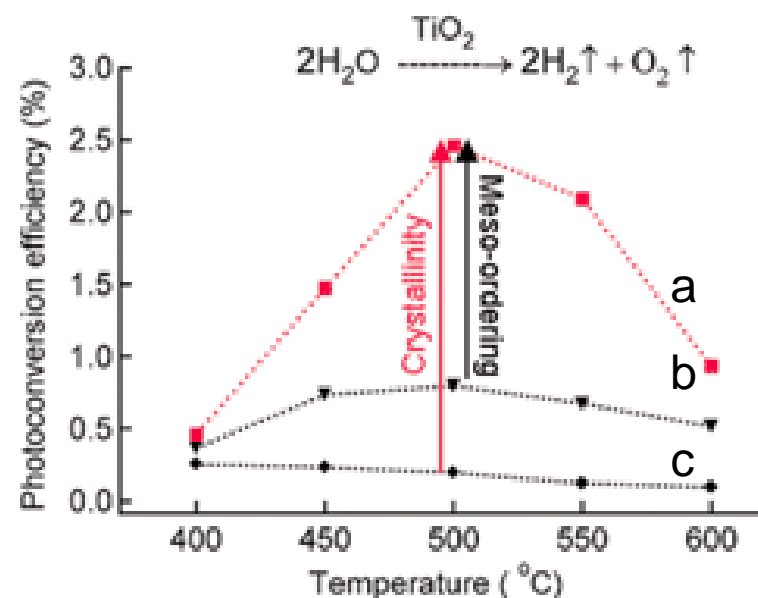
Preparation and gas-sensing properties of thermally stable mesoporous SnO₂

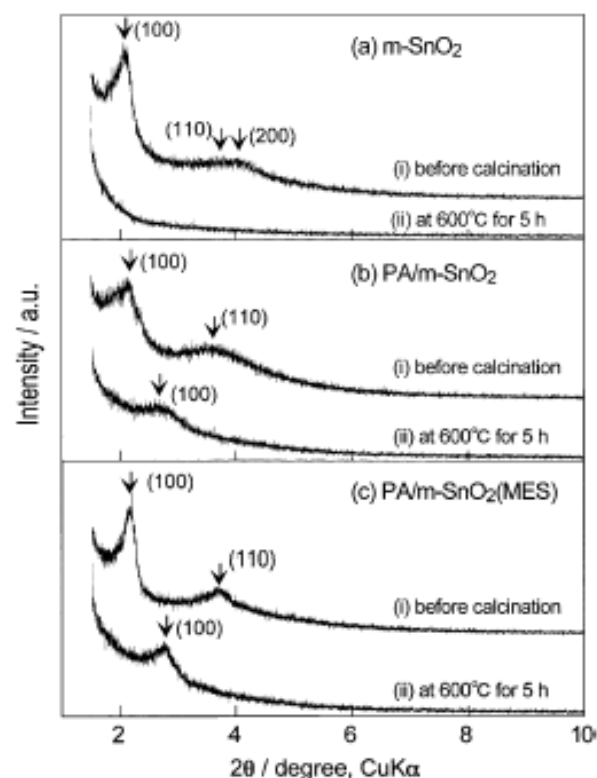Takeo Hyodo, Norihiro Nishida, Yasuhiro Shimizu,
Makoto Egashira[*]

Fig. 1. XRD patterns of (a) m-SnO₂, (b) PA/m-SnO₂ and (c) PA/m-SnO₂(MES) (preparation conditions: C₁₆PyCl concentration = 2 wt.%, [C₁₆PyCl]/[Na₂SnO₃] = 2, ([MES]/[Na₂SnO₃]) = 2.5, pH = 10).

PA/m-SnO₂(MES)
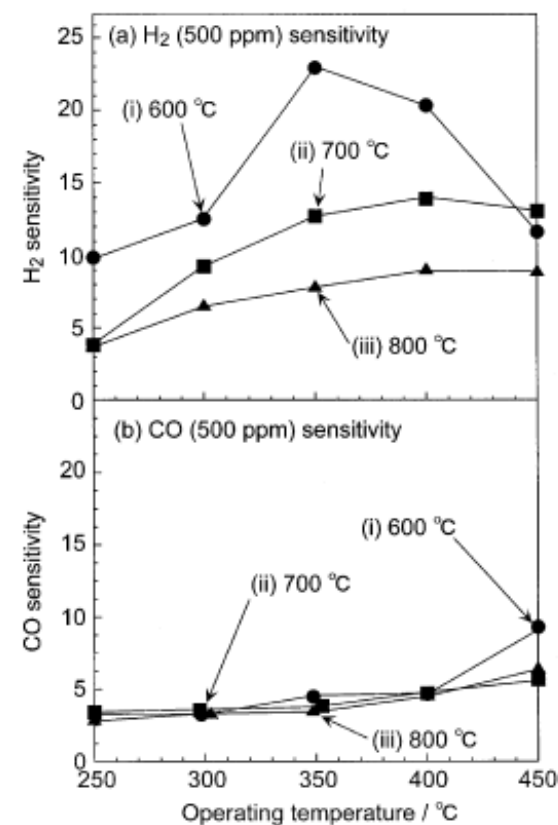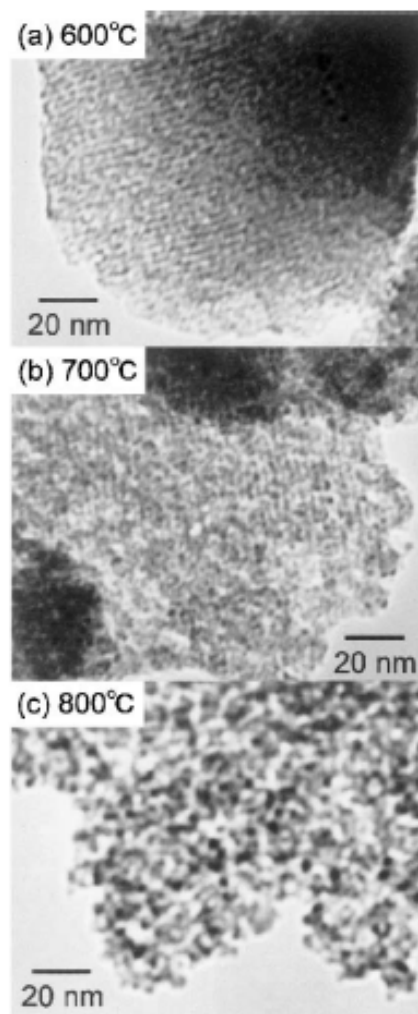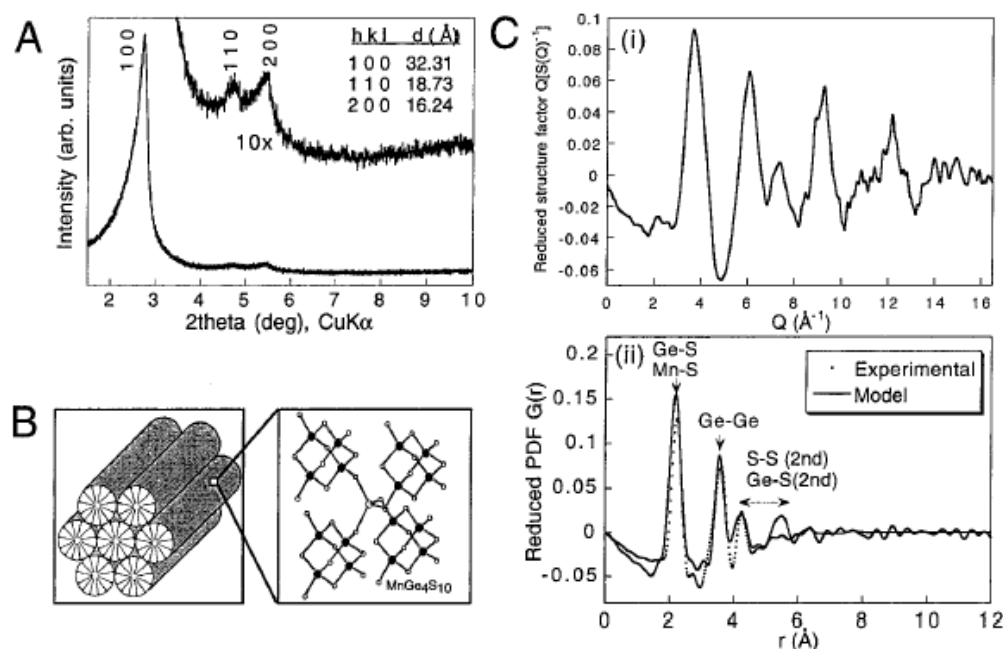

Fig. 6. Operating temperature dependence of sensitivity to (a) 500 ppm H₂ and (b) 500 ppm CO of PA/m-SnO₂(MES). Calcination temperature: (i) 600 °C, (ii) 700 °C and (iii) 800 °C.

16

Aqueous Mediated Synthesis of Mesostructured Manganese Germanium Sulfide with Hexagonal Order

K. Kasthuri Rangan,[†] Simon J. L. Billinge,[‡]
Valeri Petkov,[‡] Joy Heising,[†] and
Mercouri G. Kanatzidis*,[†]

Figure 1. (A) Powder X-ray diffraction pattern of $C_{14}MnGeS$ (Rigaku, Cu Kα) showing low angle peak corresponding to 100 of the hexagonal cell and 110 and 200 reflections in an expanded scale, (B) schematic representation of hexagonal ordered structure of $C_{14}MnGeS$ and local structure of "metal−thiogermanate wall" encapsulating rod micelles, and (C) (i) reduced structure factors $Q[S(Q) − 1]$ of $C_{14}MnGeS$, derived from the wide-angle X-ray diffraction pattern (Huber diffractometer in symmetric reflection geometry and Ag Kα radiation) and (ii) reduced pair distribution function, $G(r)$ plotted against distance r. Figure also shows PDFs corresponding to a model based on the structure of crystalline $[(CH_3)_4N]_2MnGe_4S_{10}$.
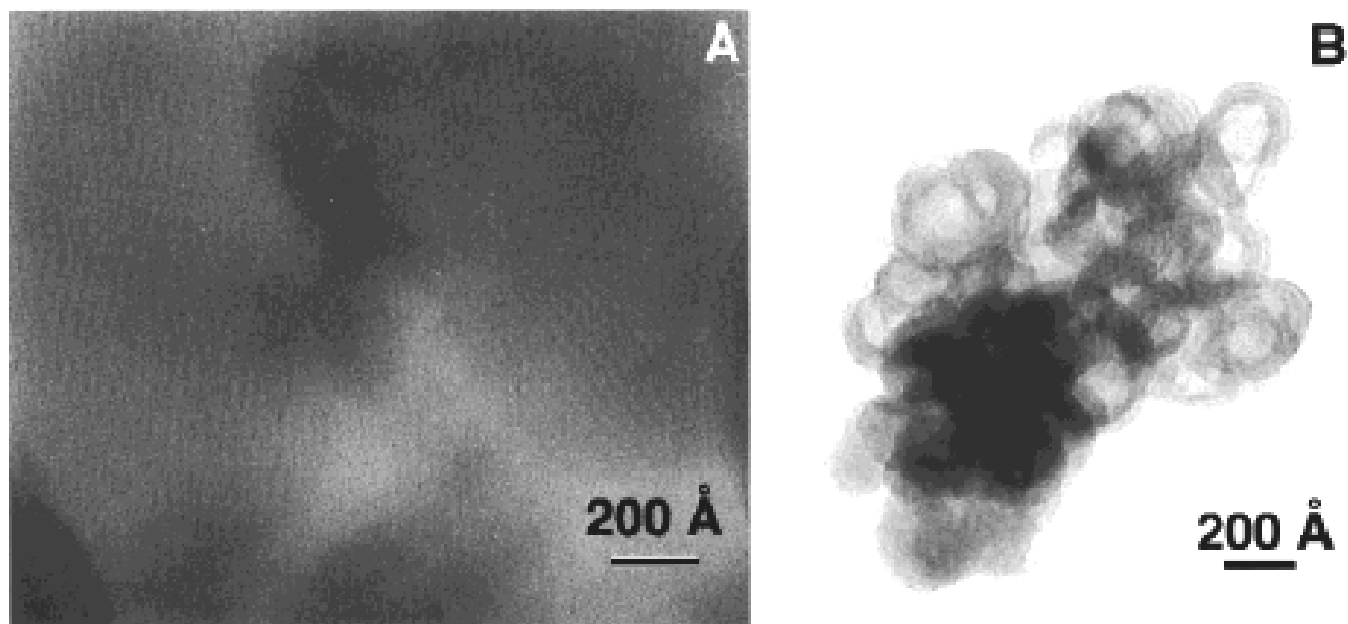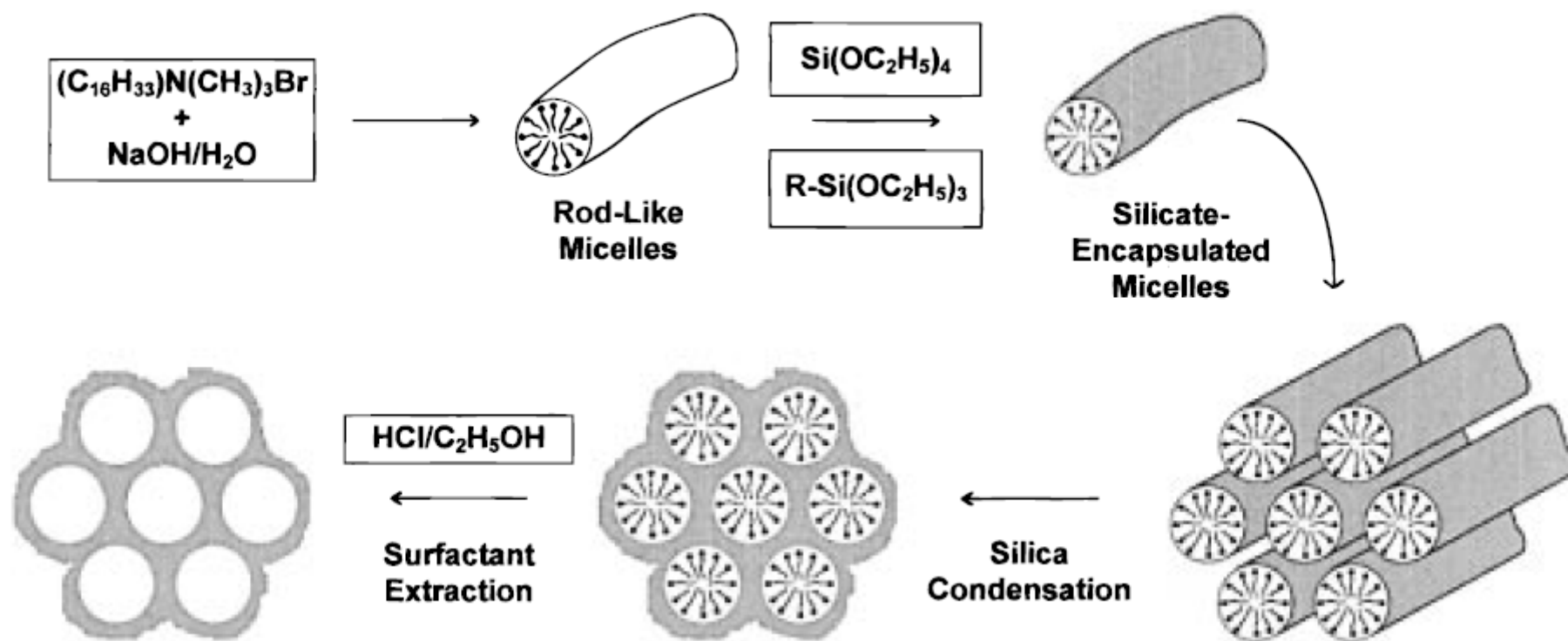
17

Figure 3. High-resolution transmission electron micrographs of $C_{14}MnGeS$ (A) as prepared sample and (B) "calcined" sample.

Scheme showing a generalized approach to the synergistic synthesis of an organized hybrid silica mesophase.

Chem. Mater. **1997, 9, 2300-2310**

Figure 1. Mesostructured thin-film formation by dip-coating. Step 1: the isotropic initial sol where the condensation is optimally slowed down. Step 2: the evaporation proceeds and micelles start to form above the CMC. Step 3: the evaporation is complete; the film equilibrates with its environment (MSS) and the final mesostructure is selected by adjusting the RH before further inorganic condensation. Step 4: the inorganic network is condensed; the hybrid mesostructure is stabilized.

Evaporation-induced self-assembly (EISA)

C. Sanchez's group

ADV. FUNCT. MATER. 14, 2004, pp. 309-322

Highly Organized Mesoporous Titania Thin Films Showing Mono-Oriented 2D Hexagonal Channels**

By *David Grosso, Galo J. de A. A. Soler-Illia, Florence Babonneau, Clément Sanchez,* Pierre-Antoine Albouy, Aline Brunet-Bruneau,* and *A. Ruud Balkenende*

$$HO(CH_2CH_2O)_{20}C_{16}H_{33}$$
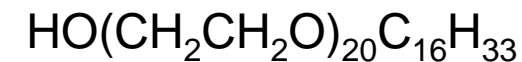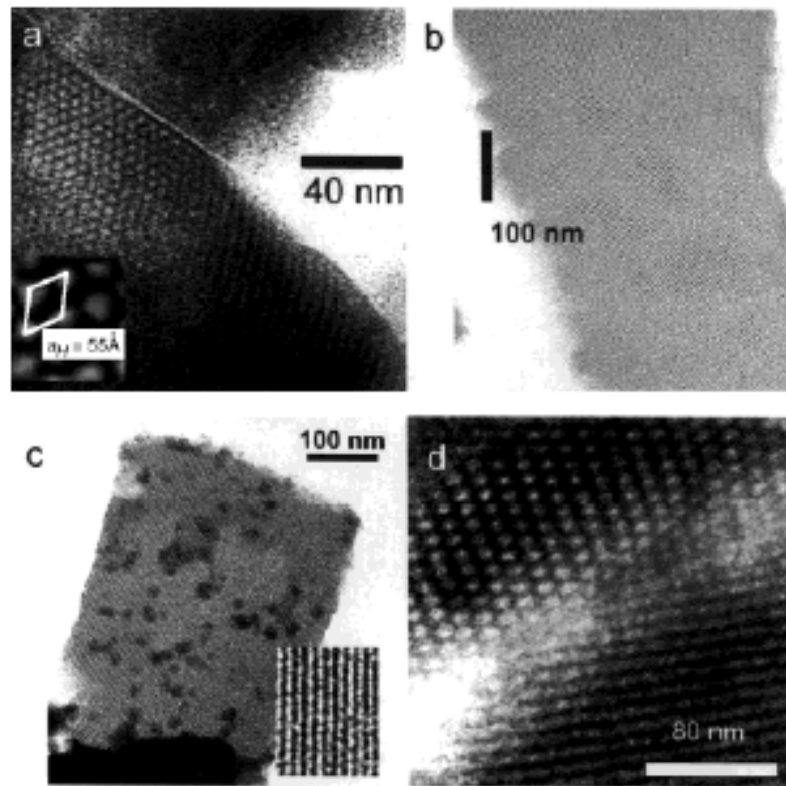
Surfactant: Brij 58

Fig. 3. TEM images of templated titania-based films: as-prepared Brij 58-titania hybrid, along the a) [001] and b) [110] zone axes of the hexagonal mesostructure; the detailed area in (a) (4×) depicts the hexagonal cell. c) Thermally treated Brij-58 templated film (350 °C), viewed along the [110] zone axis of the rectangular cell; the detailed area is magnified four times. d) Elliptical pores in F127-templated titania calcined to 350 °C; a slight tilting due to the cut can be observed. TEM was performed on ultramicrotomed specimens, previously detached from the film and embedded in epoxy resin.
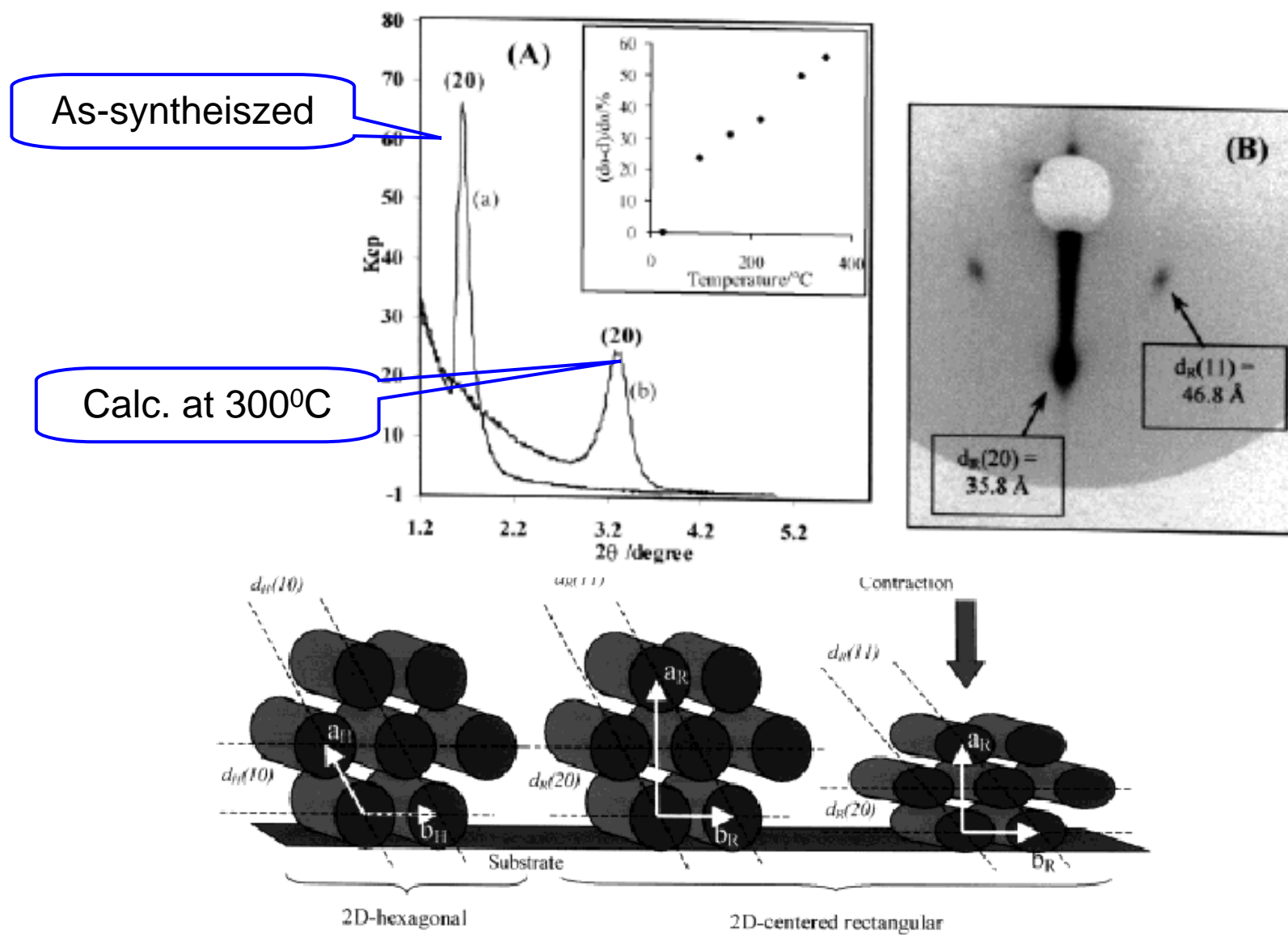
21

As-syntheiszed

Calc. at 300°C

Fig. 2. Schematic representation of the relationships between hexagonal ($p6m$), and centered-rectangular ($c2m$) two-dimensional cells. The latter adequately describes the uniaxial contraction.

22

Highly Porous TiO$_2$ Anatase Optical Thin Films with Cubic Mesostructure Stabilized at 700 °C

David Grosso,[†] Galo J. de A. A. Soler-Illia,[†] Eduardo. L. Crepaldi,[†]
Florence Cagnol,[†] Christophe Sinturel,[‡] Alexis Bourgeois,[§]
Aline Brunet-Bruneau,[§] Heinz Amenitsch,[‖] Pierre A. Albouy,[⊥] and
Clément Sanchez*,[†]
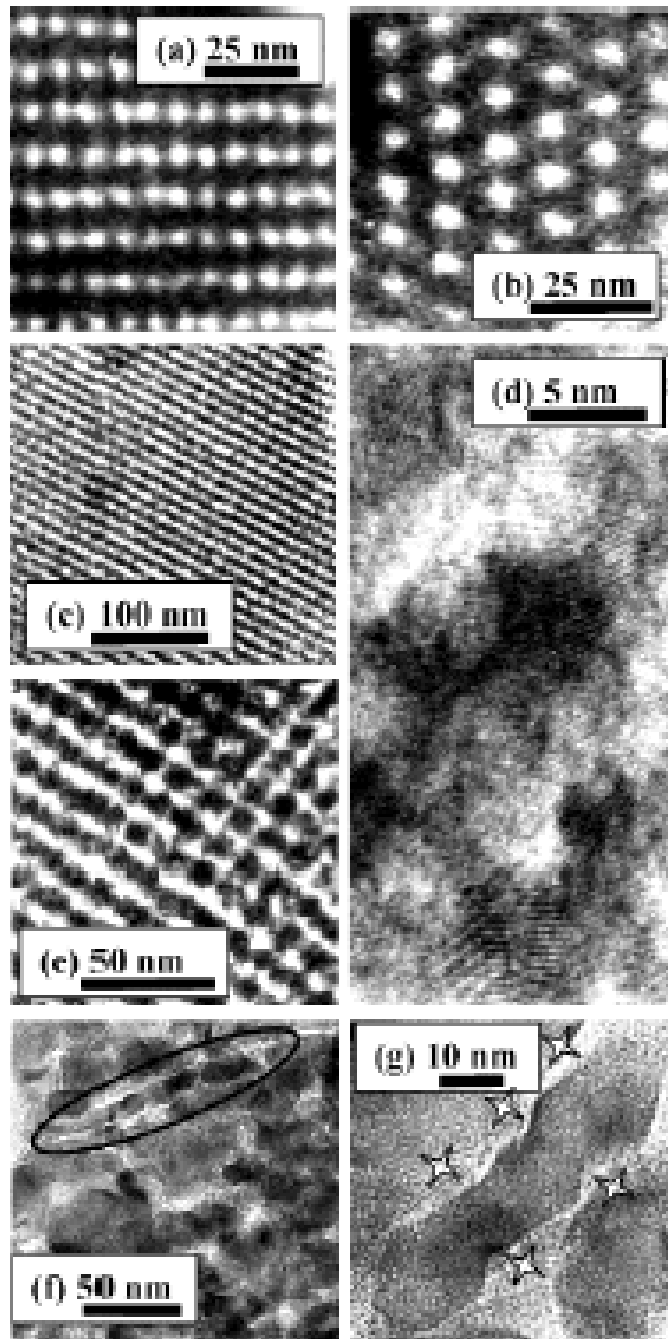
**Figure 5.** HRTEM images of TiO$_2$-based films treated at 100 °C for 12 h ((a) [100] zone axis, and (b) [111] zone axis); treated up to 500 °C (T_c) for 6 h following the PT10 conditions ((c) and (d) [110] zone axis, and (e) [1$\bar{1}$0] zone axis); and treated at 730 °C for 20 min following the PT20 conditions ((f), and (g) enlargement of (f)). The white stars indicate the pore positions in the initial structure.

23

Table 2. RBS and VASE Results Corresponding to a PT20 Sample at Various Temperatures along the Treatment Process

sample DRC		Ti[a]	O/Ti[a]	C/Ti[a]	$P_{RBS}{}^{b}$ (%)	n_{VASE} F[c]	n_{VASE} W[c]	$P_{VASE}{}^{b}$ (%)
300 °C	amor.	1.73×10^{22}	2	0.7	40	1.75	2.18	45
500 °C[d]	cryst.					1.85	2.27	35
730 °C	cryst.	2.10×10^{22}	1.8	0.1	28	1.89	2.32	35

[a] RBS atoms contained are given in number of atoms per cm^{-3} for Ti, and in molar ratio for C and O with 10% error. [b] P_{RBS} and P_{VASE} are porous volumes deduced from both RBS and VASE techniques with 10% error (RBS error) and 5% error (Bruggeman effective medium approximation model), respectively. [c] Optical constants n_{VASE} F (for film samples) and n_{VASE} W (for network walls) obtained by VASE are given for $\lambda = 600$ nm. [d] The 500 °C sample stood 12 h at this temperature.
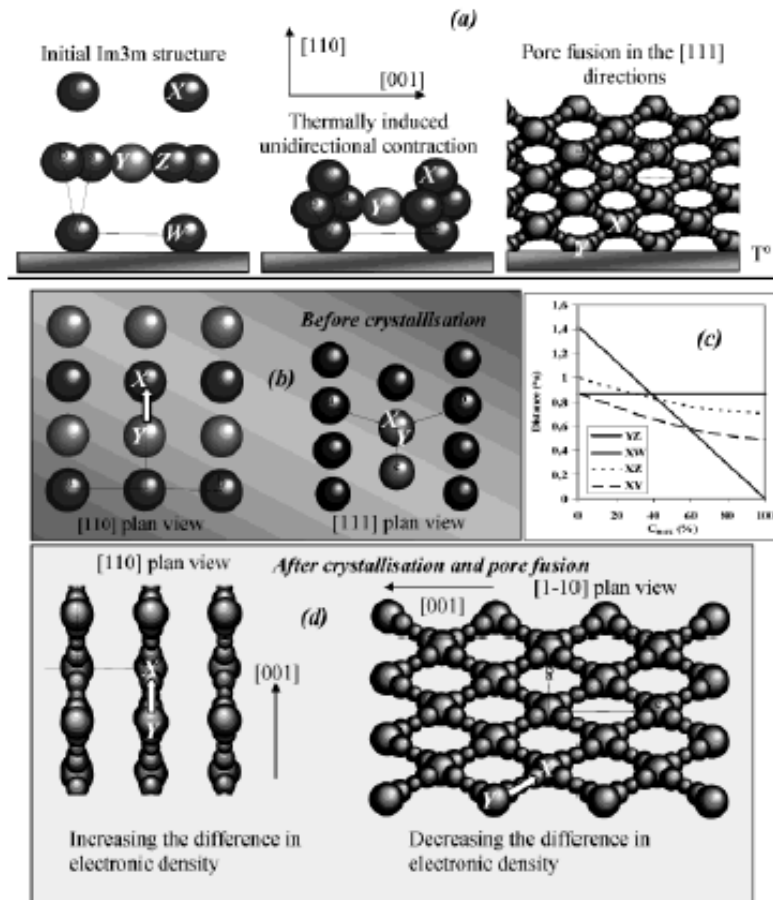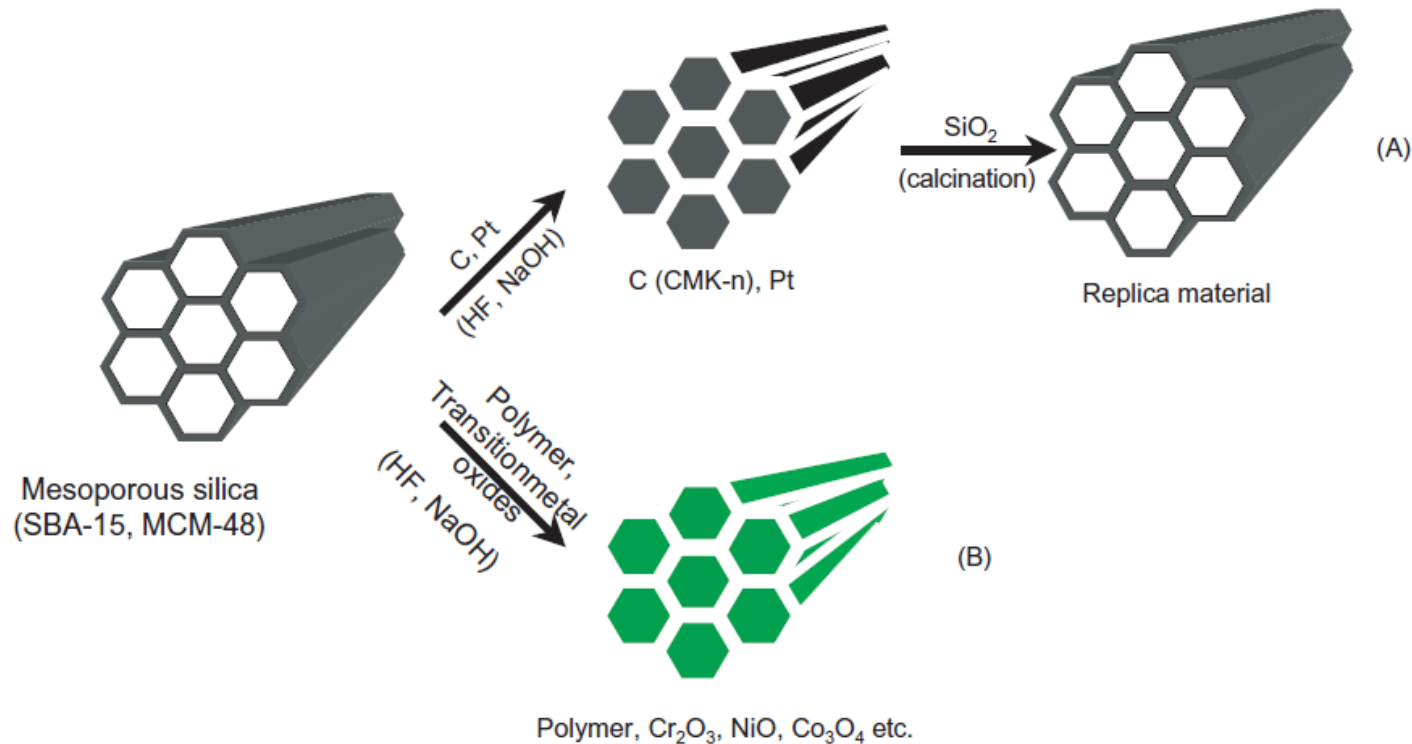

Figure 6. Scheme representing the structural variation during the various steps of heat treatment.
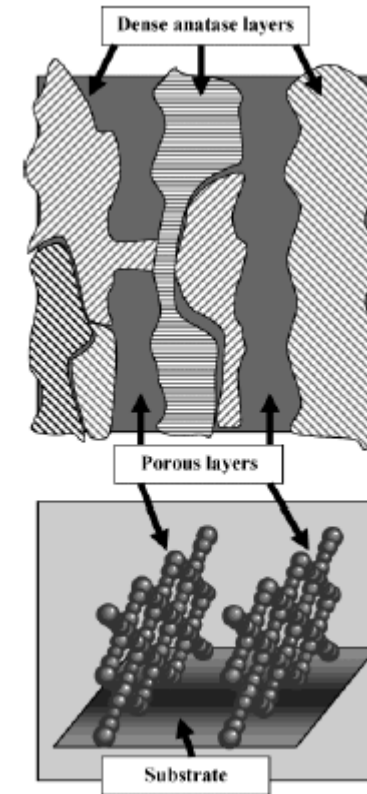
Figure 7. Scheme illustrating the final mesoporous crystalline structure.

24

Nanocasting pathway

Schematic description of the nanocasting pathway. (A) Loading with carbon or platinum and following dissolution of mesoporous silica gives the corresponding porous materials with negative replica structure. Subsequent back casting with silica source and removal of carbon by calcination allows to obtain positive replica porous silica material. (B) Incorporation of polymer or metal oxides instead of carbon or platinum also allows to obtain new mesoporous materials.

25
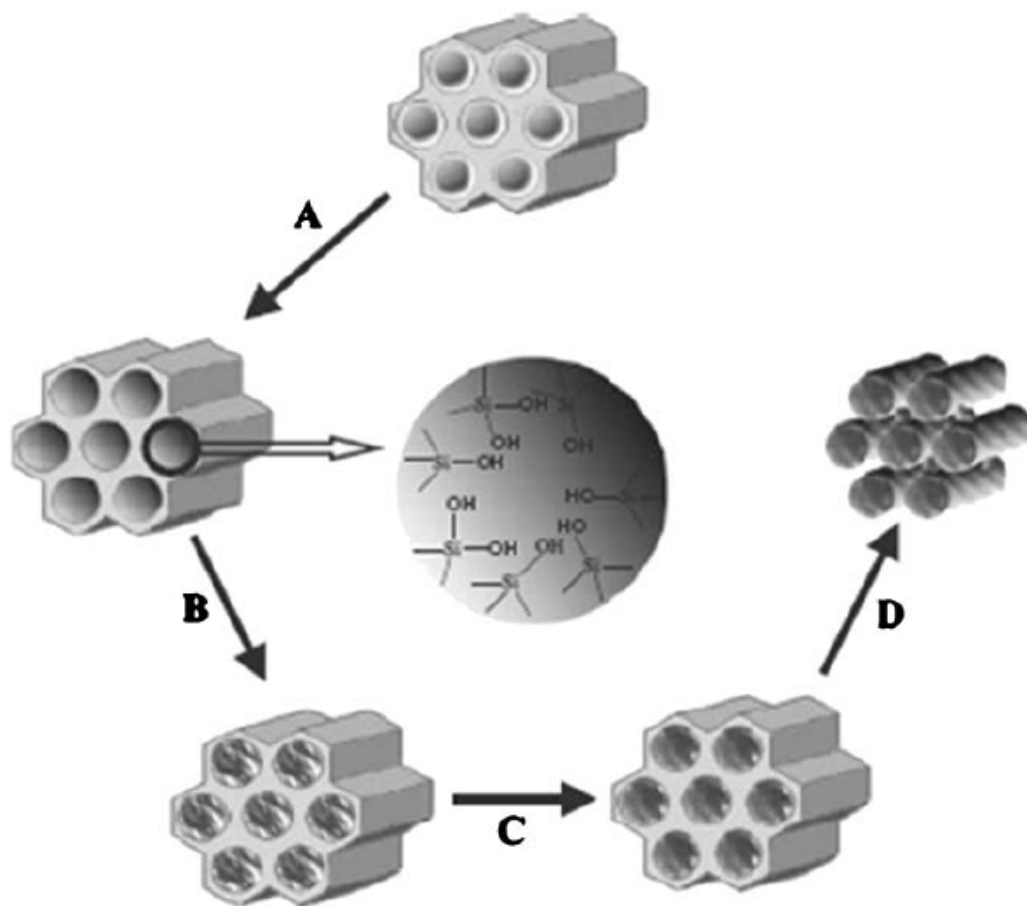
The synthetic procedure for **metal oxide nanowire arrays** by using mesoporous silica as a template.

A) Removal of the surfactants in as-synthesized mesoporous silica materials by microwave-digestion method.

B) Incorporation of ethanol solutions of metal salts into the channels of microwave-digested mesoporous silica.

C) Heating process to decompose the metal salts to metal oxides inside the channels.

D) Dissolution of silica to create the mesostructured replica.
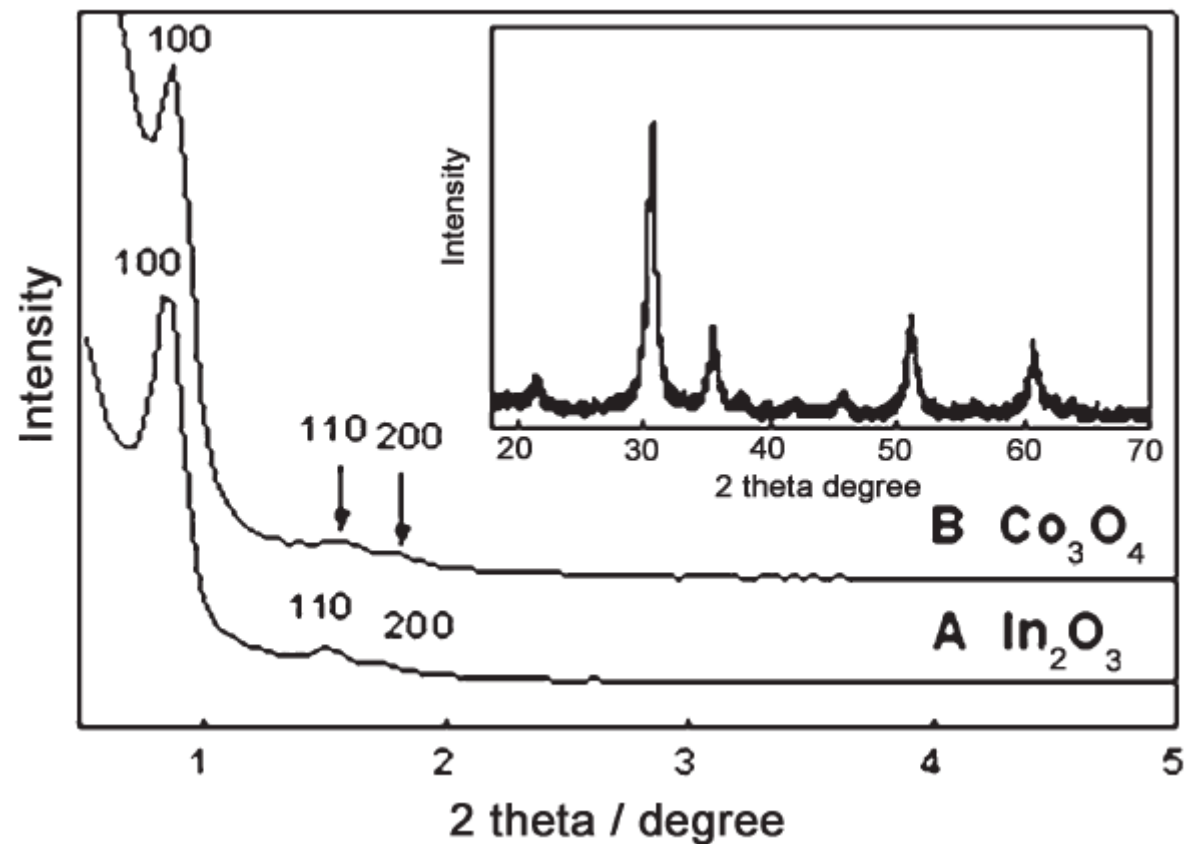
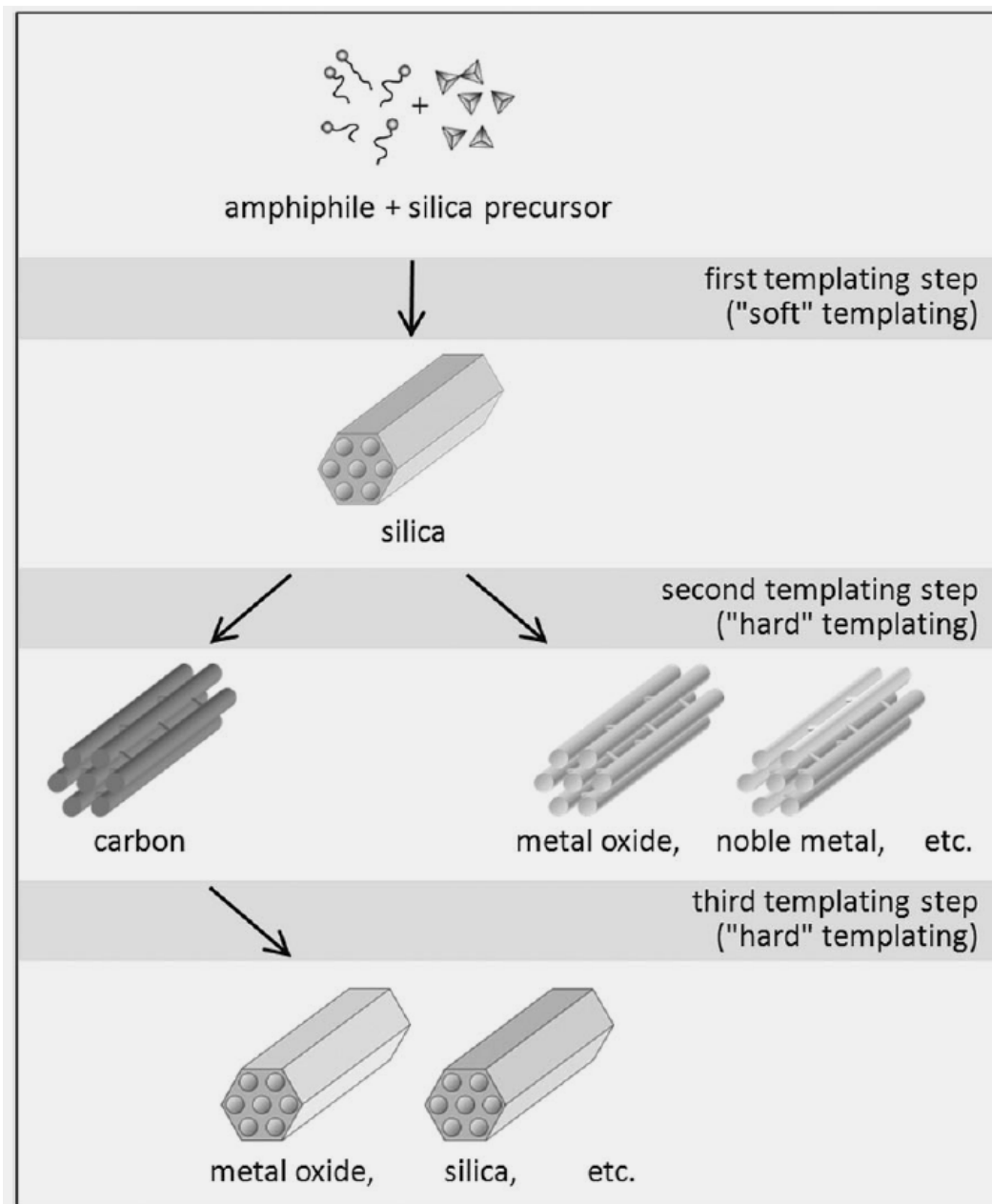Small-angle XRD patterns of: A) In_2O_3 and B) Co_3O_4 nanowire arrays templated by MWD-SBA-15. The inset is the wideangle XRD pattern of an In_2O_3 nanowire replica material.

Repeated Templating

amphiphile + silica precursor

first templating step ("soft" templating)

silica

second templating step ("hard" templating)

carbon

metal oxide, noble metal, etc.

third templating step ("hard" templating)

metal oxide, silica, etc.

Schematic drawing of repeated templating for the synthesis of ordered mesoporous materials. The first step is "soft templating" (endotemplating), i.e., structure formation by utilization of amphiphilic structure directors; the following steps are "hard templating" (exotemplating).
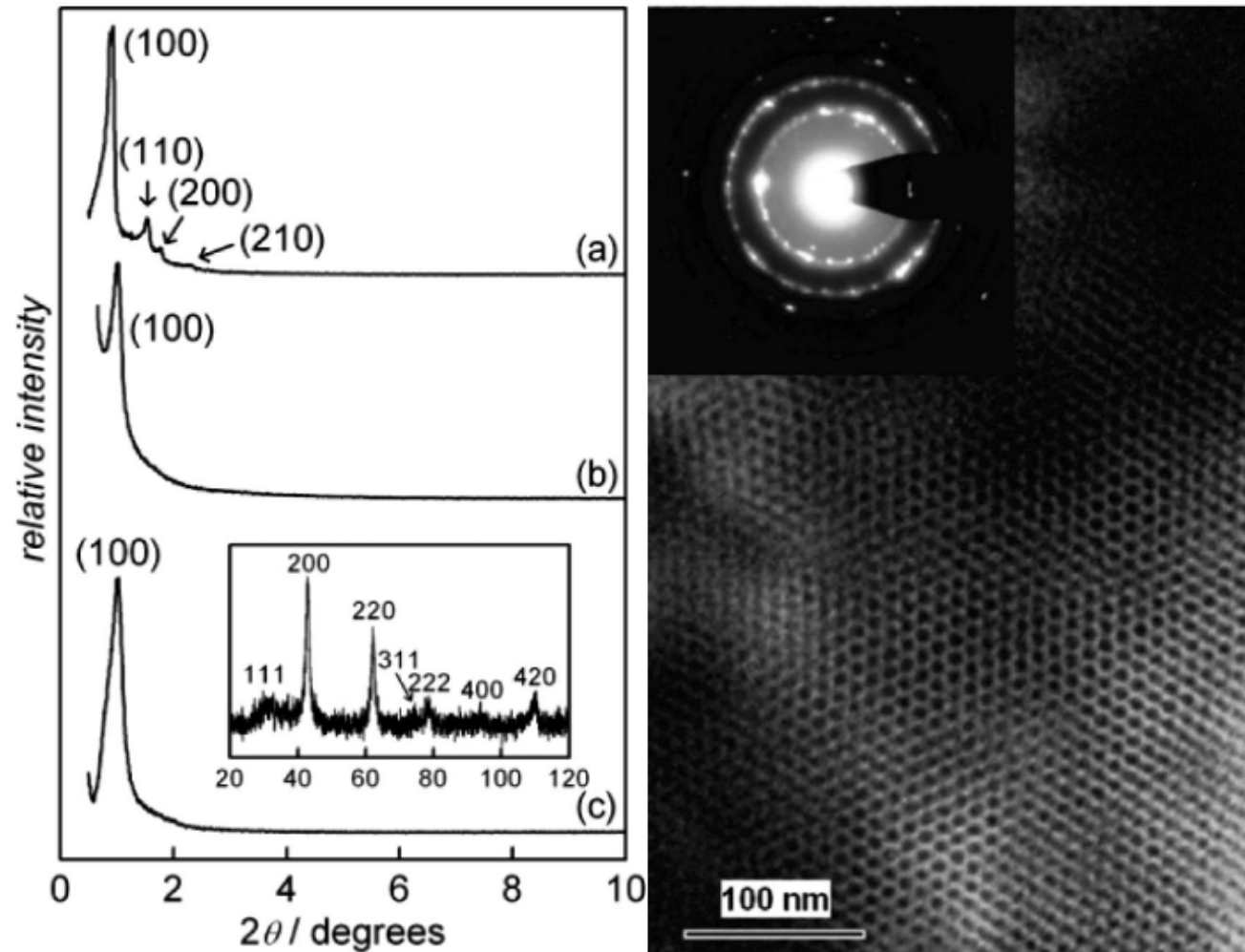
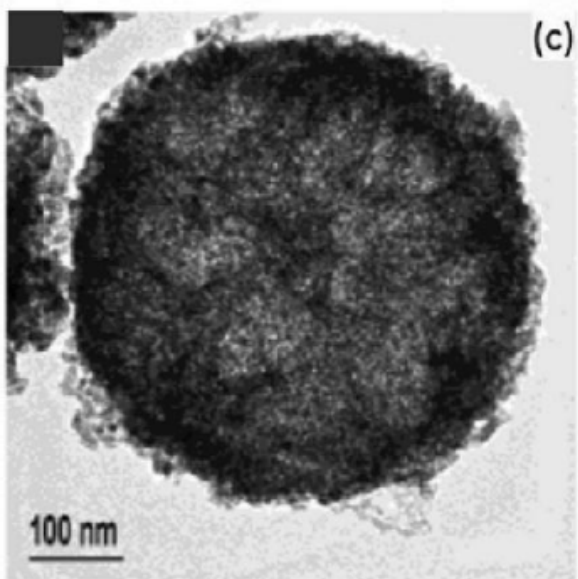(Left) Powder X-ray diffraction diagrams of (a) SBA-15 silica, (b) CMK-3 carbon, and (c) mesoporous MgO, created by consecutive templating. The low-angle signatures confirm that the hexagonal (*p6mm)* pore arrangement is conserved in both replication steps. (Right) TEM/SAED diagram of mesoporous MgO.

Chem. Mater. **2008, 20, 961–971**   29
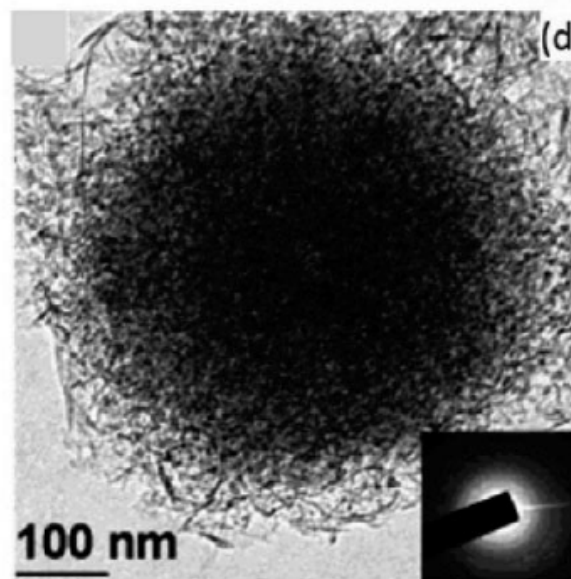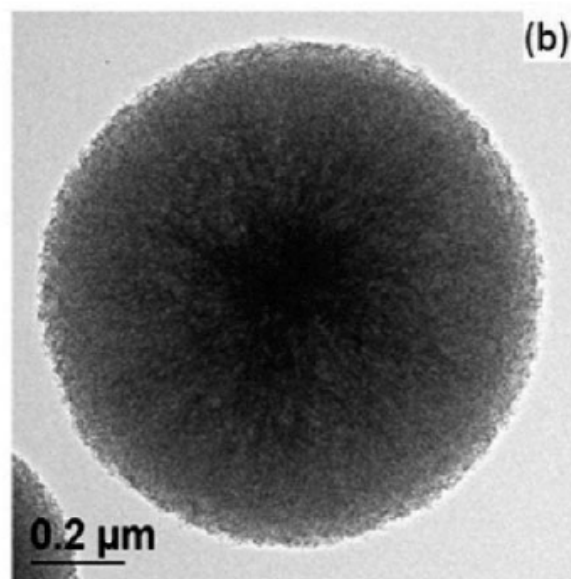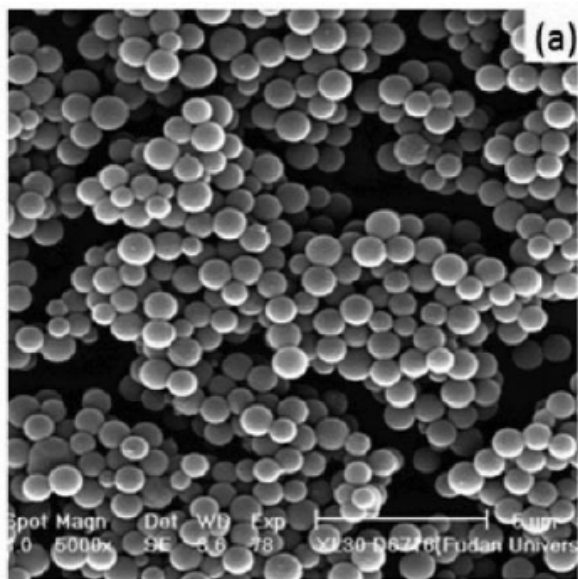
(a) SEM and (b) TEM images of mesoporous carbon spheres and TEM images of (c) ZrO$_2$ and (d) Al$_2$O$_3$ replicas

Chem. Mater. **2008, 20, 961–971**

30

Techniques for characterization of nano-porous materials

Crystalline structure

- Single crystal & Powder X-ray diffraction (XRD)
- Electron crystallography

Surface area & Pore size

- N_2 adsorption-desorption isotherm
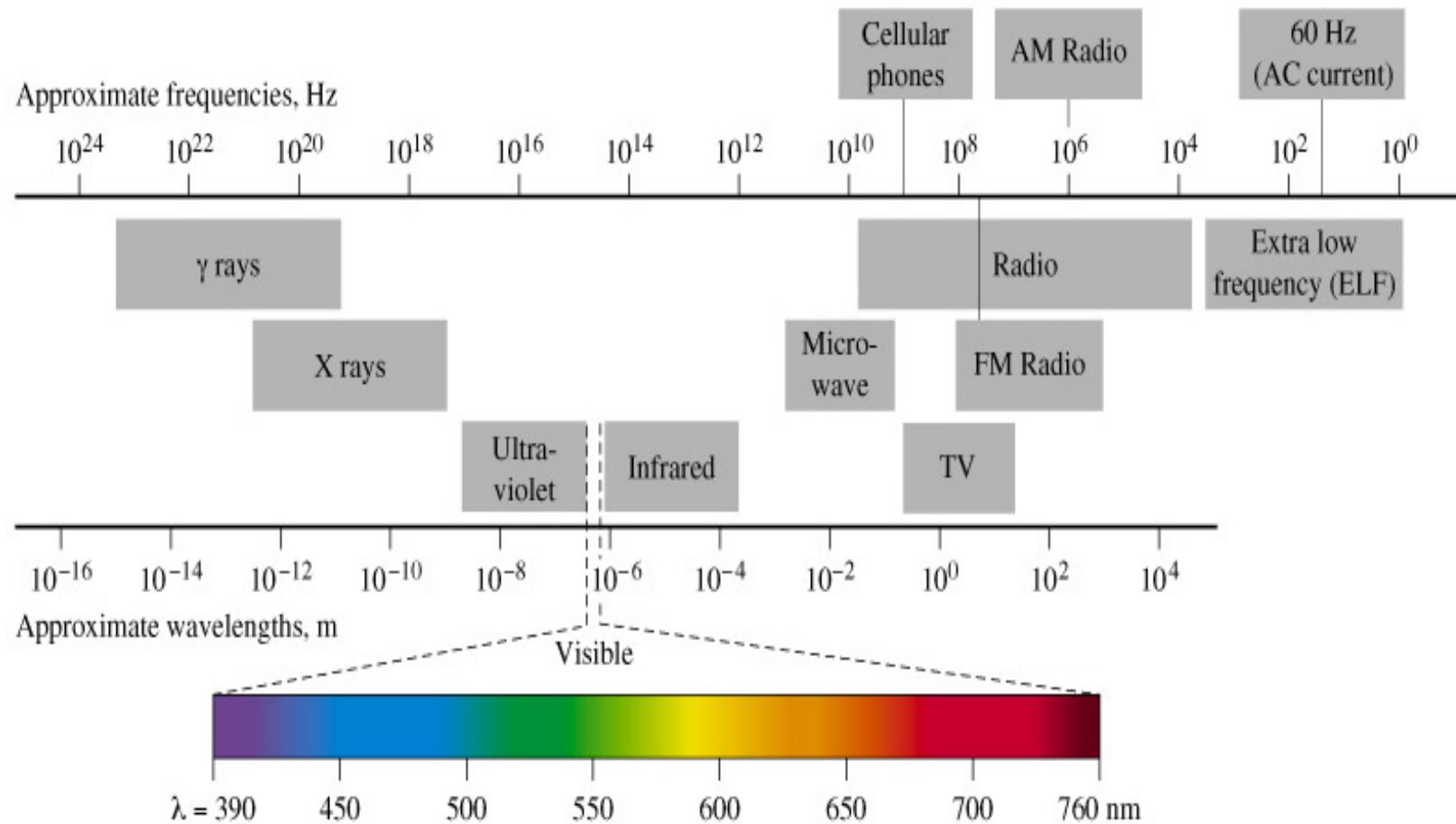- Mercury Intrusion Porosimetry
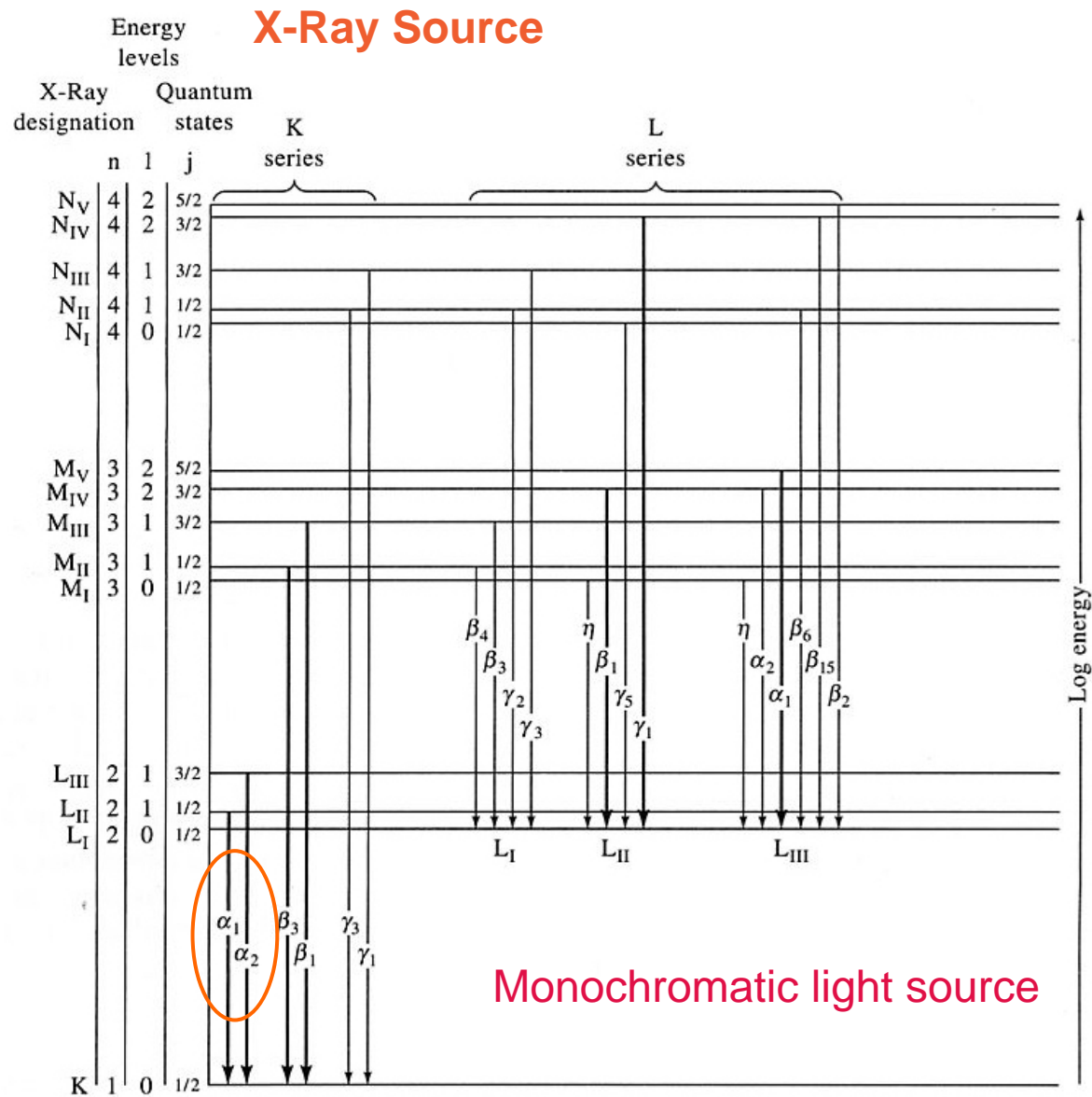
Pore structure- TEM

Morphology- SEM

Oxidation state & Coordination

- X-ray absorption spectra
- X-ray photoelectron spectra (XPS & Auger)
- Solid state NMR (mainly coordination)
- IR & Raman (mainly coordination)
- UV-Vis spectra

Elemental analysis- ICP-AES, XPS, EDX

The Electromagnetic Spectrum

Approximate frequencies, Hz

10^{24} 10^{22} 10^{20} 10^{18} 10^{16} 10^{14} 10^{12} 10^{10} 10^{8} 10^{6} 10^{4} 10^{2} 10^{0}

Cellular phones — AM Radio — 60 Hz (AC current)

γ rays

X rays

Radio — Extra low frequency (ELF)

Micro-wave — FM Radio

Ultra-violet — Infrared — TV

10^{-16} 10^{-14} 10^{-12} 10^{-10} 10^{-8} 10^{-6} 10^{-4} 10^{-2} 10^{0} 10^{2} 10^{4}

Approximate wavelengths, m

Visible

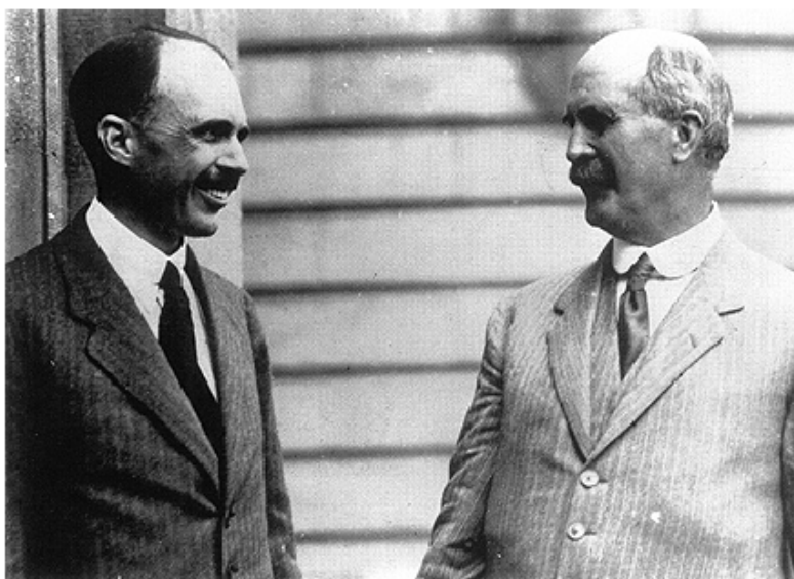$\lambda = 390$ 450   500   550   600   650   700   760 nm

X-Ray Source

Monochromatic light source

Figure 12-4 Partial energy-level diagram showing common transitions producing X-rays. The most intense lines are indicated by the wider arrows.

33

William Lawrence Bragg (left) and William Henry Bragg.

In 1912 Max von Laue reported the diffraction of X rays by a crystal (for which he received a Nobel Prize in physics in 1914). The elder Bragg and his son, who was by then a doctoral student with J. J. Thomson at Cambridge, began exploring this phenomenon immediately. They brought different interests and skills to the collaboration. William Henry's original interest was in what diffraction showed about the nature of X rays, and he was a skilled experimenter and designer of instruments. William Lawrence was more concerned with what X rays revealed about the crystalline state, and he possessed a powerful ability to conceptualize physical problems and express them mathematically. Simple inorganic crystals like sodium chloride were the subjects of the original studies in X-ray crystallography. Here the surprising result was that in the solid state these ionic compounds did not exist as paired positive and negative ions. Sodium chloride, for instance, did not exist as NaCl units; rather, Na and Cl alternated in a regular fashion in the crystal lattice.

In 1915, Bragg received the Nobel Prize.
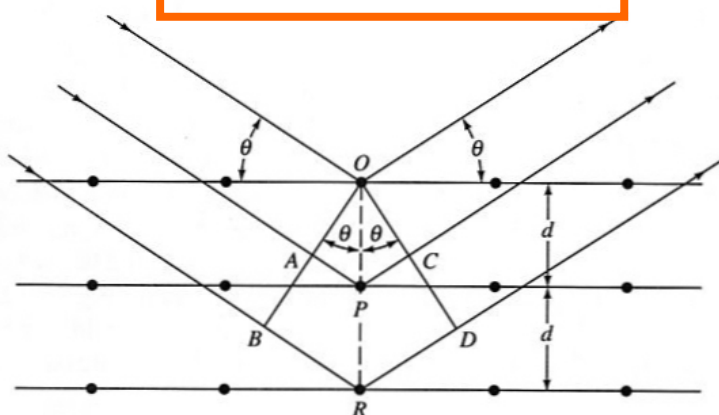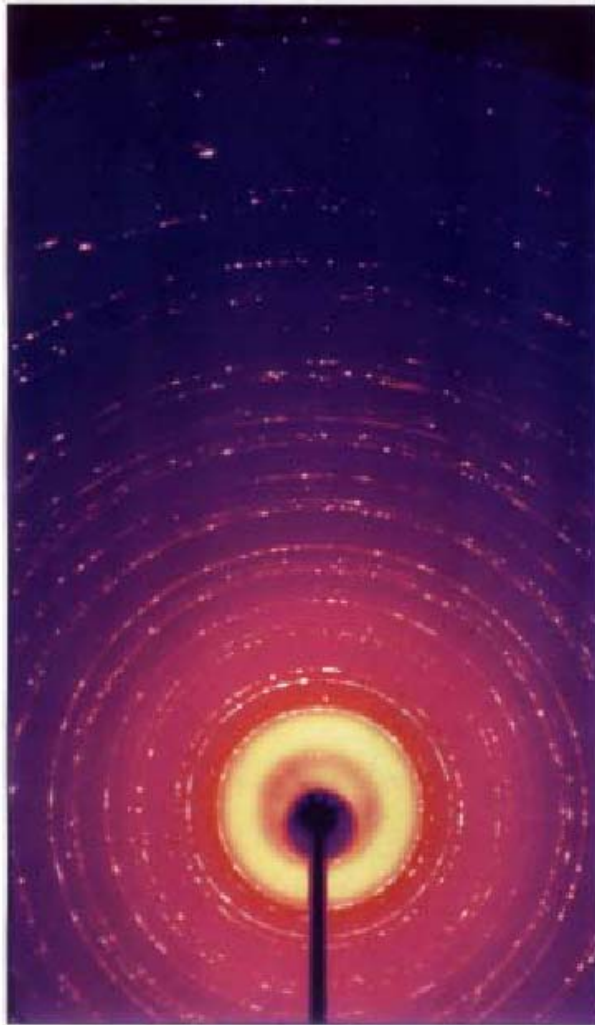
Bragg's Law
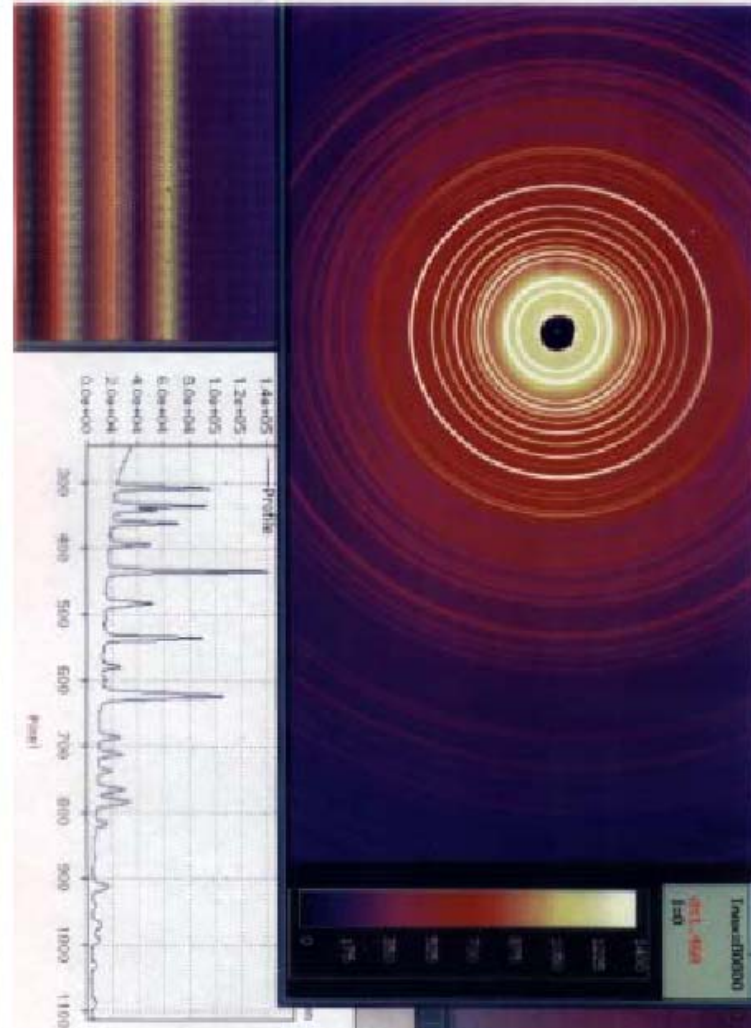
$$2d \sin\theta = n \lambda$$

Figure 12-6   Diffraction of X-rays by a crystal.
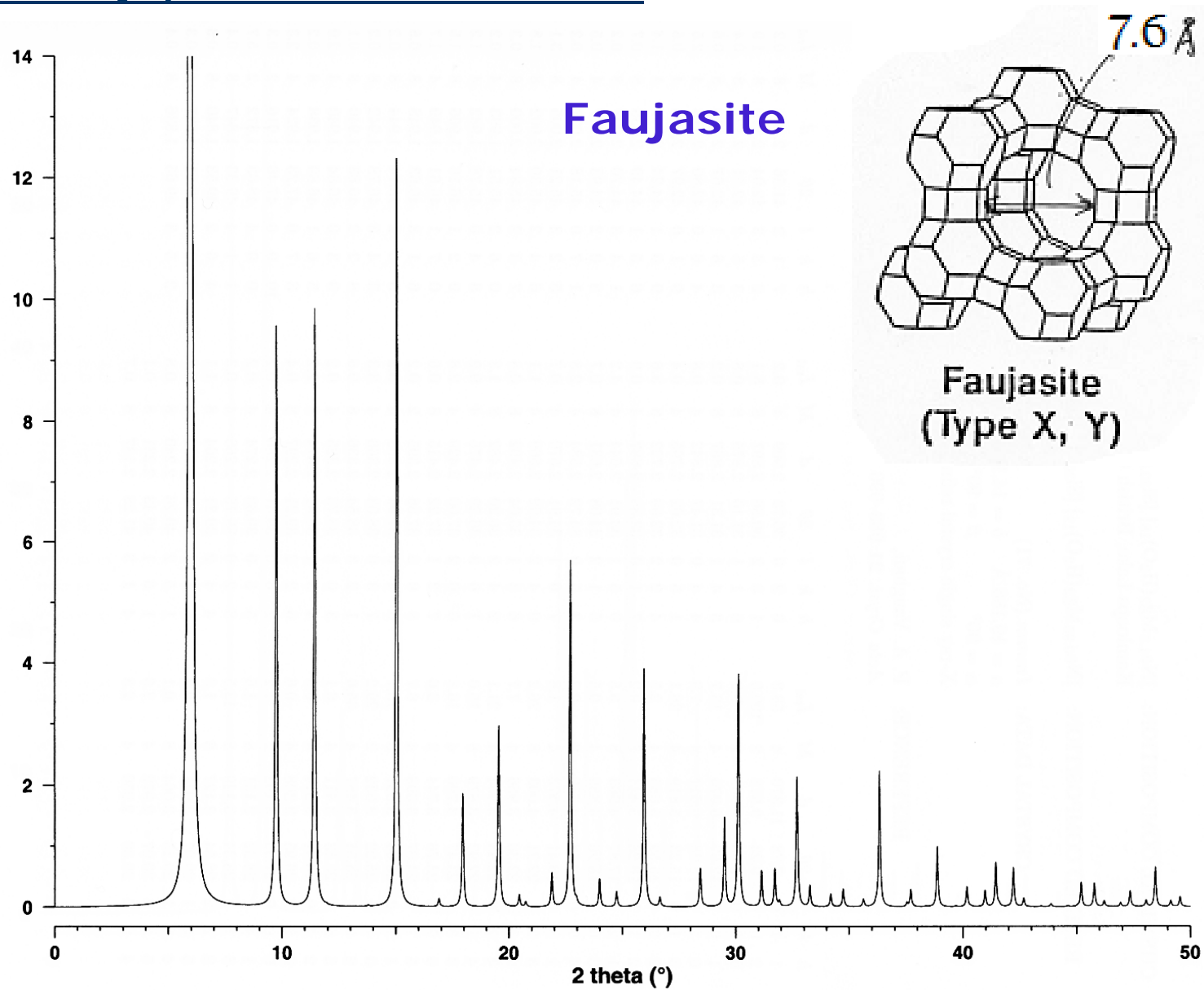
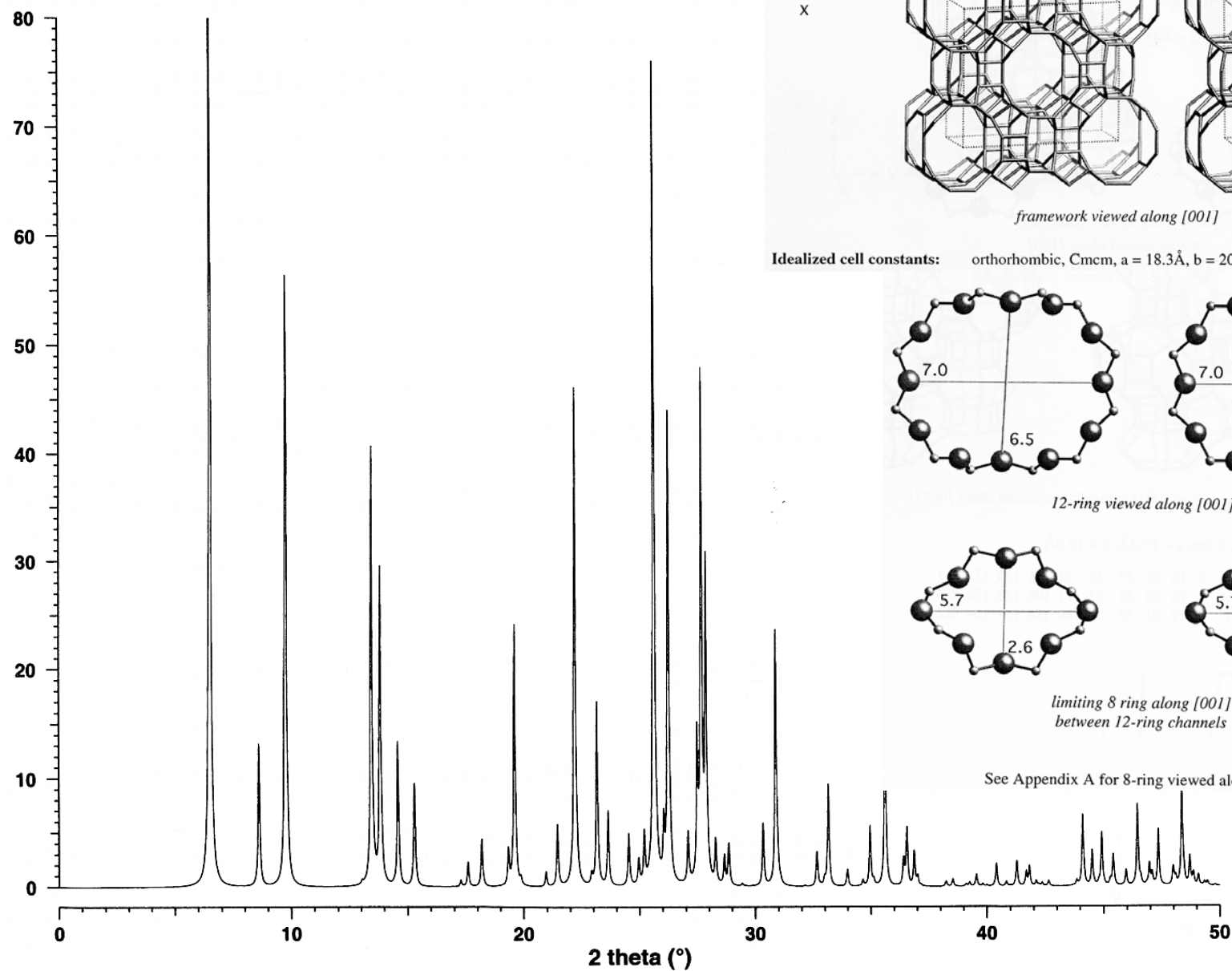34

X-Ray Diffraction Image & Pattern

Single crystal

Powder

X-ray powder diffraction

Faujasite

7.6 Å

Faujasite
(Type X, Y)

Mordenite

framework viewed along [001]

Idealized cell constants: orthorhombic, Cmcm, a = 18.3Å, b = 20.5Å, c = 7.5Å

12-ring viewed along [001]

limiting 8 ring along [001]
between 12-ring channels

See Appendix A for 8-ring viewed along [010]

2 theta (°)

As-synthesized

ZSM-5

(010)   (100)

calcined
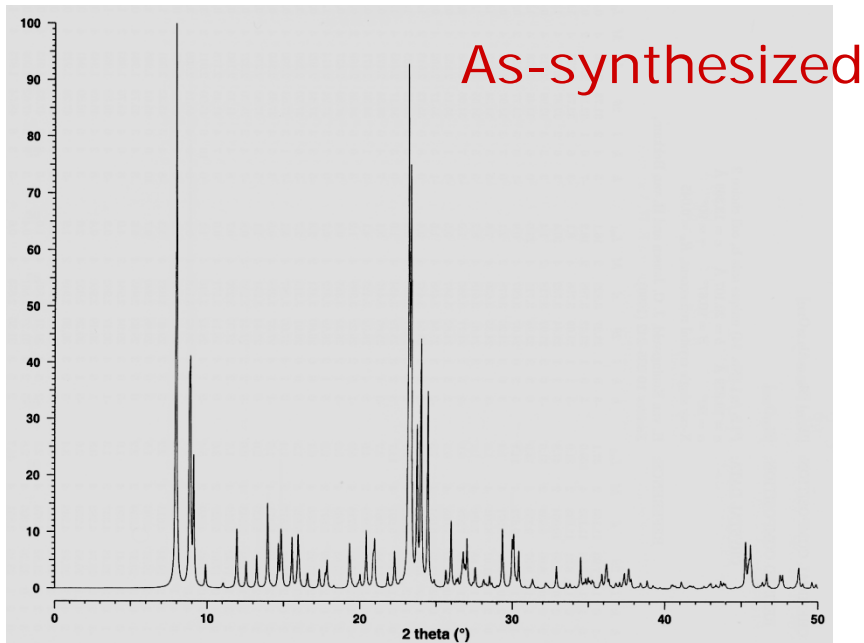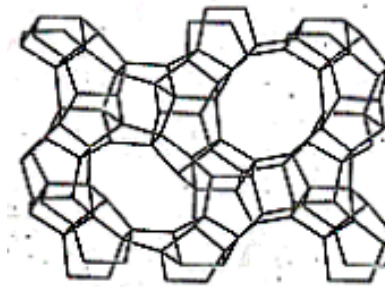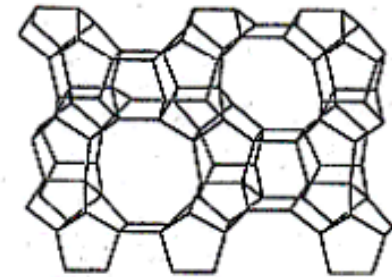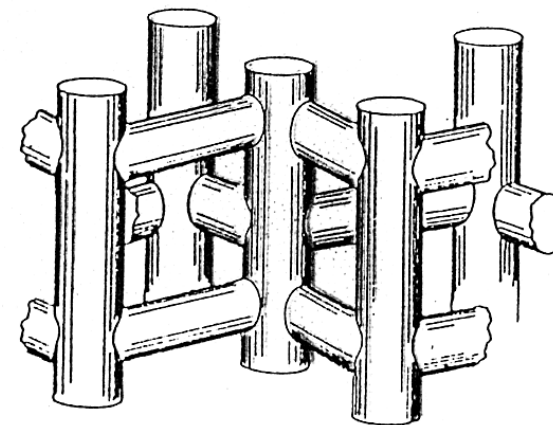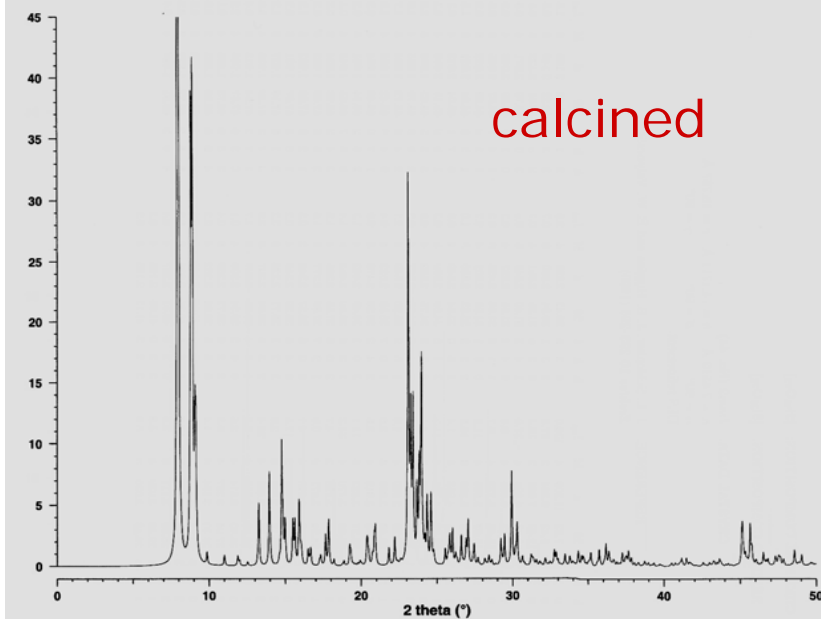
Fig. 4 The channel structure in ZSM-5.

Discovery of M41S Family
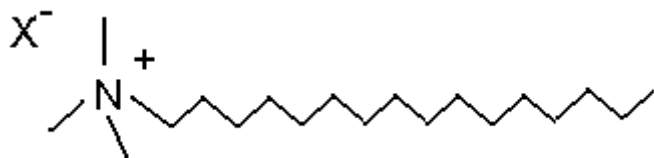
Surfactant: C$_{16}$TMABr

M41S
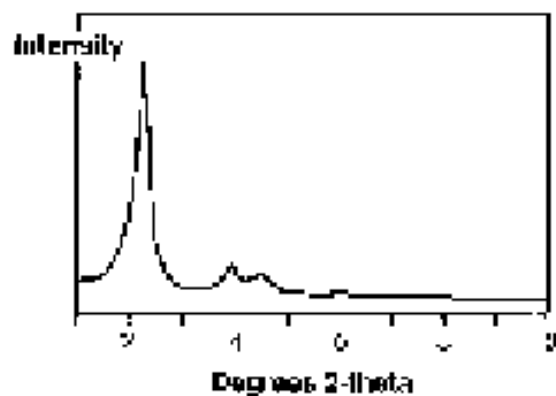
MCM-41
Hexagonal
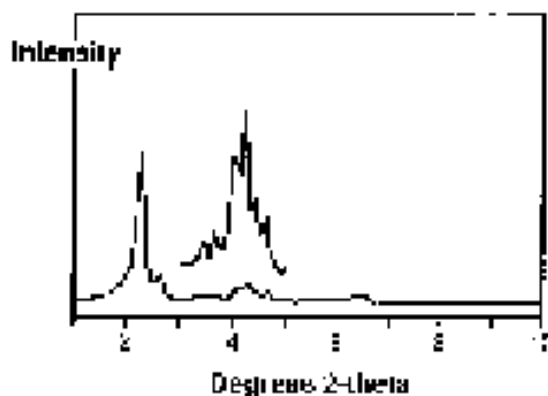
MCM-48
Cubic
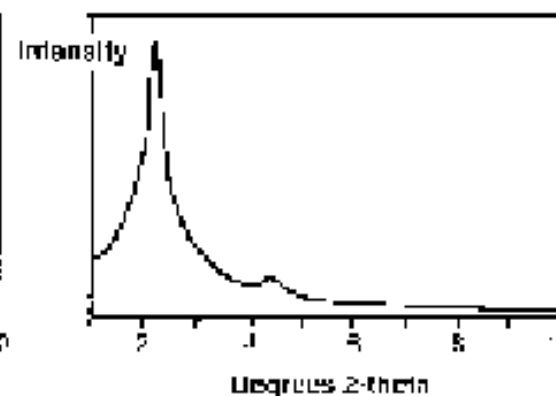
MCM-50
Lamellar

Increasing $\dfrac{Sur}{SiO_2}$

SBA-15

D. Zhao *et al. Science*, **1998**, *279*, 548.

hkl	d(Å)
100	104
110	60.0
200	52.0
210	39.4
300	34.6
220	30.0
310	28.5

hkl	d(Å)
100	95.7
110	55.0
200	47.7
300	31.7
220	27.5
310	26.5

PEO-PPO-PEO
Triblock-copolymer

hydrophilic media

Micelle
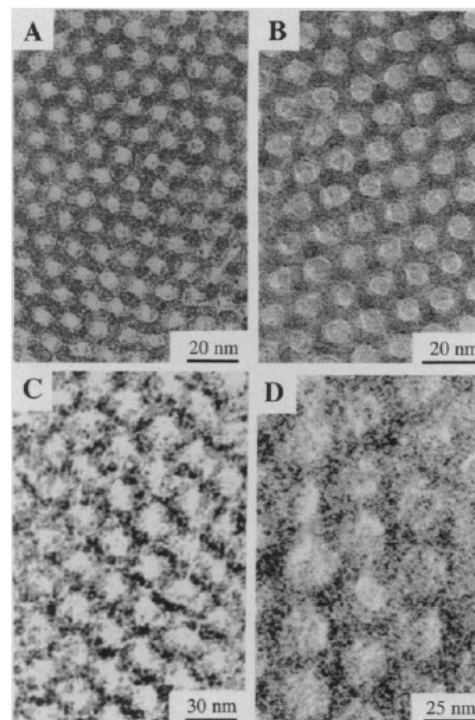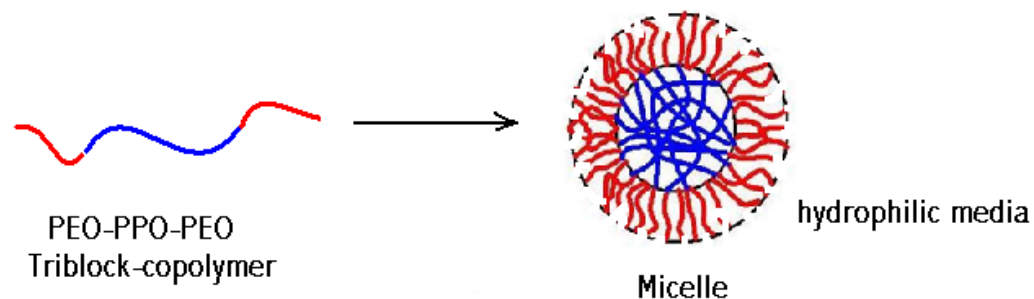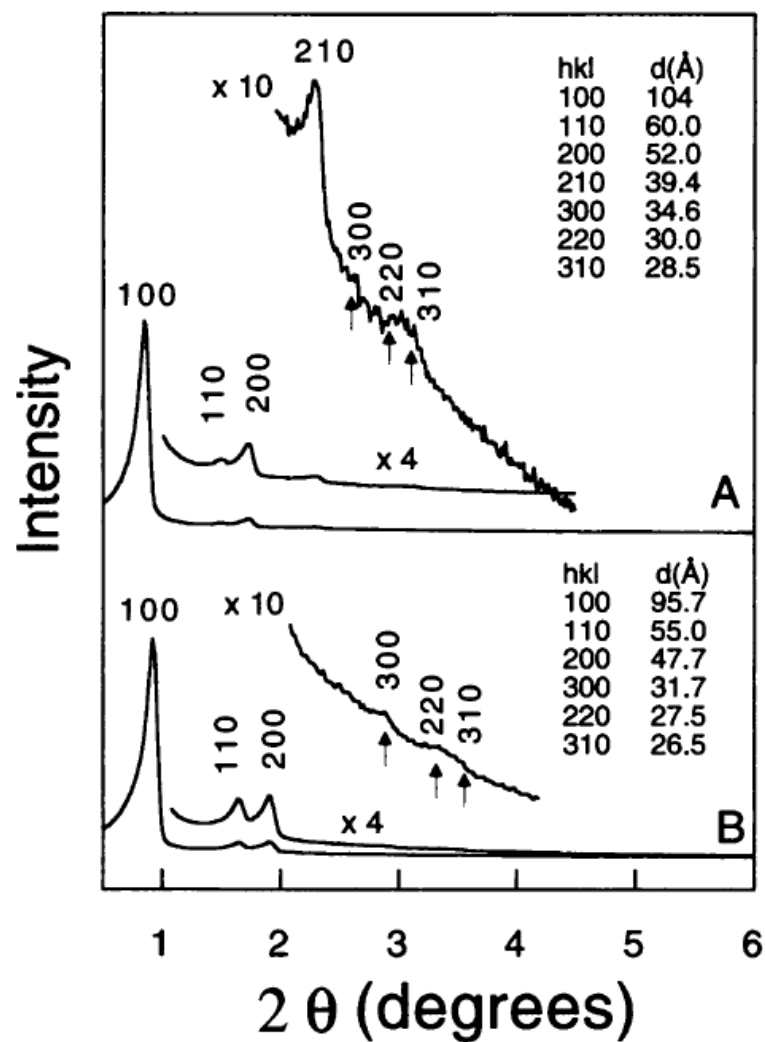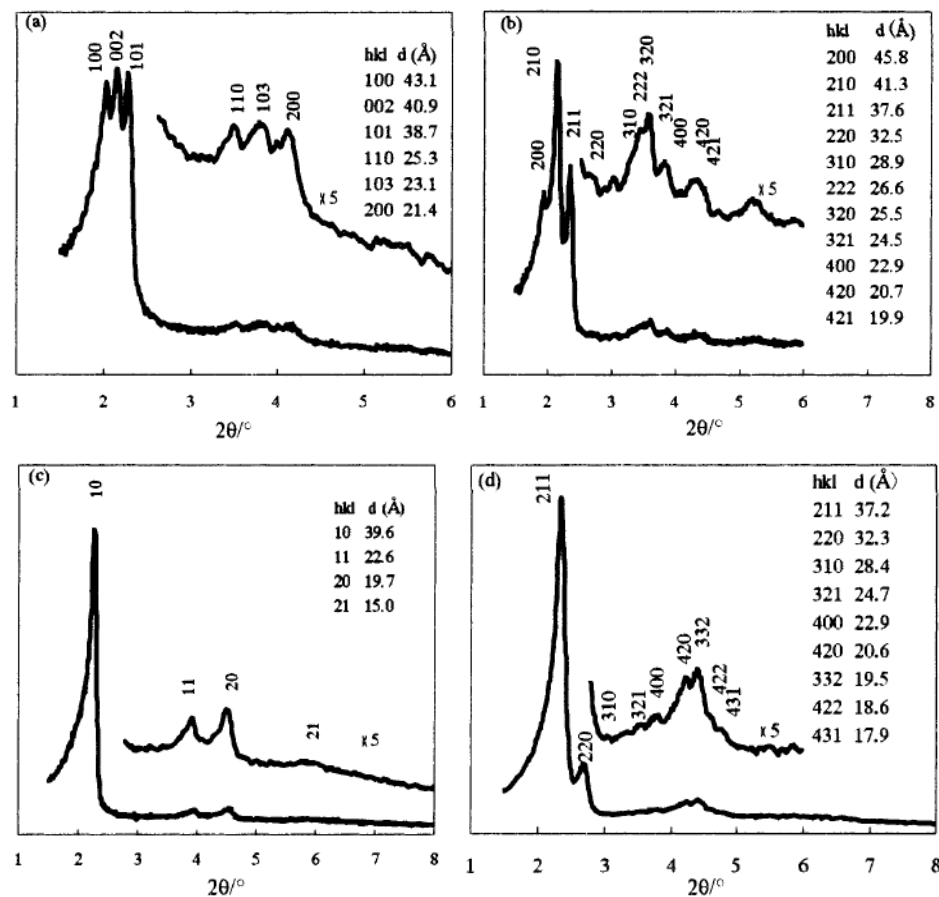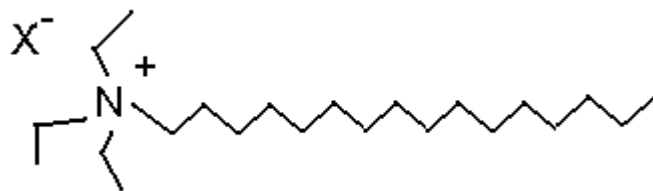
XRD patterns of as-synthesized materials synthesized with CTEABr & various acids: (a) H_2SO_4, (b) HCl, (c) HBr, and (d) HNO_3

Che et al. J. Am.Chem. Soc. **2002**, *124, 13963*

41

Carbon Molecular Sieve
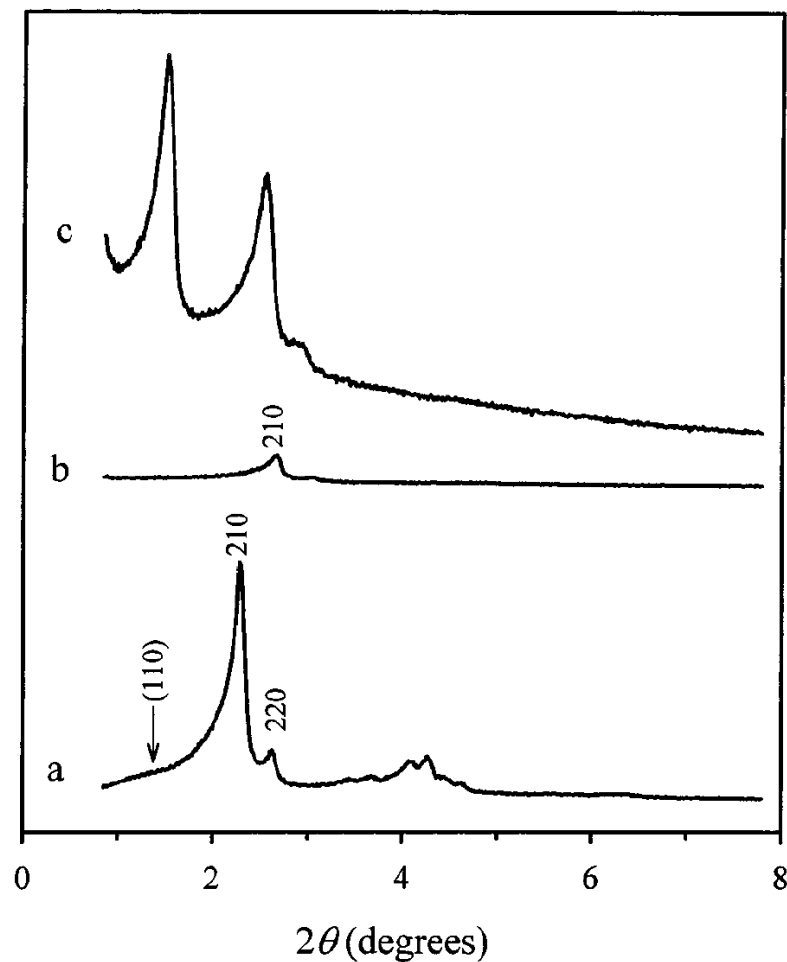
Figure 2. Changes in powder X-ray diffraction patterns during synthesis of the carbon molecular sieve CMK-1 with its silica template MCM-48: (a) The mesoporous silica molecular sieve MCM-48, (b) MCM-48 after completing carbonization within pores, and (c) CMK-1 obtained by removing silica wall after carbonization. These XRD patterns were obtained using a Rigaku D/MAX-III (3 kW).
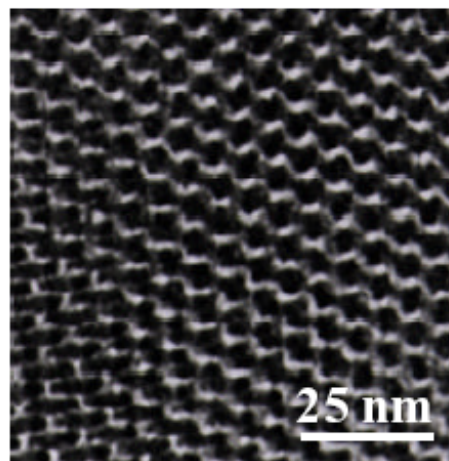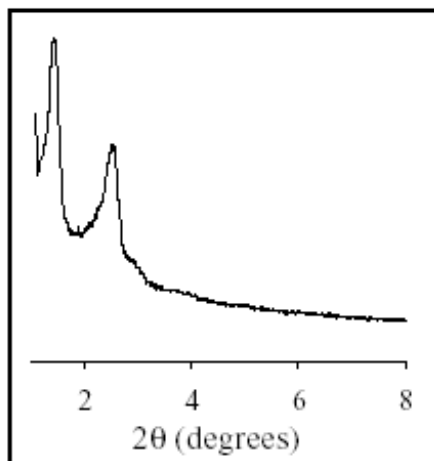
Fig. 2. XRD pattern and TEM image of CMK-1 carbon after the complete removal of template.

MCM-48
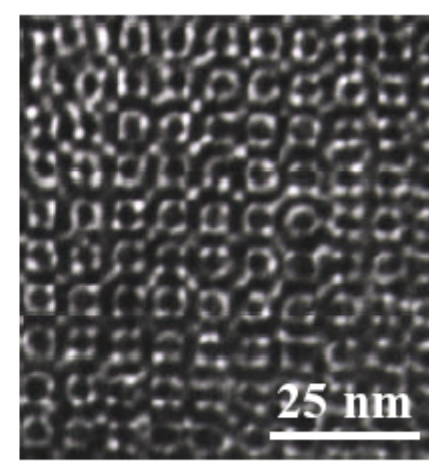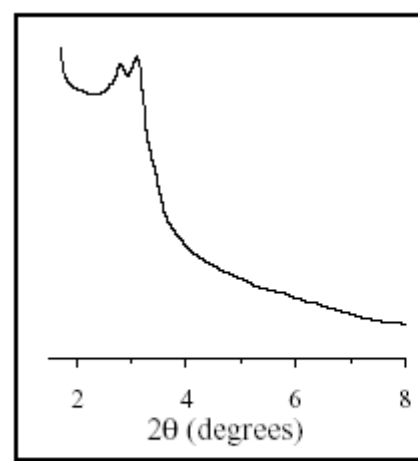
Fig. 3. XRD pattern and TEM image of CMK-2 carbon after the complete removal of template.
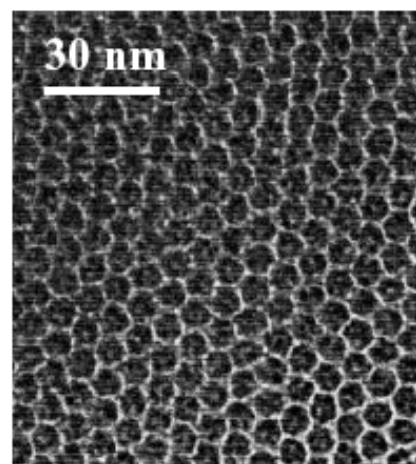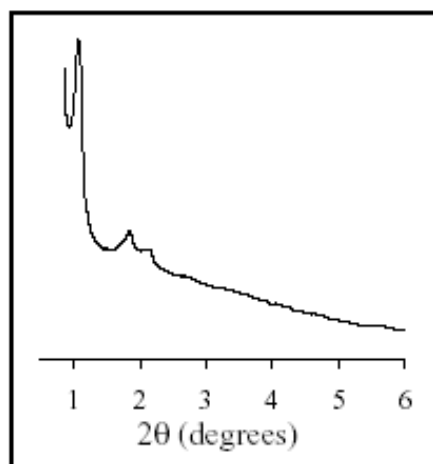
SBA-1

Fig. 4. XRD pattern and TEM image of CMK-3 carbon after the complete removal of template.

SBA-15

Overlapping of peaks ⇒

Difficulties in solving the crystal structure from X-ray powder diffraction patterns
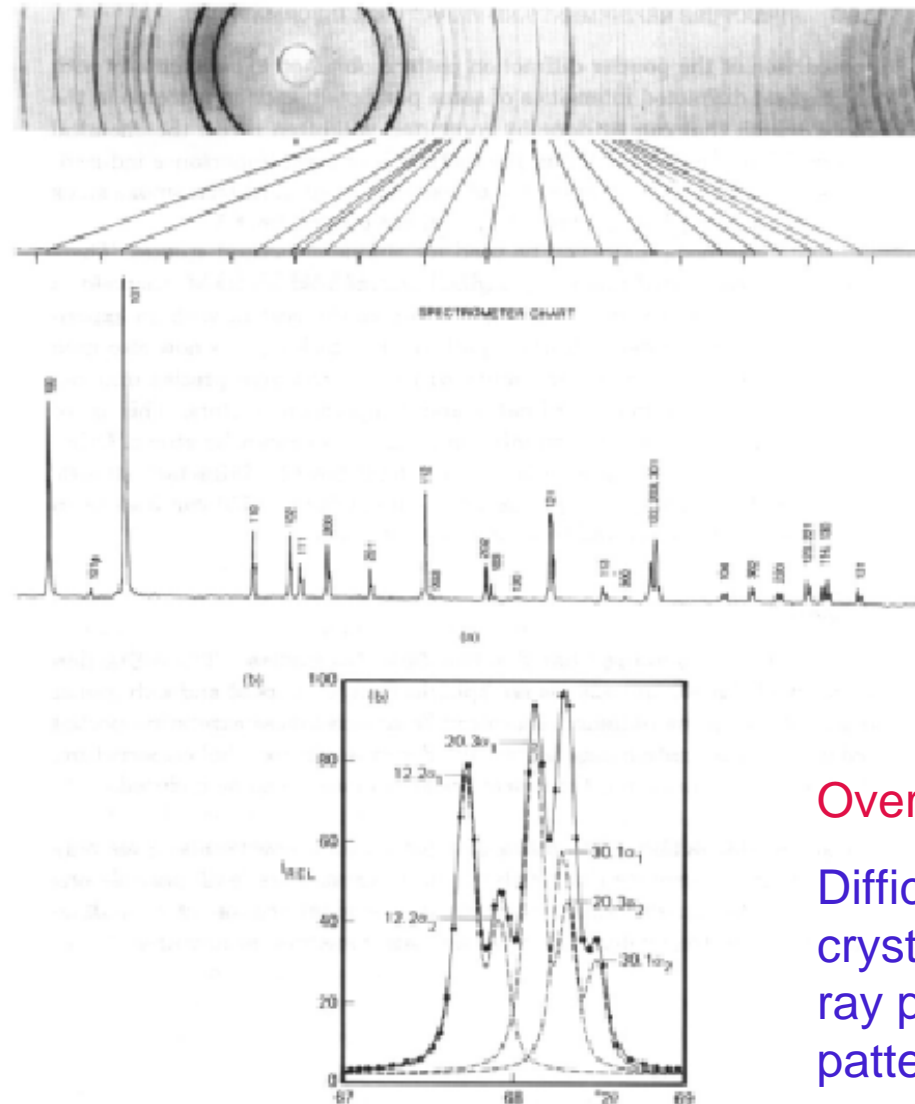
FIGURE 13.3 Powder Diffraction.

(a) Comparison of an 11.46-cm diameter powder camera film (upper photograph) with a scanned diffractometer pattern of quartz (with copper $K\alpha$-radiation) 12.2, 20.3, and 30.1 represent, respectively, the 122, 203, and 301 reflections for this crystal.

(b) Profile fitting of a portion of the diffraction pattern of quartz. Dots are experimental points from step-scanning and dashed lines are the individual results for each reflection. The sum is represented by a solid line. Note the separation of the α_1 and α_2 wavelengths of the radiation.
(Photographs and diagram courtesy of Dr. William Parrish.)

44

Particle Size Determination from XRD peaks

- The width of the peaks in a powder pattern contain information about the crystallite size in the sample (and also the presence of microstrain)

- $L = (K \lambda / \beta \cos \theta)$: Scherrer equation

  - L - mean size of crystallites
  - K - constant roughly 1: depends on shape of crystallites
  - β - width of reflection in radians

XRD Pattern of Meso-Porous ZrO$_2$
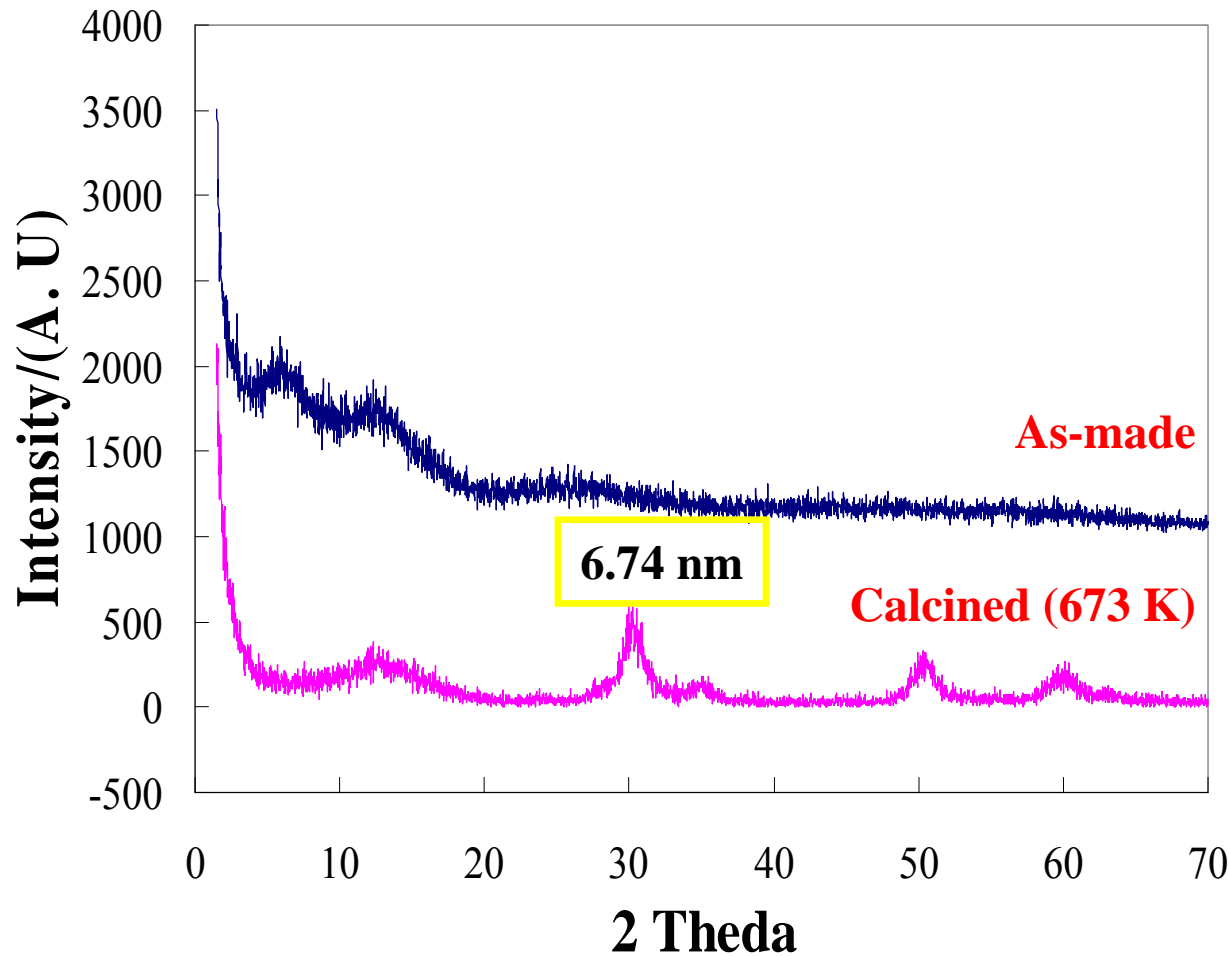
Scherrer Equation

$$d = \frac{K\lambda}{\beta_{1/2}(\cos\theta)}$$

$\beta_{1/2} = \sqrt{(B^2 - b^2)}$
(calibrated peak width at half maximum)

B = *peak width at half maximum*

b = *instrumental peak width*
(~0.16 for NaCl$_{(s)}$)

46

Electron diffraction patterns & micrographs
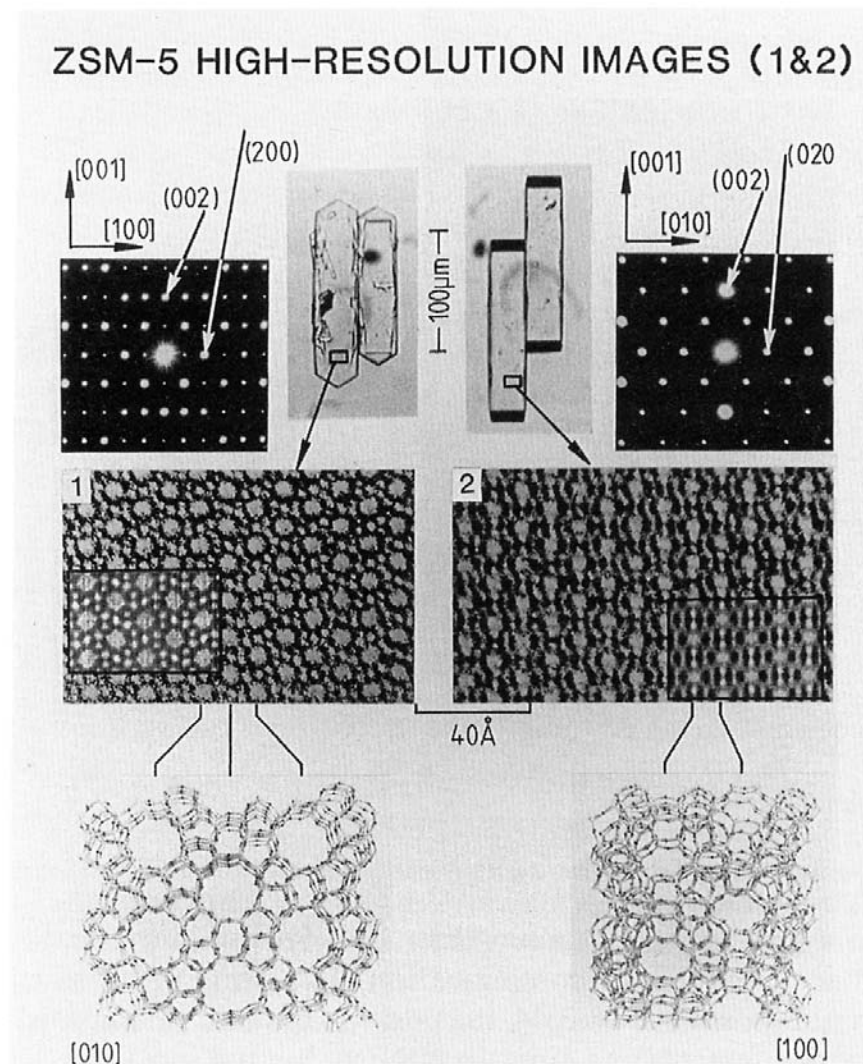
Figure 3.46 High-resolution micrographs (middle) together with selected-area diffraction patterns and optical micrographs of ZSM-5 looking down the [010] direction (top left) and the [100] direction (top right). Corresponding views of the structural model are shown at the bottom. (Based on work of G. R. Millward and J. M. Thomas).

47

Electron diffraction crystallography

Resolution of
Electron Microscopy

Wave length of
visible light

Wave length
of X-ray

Wave length
of electron

de Broglie relation

$$\lambda = h / mv$$

100

.1Å

d

Structures of
Mesoporous

Diameters of
Pore & Cage are
20-500 Å

Framework
Structure of
Zeolites

Bond distances,
T-O = 1.6
T-(O)-T= 3 Å

Atomic Coordinates

Atomic coordinates are
obtained by statistical
treatment from many
reflections up to large
scattering vectors.

Fig. 1   Schematic Length Scale

B

A

B

B

A

A

A

B

A

B

A

B

A

B

B

146 Å

B
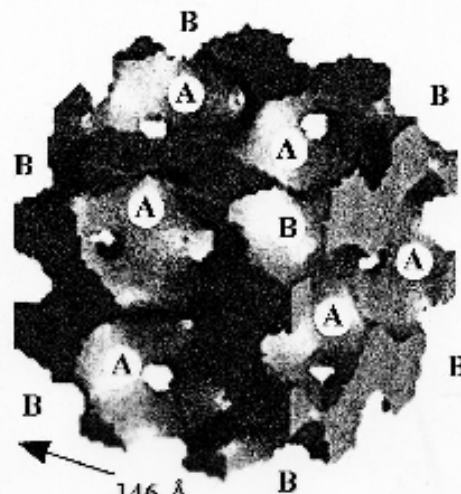
Fig. 6   Structure solution of SBA-6. Pm-3n.

48

Structural Solution of Mesocaged Material AMS-8

Alfonso E. Garcia-Bennett,* Keiichi Miyasaka, and Osamu Terasaki
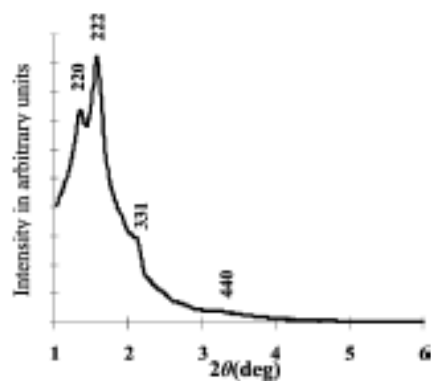
Figure 1. X-ray diffraction pattern of calcined AMS-8 cubic mesocaged structure with unit cell parameter $a = 183.4$ Å.
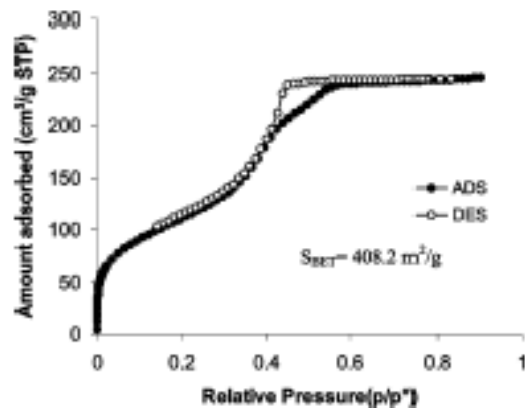
Figure 2. Nitrogen adsorption−desorption isotherm of calcined AMS-8. The isotherm shows a relatively broad capillary condensation step accompanied by a marked hysteresis effect in desorption branch of the isotherm.
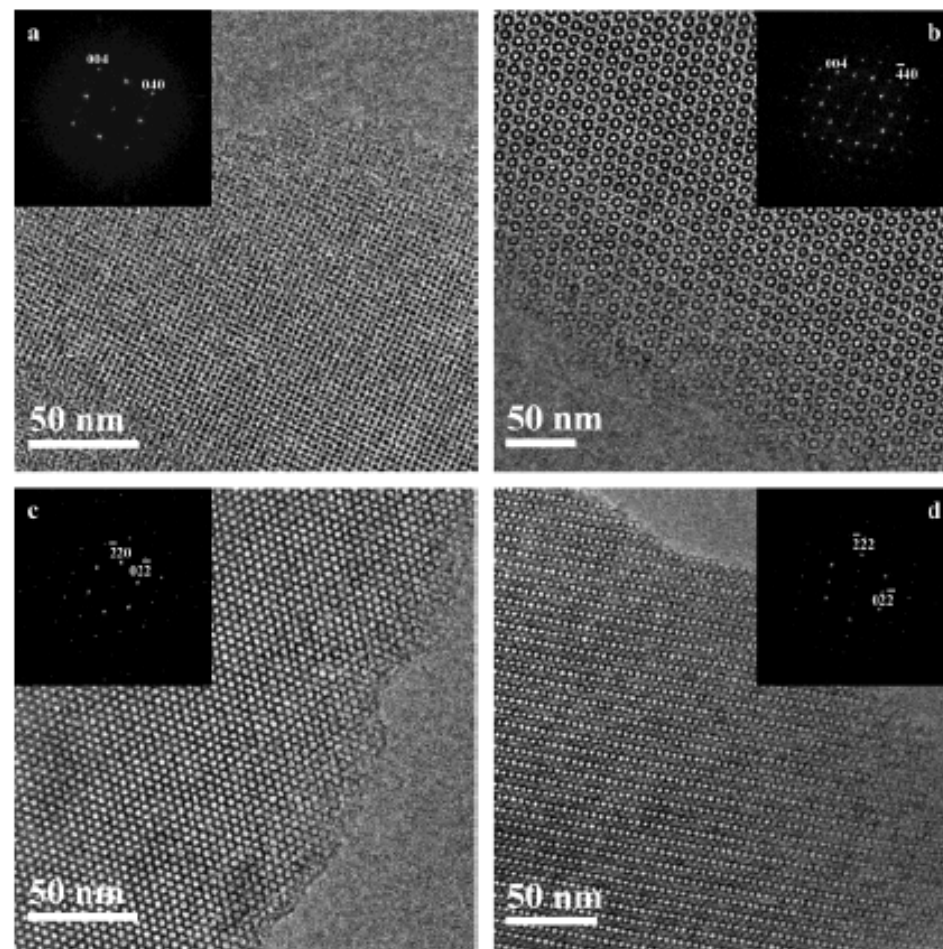
Figure 3. Typical HRTEM images and corresponding FT diffractograms of calcined AMS-8 recorded with (a) [100], (b) [110], (c) [111], and (d) [211] incidence. Diffractograms are indexed on the basis of a cubic unit cell, $a = 177.9$ Å. All images show large ordered regions indicative of a well-structured material.

49
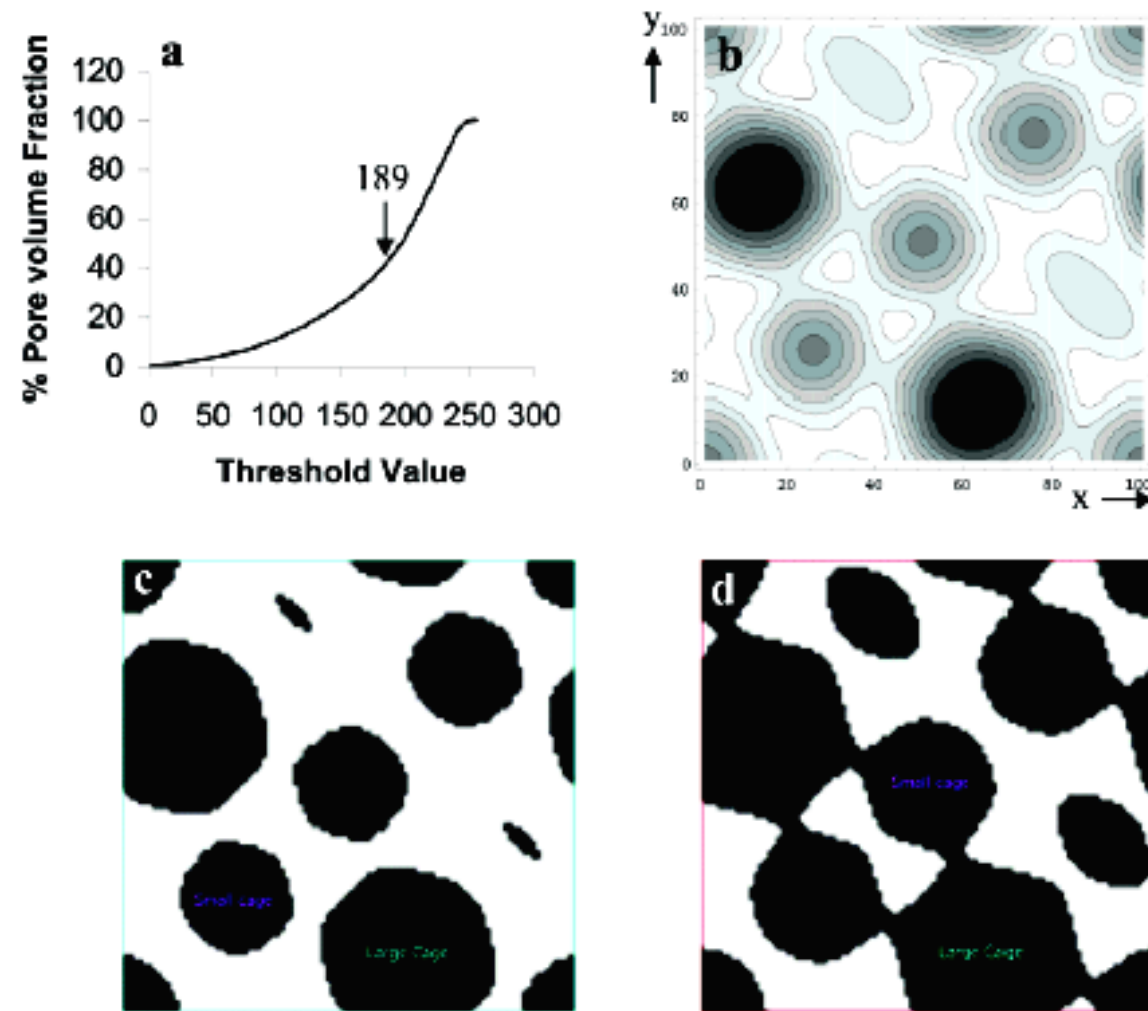
Figure 4. Plot of pore volume fraction versus potential density of the wall for mesocaged material AMS-8 (a), from which the 2D-sliced electrostatic potential density maps of the unit cell can be derived for the threshold range 150−256 (b) and the threshold values 189 (c) and 199 (d). The latter correspond to 44 and 50% pore volume fractions, respectively. The unit cells slices are taken with $z = 7$, where the unit cell has been divided into 100 slices (slice thickens = 1.834 Å). White contrast represents the silica wall and black contrast represents the pore space.

(100)

(110)

(111)
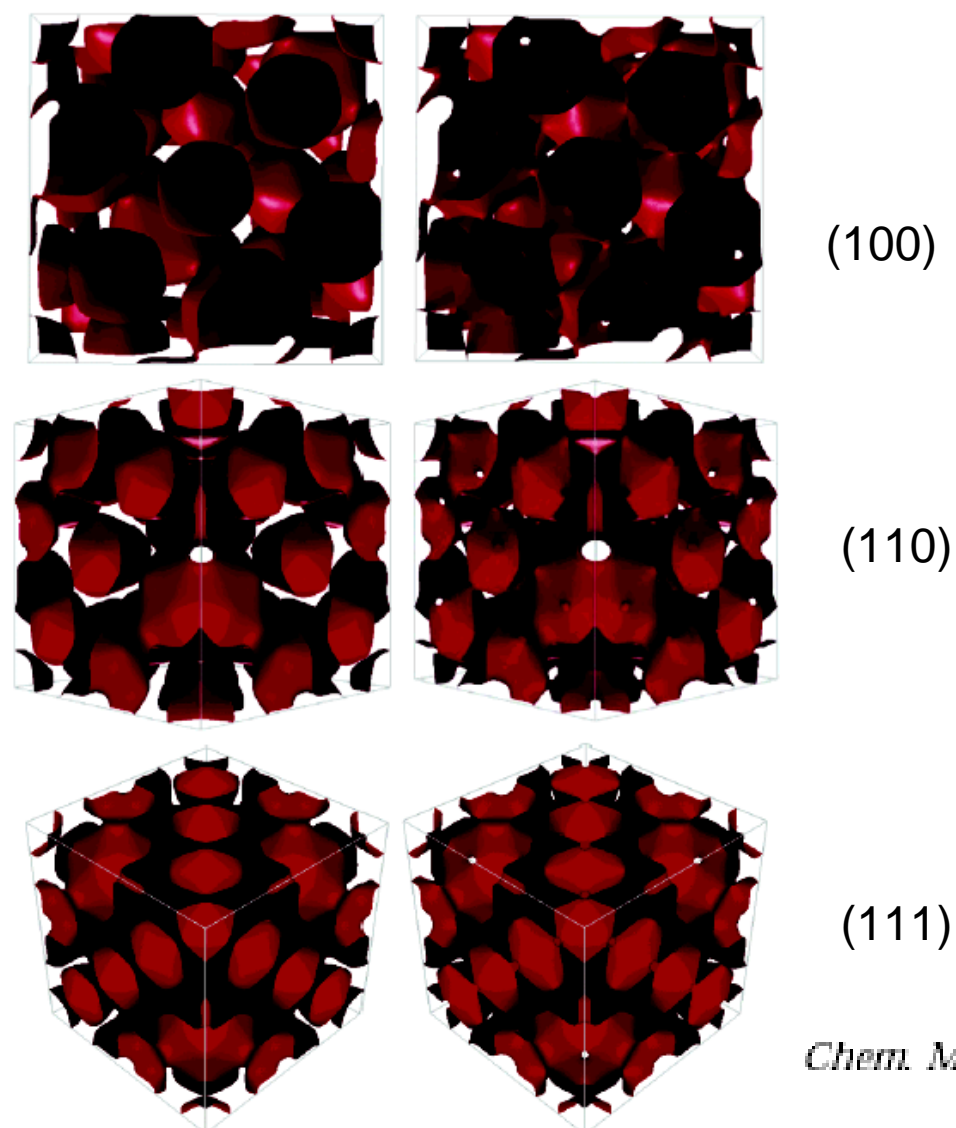
Figure 5. Electron density 3D reconstruction of the unit cell of AMS-8 viewed in perspective along the [100] (top), [110] (middle), and [111] (bottom) directions for threshold values 189 (left) and 199 (right). Only the outline of the cages is shown where light red corresponds to the interior surface of the cage. For threshold 189, large cages are connected via cavity windows to four additional large cages in a zigzag arrangement. This connecting window can be clearly seen as a pore opening parallel to the [110] orientation. Smaller cages are not connected. For threshold 199, large cages are connected to 12 individual smaller cages through small openings and to 4 additional larger cages through larger openings. Smaller cages are connected to each other through a single small pore opening.

51

Techniques for characterization of nano-porous materials

Crystalline structure

- Single crystal & Powder X-ray diffraction (XRD)
- Electron crystallography

Surface area & Pore size

- N_2 adsorption-desorption isotherm
- Mercury Intrusion Porosimetry

Pore structure- TEM

Morphology- SEM

Oxidation state & Coordination

- X-ray absorption spectra
- X-ray photoelectron spectra (XPS & Auger)
- Solid state NMR (mainly coordination)
- IR & Raman (mainly coordination)
- UV-Vis spectra

Elemental analysis- ICP-AES, XPS, EDX
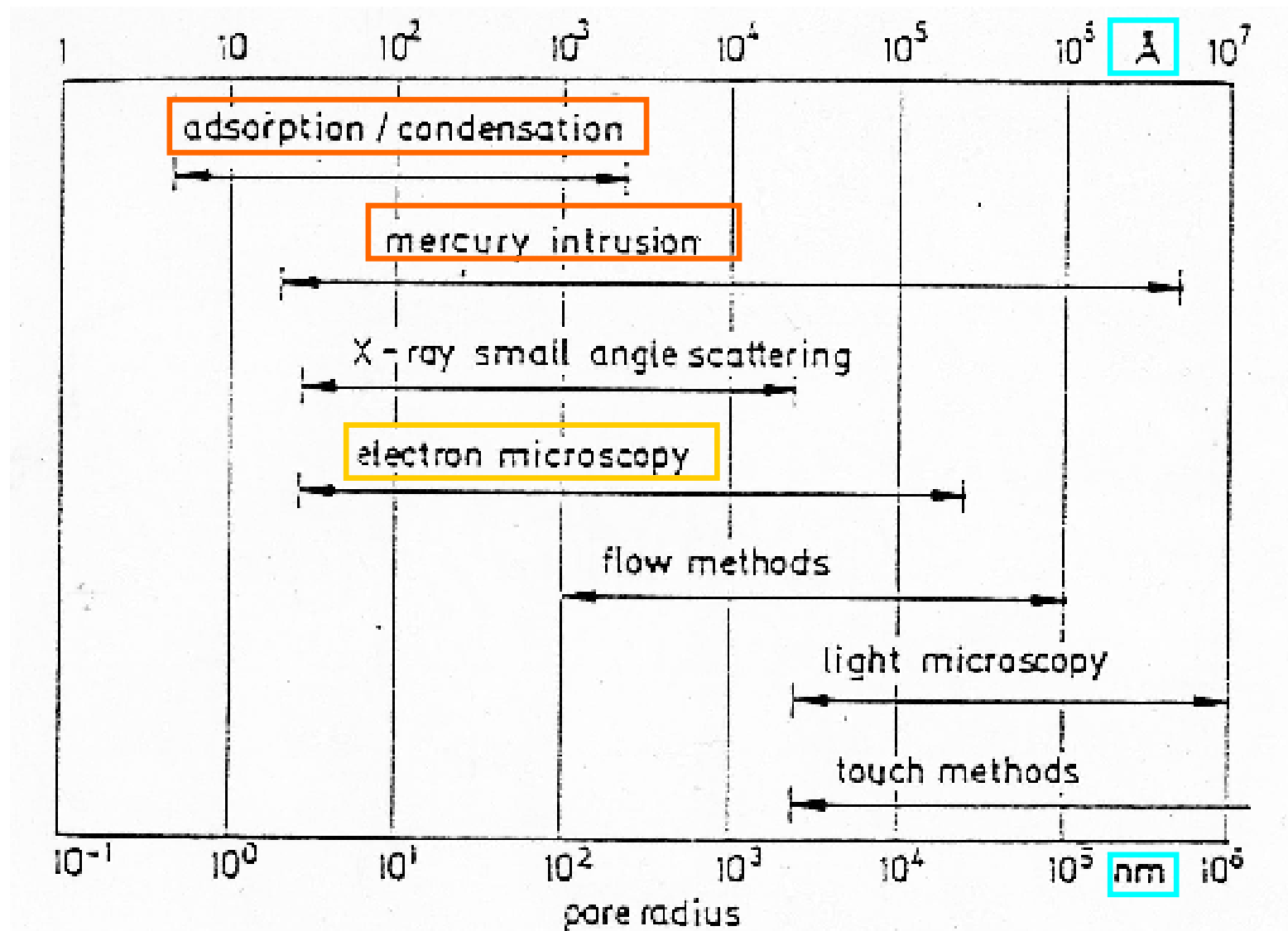
Survey on Pore Size Determination Methods

N$_2$ or Ar Adsorption-Desorption Isotherm
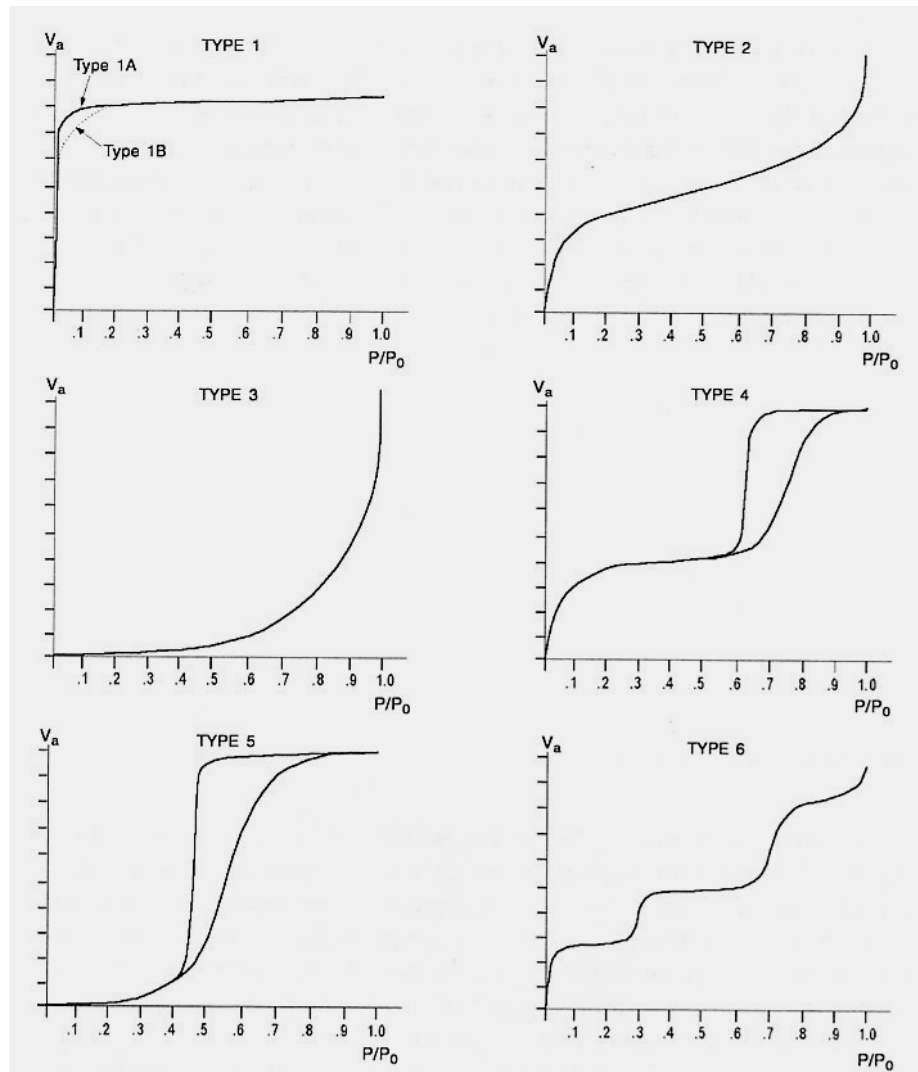
Figure 3.1. The six basic adsorption isotherm types.
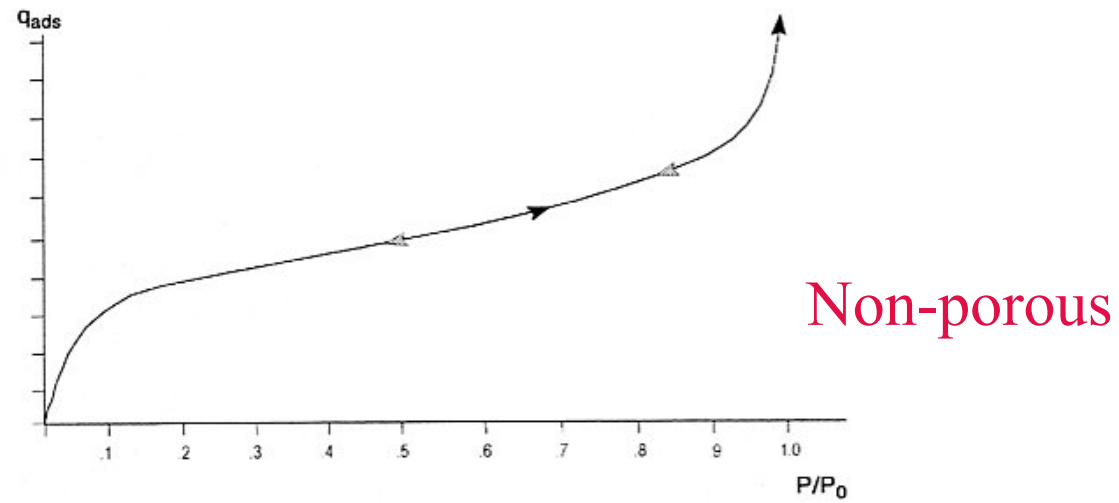
Figure 3.2. Adsorption and desorption isotherms for a nonporous solid.
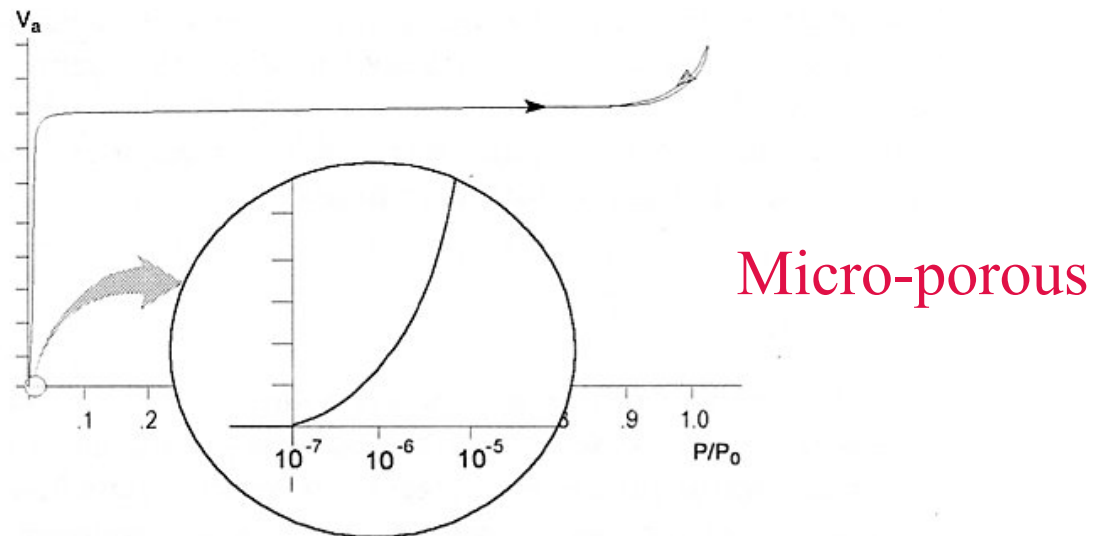
Non-porous

Figure 3.6. Adsorption and desorption isotherms for a microporous solid. The inset shows the steep rising region of the isotherm plotted on a logarithmic x-axis.

Micro-porous

55

b. N$_2$ adsorption -

Figure 3.2. Adsorption and desorption isotherms for a nonporous solid.

Non-porous

hysteresis

Desorption
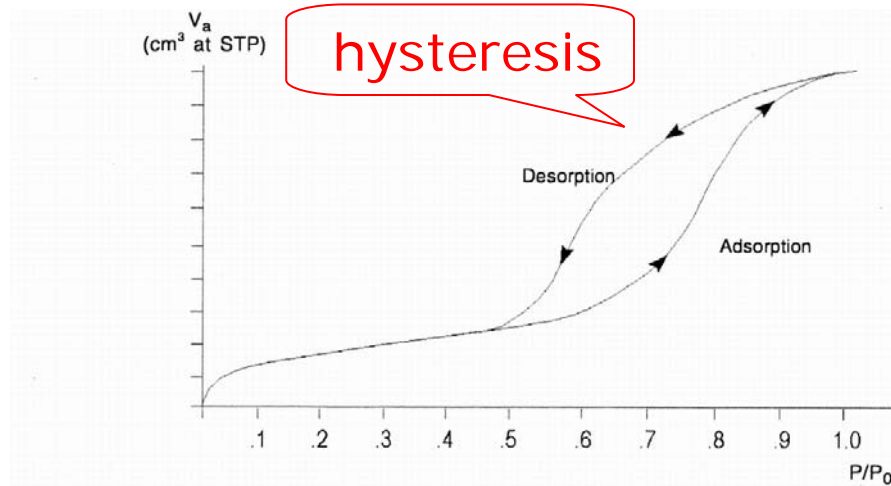
Adsorption

Figure 3.3. Adsorption and desorption isotherms for a porous solid.

Capillary condensation applicable to mesopore only

20 Å < d < 500 Å

56

Explanation for hysteresis

(1) Changes in Contact Angles upon Ads. & Des.

On adsorption,

According to Kelvin eq.
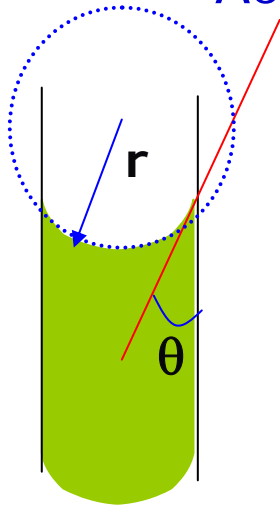
surface tension of liquid

molar volume of liquid

$$\ln \frac{P_a}{P_0} = -\frac{2\sigma \overline{V} \cos\theta}{RTr_k} \qquad \frac{P_a}{P_0} = e^{-2\sigma \overline{V} \cos\theta / RT\, r_k}$$

radius of empty pore

On desorption, $\theta = 0$, $\cos\theta = 1$

$$\ln \frac{P_d}{P_0} = -\frac{2\sigma \overline{V}}{RTr_k} \qquad \frac{P_d}{P_0} = e^{-2\sigma \overline{V} / RT\, r_k}$$

Since $\cos\theta \leq 1 \implies \dfrac{P_a}{P_0} > \dfrac{P_d}{P_0}$

r

θ

(2) Ink-bottle pores
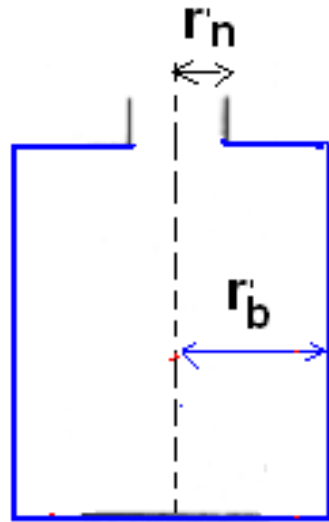
$r_n < r_b$
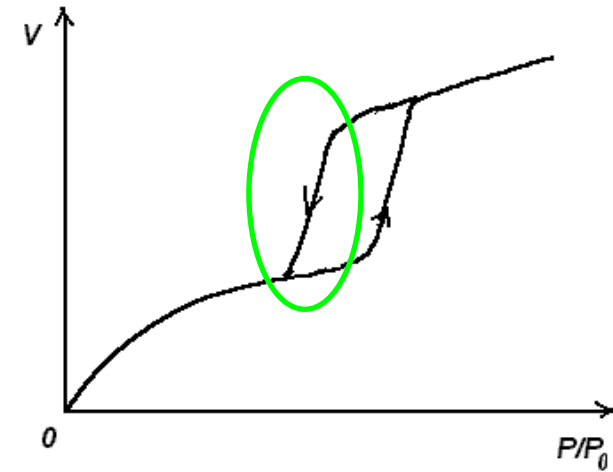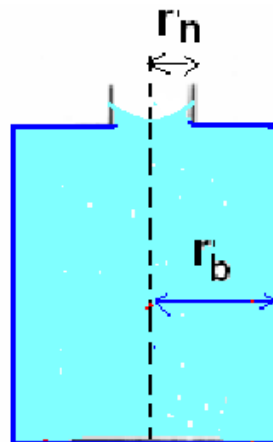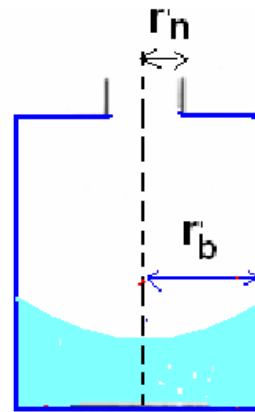
$$\frac{P_a}{P_0} = e^{-2\sigma\overline{V}/RTr_b}$$

$$\frac{P_d}{P_0} = e^{-2\sigma\overline{V}/RTr_n}$$

$$\Rightarrow \frac{P_a}{P_0} > \frac{P_d}{P_0}$$
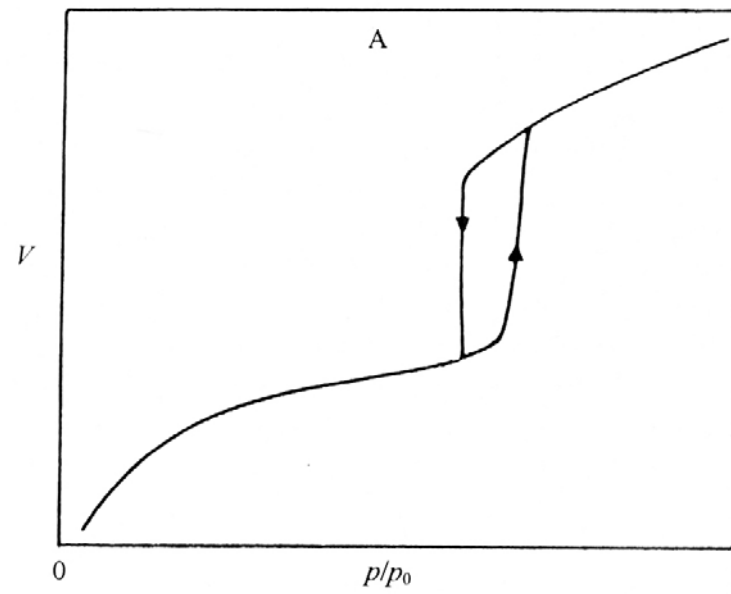
uniform narrow-distributed pores
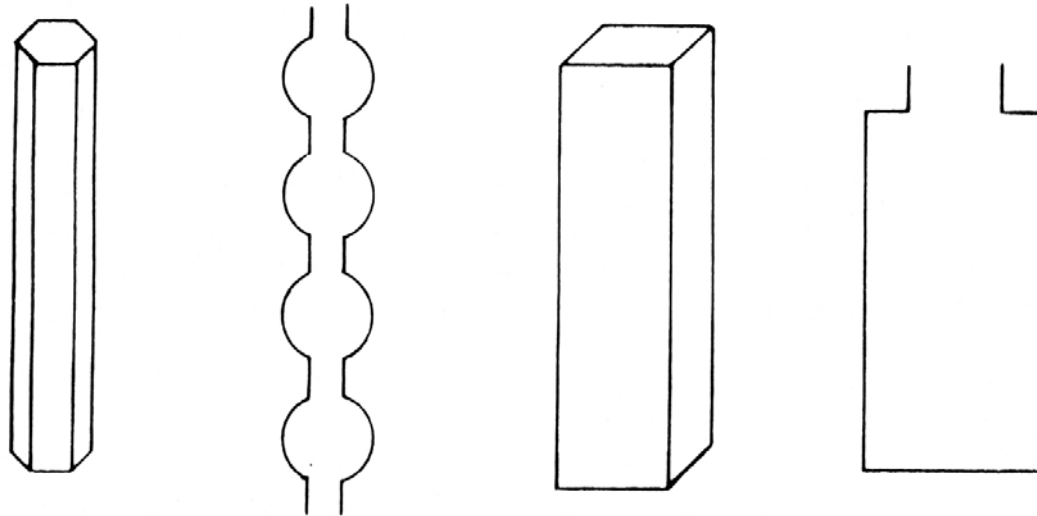
Figure 4.11 Type A hysteresis loop and possible pore structures.
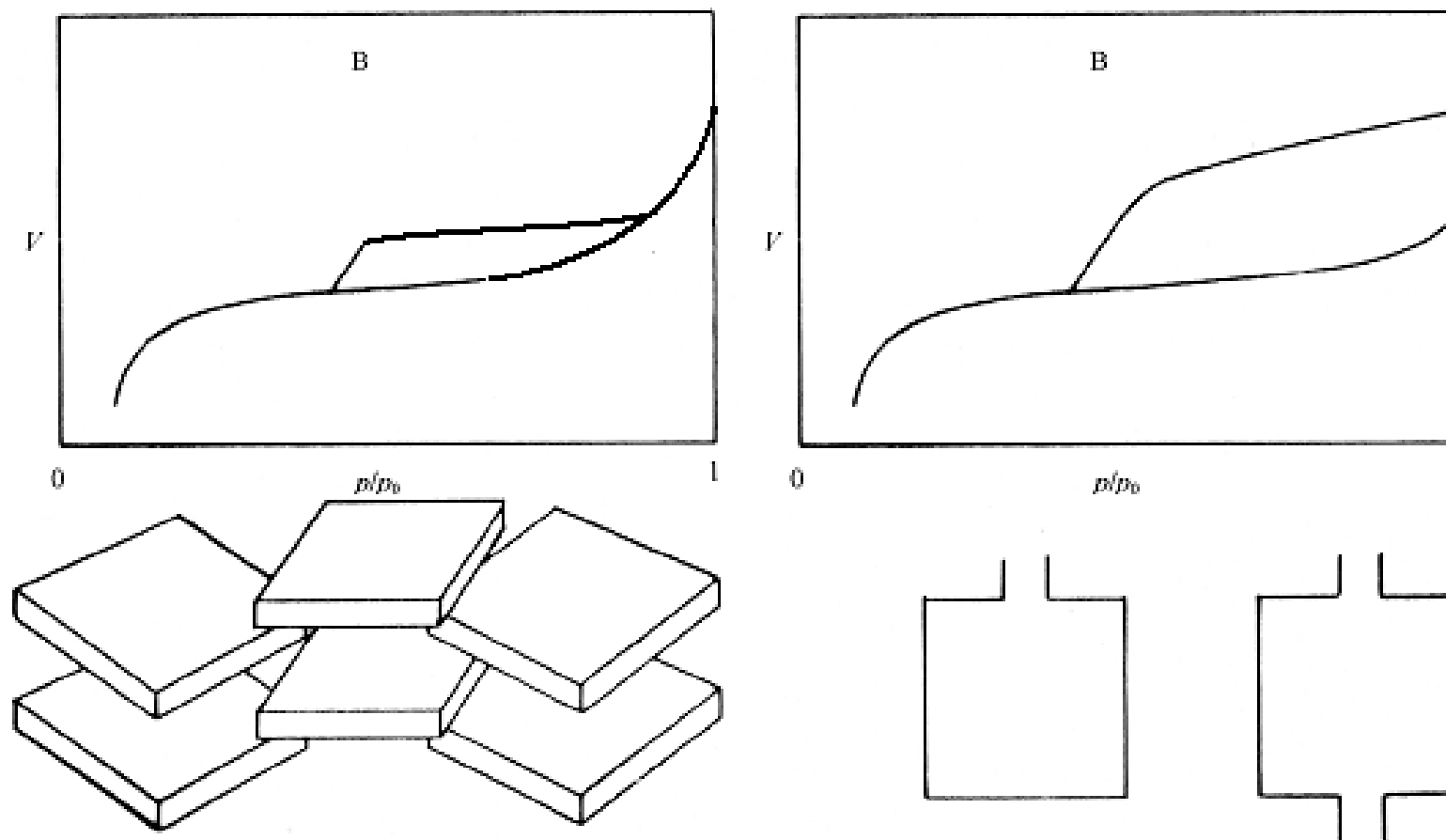
Figure 4.12 Type B hysteresis loop and possible pore structures.

Pores between laminated plates

Small neck, large body (~100nm) Pores

60

V_a (cm^3 at STP)

Desorption

Adsorption

(reversible)

.1   .2   .3   .4   .5   .6   .7   .8   .9   1.0

P/P_0
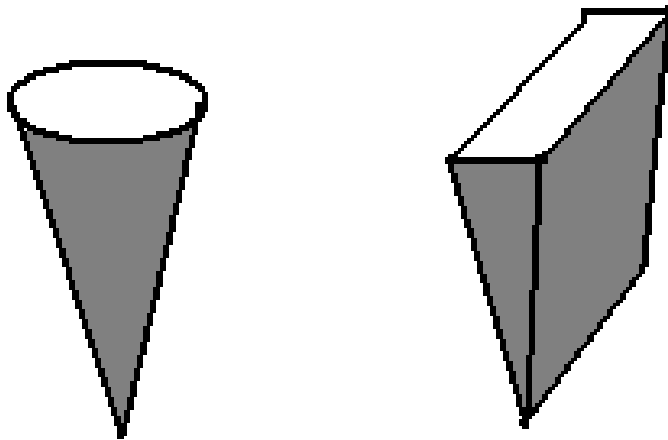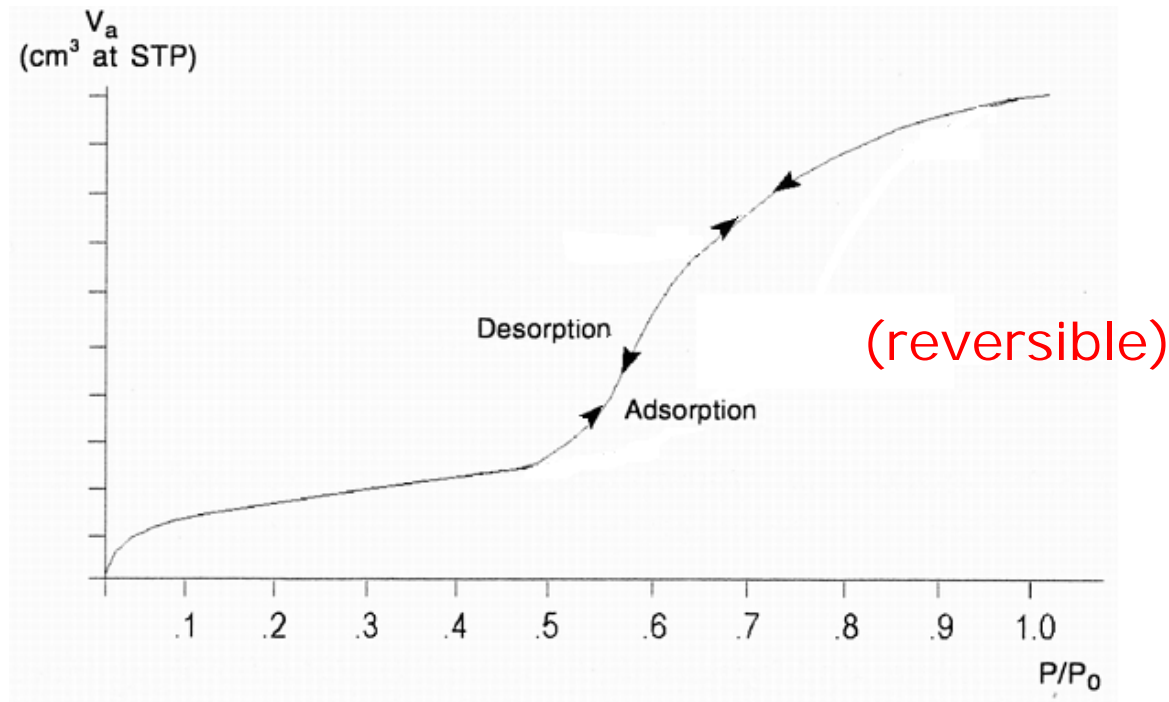
Capillary condensation occurs conical, wedge-pore close at one end

61

BET (Brunauer-Emmett-Teller) Surface Area Measurement

Physical Adsorption of Gas Adsorbate
BET equation:

$$\frac{P}{V_a(P_0 - P)} = \frac{1}{V_m C} + \frac{C-1}{V_m C}\left(\frac{P}{P_0}\right)$$

(3-1)
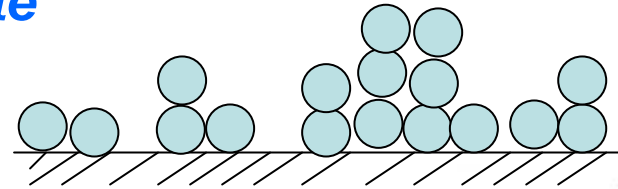
$$C \propto \exp\frac{q_1 - q_L}{RT}$$

(3-2)

q_1 = heat of adsorption of the first layer
q_L = heat of liquefication of the gas adsorbat
V_m = amount of gas adsorbed upon monolayer coverage

$$s = \frac{V_m \sigma N_A}{m V_o}$$

(3-3)

s = surface area
σ = mean area per molecule of the gas adsorbate

$$s(m^2 / g) = \frac{4.35\, V_m\,(cm^3\ at\ STP)}{m(g)}$$

N_2 as the adsorbate   (3-4)

Effective BET plot is usually in the range of

$P/P_0 = 0.05 \sim 0.3$
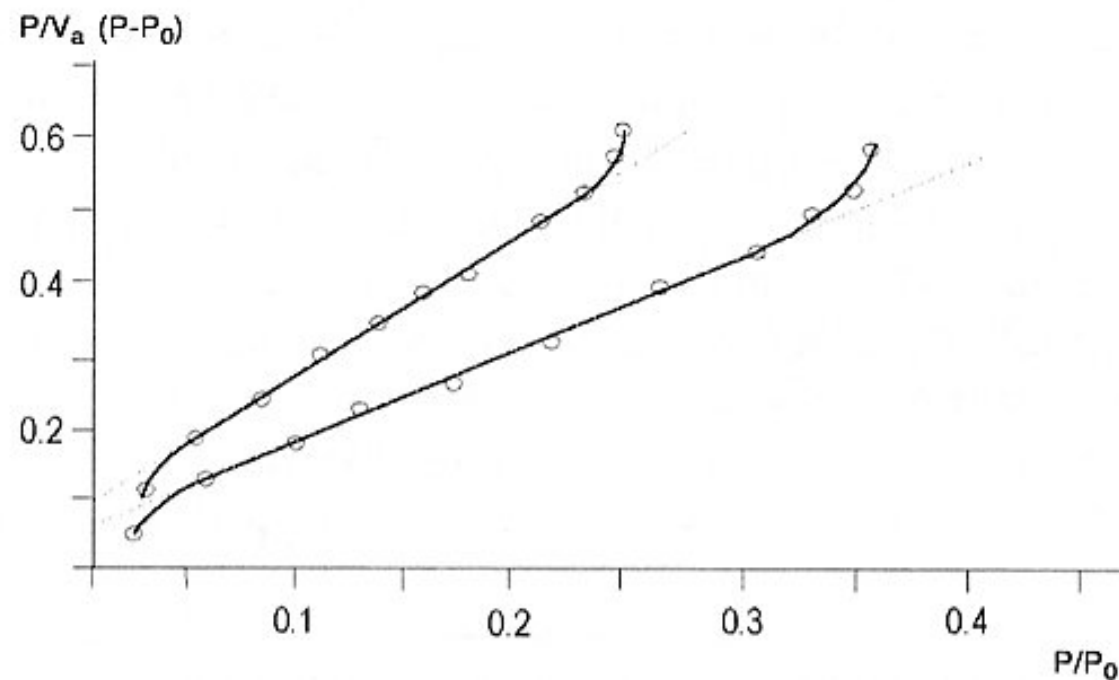
Figure 3.7. BET transform plots, each with a regression line through the linear region.

Porous Structure Determination

α - Plot

Table 3.1. Data set from adsorption on reference material. Shaded area contains interpolated values.

	Reference Data	
P/P_0	V_a	α_S
0.0101	0.9613	0.45
0.0502	1.2742	0.60
0.1501	1.5902	0.75
0.2003	1.7072	0.81
0.4000	2.1156	1.00
0.4003	2.1188	1.00
0.5002	2.3421	1.11
0.7002	2.9570	1.40
0.7999	3.4895	1.65
0.8750	4.2270	2.00
0.8999	4.6219	2.19
0.9483	6.0848	2.90
0.9660	7.2637	3.43
0.9754	8.3359	3.94
0.9842	10.0120	4.73
0.9901	11.8578	5.61
0.9967	16.5133	7.81

$$\alpha = V_a / V_a(P/P_0 = 0.4000)$$
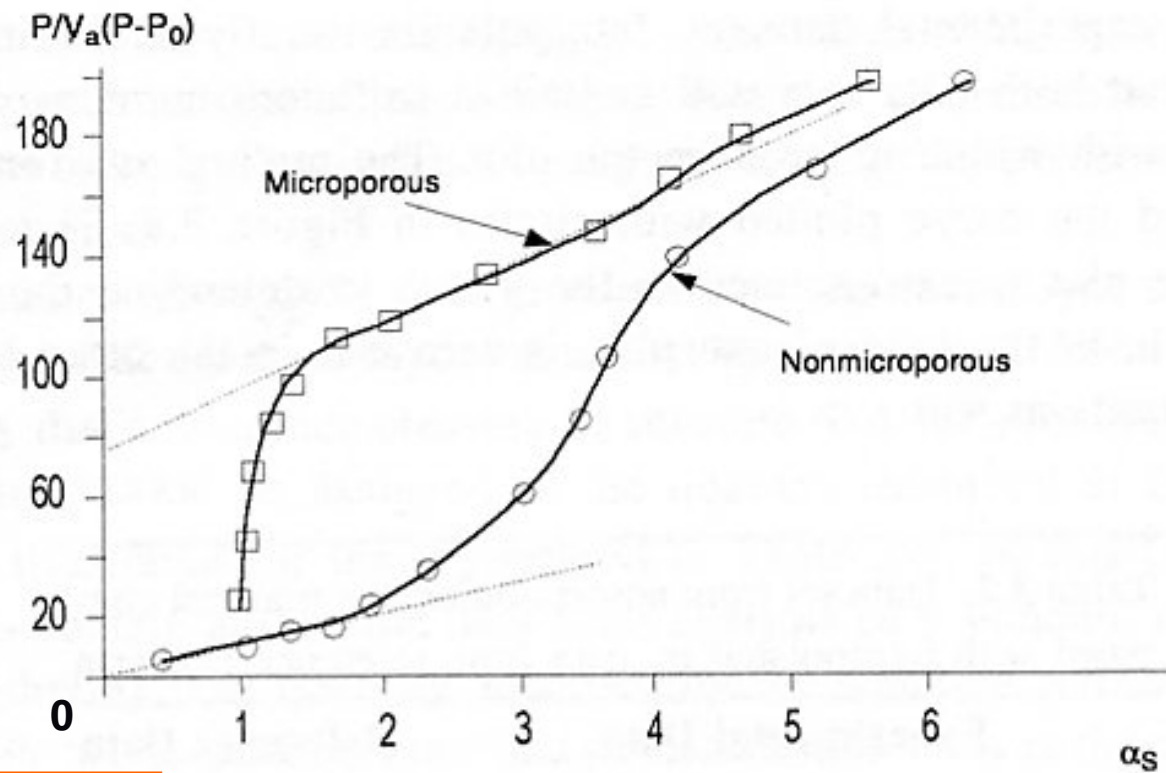
Figure 3.8. α_S plots of experimental data showing first linear region extrapolated to the y-axis.

t - Plot

$$t = 3.54 \left(\frac{V_a}{V_m} \right) \ \overset{\circ}{A}$$
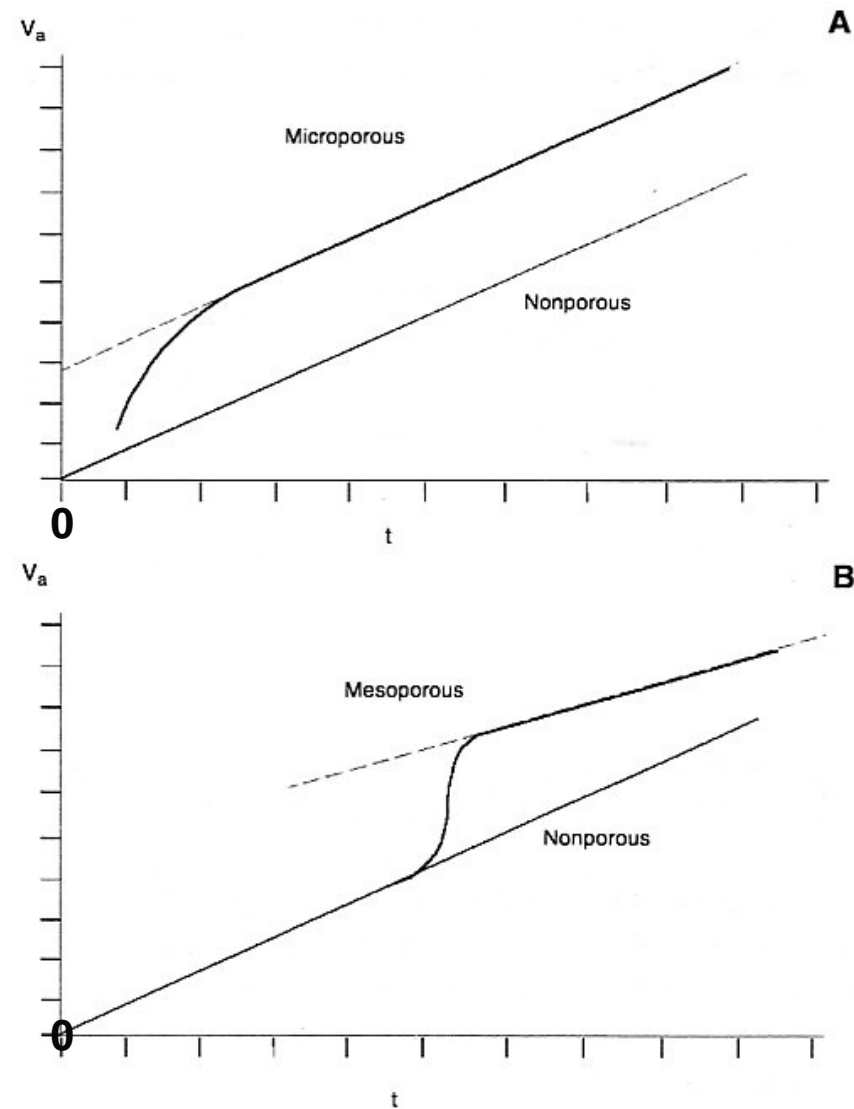
Figure 3.9. Idealized examples of t-Plots for (A) a microporous and (B) a mesoporous solid. Both examples show also the t-plot obtained for a nonporous sample of the same type as the porous sample.

BJH Pore Size Distribution

Kelvin Equation

$$\ln(P^*/P_0) = -(2\,\gamma\,\nu)/RTr_m$$

P^* = the critical condensation pressure
γ = the liquid surface tension
ν = molar volume of the condensed adsorbate
θ = contact angle
r_m = mean radius of the curvature of the liquid meniscus

$$r = r_k + t = r_m \cos\theta + t$$

r = pore radius
t = thickness of adsorbate on the wall

$$r_m = (r - t)/\cos\theta$$

$$\ln(P/P_0) = -(2\,\gamma\,\nu\cos\theta)/RT(r - t)$$

t $r = r_k + t$

r_m

θ
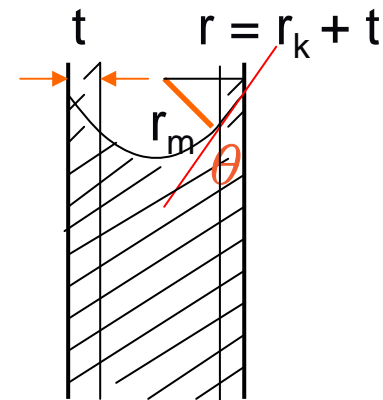
cylindrical pore

On desorption, $\theta \sim 0$, $\cos \theta \sim 1$

$$\ln(P/P_0) = - (2\,\gamma\,\nu\,\cos\theta)/\, RT(r - t)$$

$$r = - (2\,\gamma\,\nu)/\, RT\,\ln(P/P_0) + t$$

$$r_P = -\frac{0.405}{\log\left(\dfrac{P}{P_0}\right)} + t$$
(nm)

for liquid N_2 at 77.4 K

$\gamma = 8.72 \times 10^{-3}$ Nm^{-1}, $\nu = 34.68$ cm^{3}· mol^{-1}

V_a (cm^3 at STP)

Desorption

Adsorption

.1 .2 .3 .4 .5 .6 .7 .8 .9 1.0

P/P_0

Figure 3.3. Adsorption and desorption isotherms for a porous solid.

68
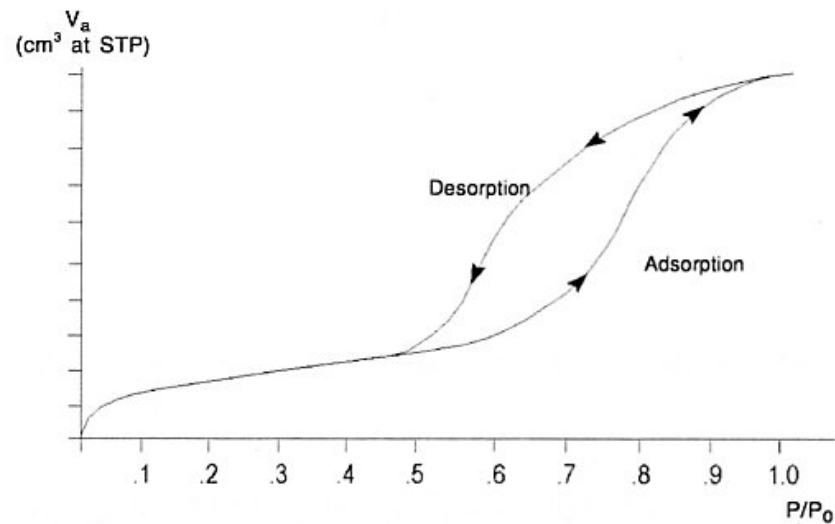
P (torr)	P/P_0	r_k (nm)	
760	1.00	10^4	⟸ *complete condensation*
752	0.990	10^2	
691	0.909	10	
292	0.384	1	
112	0.147	0.5	
0.05	6.9×10^{-5}	0.1	⟸ *undetectable*

⟹ **N_2 adsorption-desorption method applicable to**

1 nm < r < 20 nm
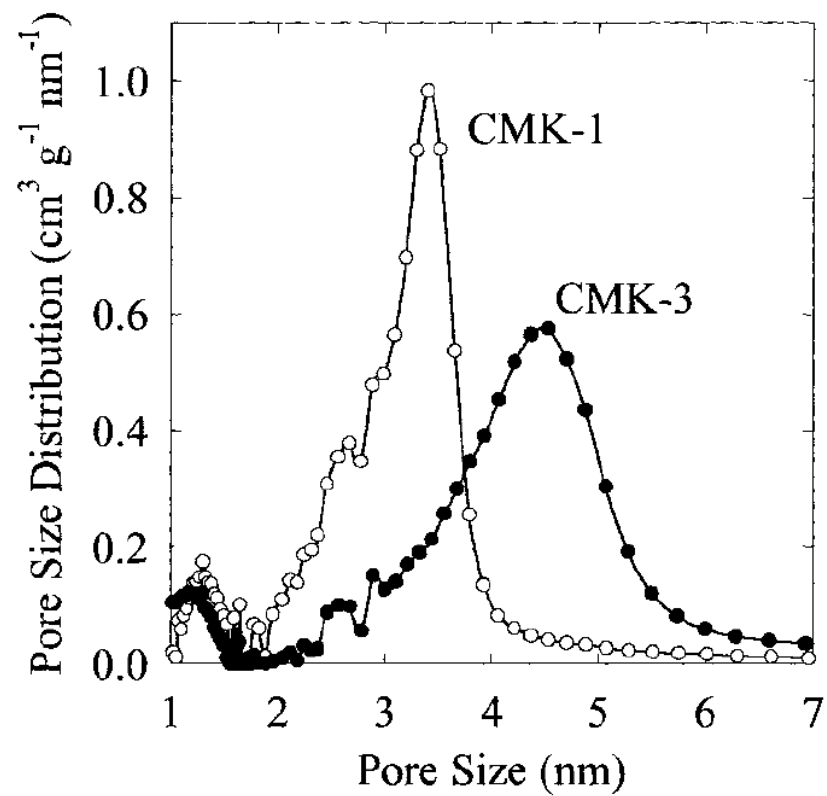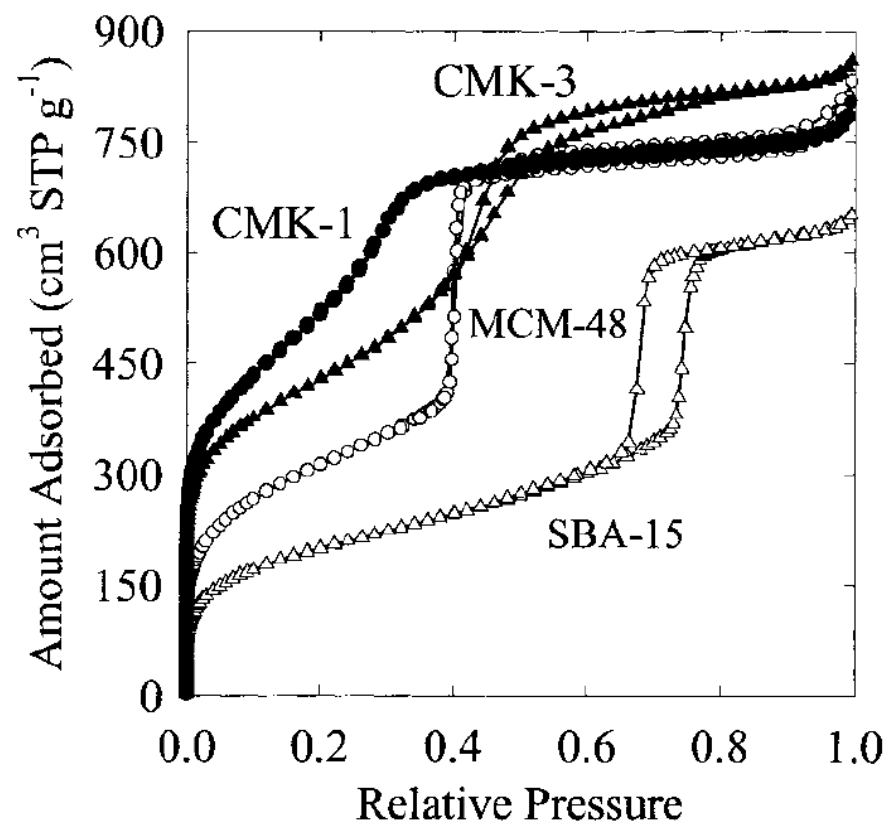
Ryoung Ryoo *et al.*, *Adv. Mater.* 13(9), 677(2001)

Mercury Intrusion Porosimetry (MIP)

Resistance force due to surface tension = Force due to applied pressure

$$-\pi \, D\gamma \, \cos\theta = \frac{\pi \, D^2 \, P}{4}$$

P = applied pressure
D = pore diameter
γ = surface tension of Hg
θ = contact angle

$$D = \frac{-4\gamma \, \cos\theta}{P}$$ **(Washburn equation)**
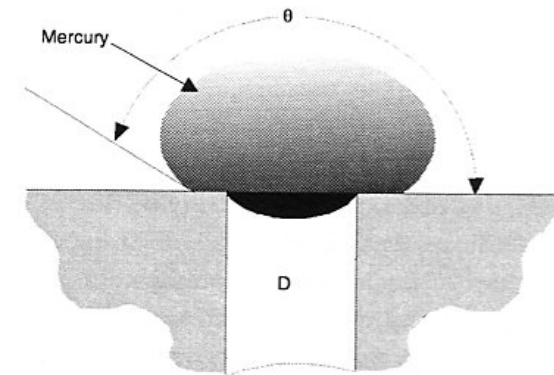
Figure 4.1. Mercury in contact with a porous solid.

For slit-like pores

$$W = \frac{-2\gamma \, \cos\theta}{P}$$

W = width between the plates

$$r \sim \frac{7500}{P}$$

(nm)   (atm)

P ↑ ⇒ r ↓

71
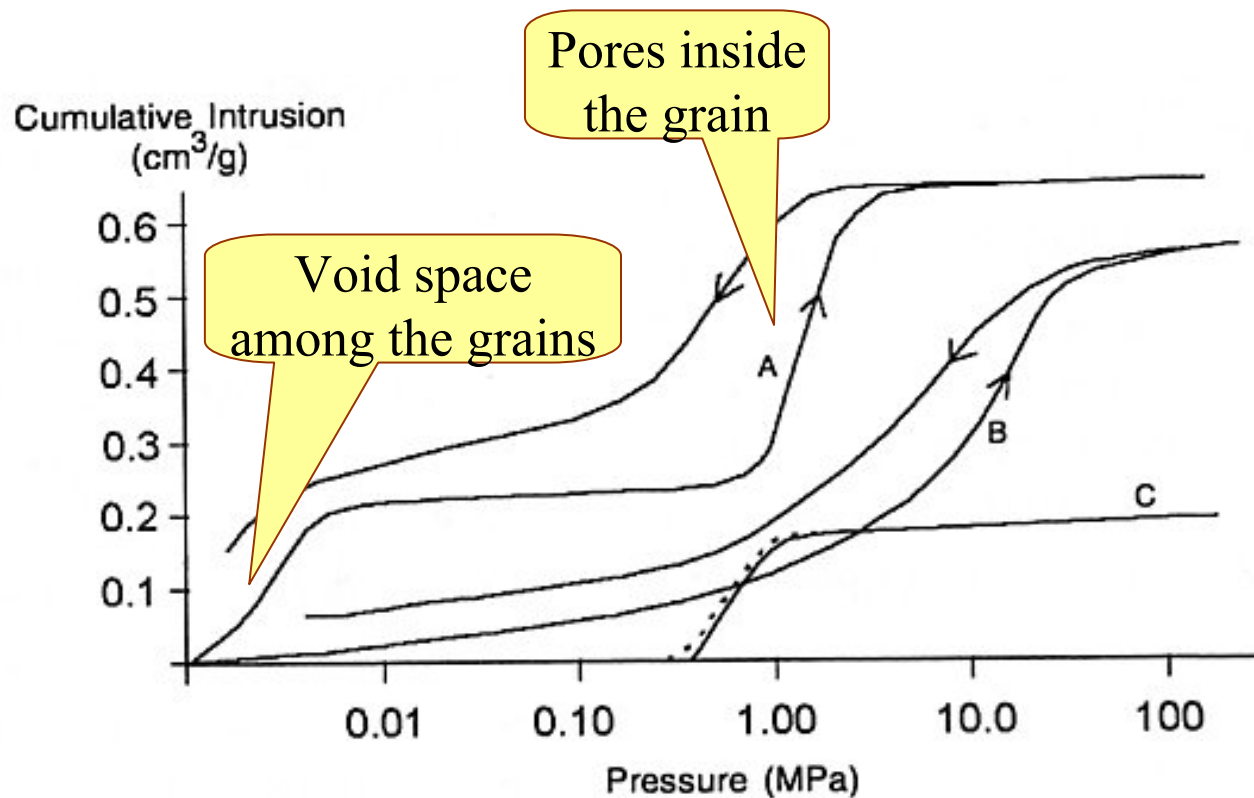
Figure 4.2. Typical intrusion and extrusion curves from a mercury penetration analysis.

A: sample of relatively coarse grains
B: a single piece of material with a wide distribution of
  pore sizes
C: fine powders without pores

72

Techniques for characterization of nano-porous materials

Crystalline structure

- Single crystal & Powder X-ray diffraction (XRD)
- Electron crystallography

Surface area & Pore size

- N_2 adsorption-desorption isotherm
- Mercury Intrusion Porosimetry

Pore structure- TEM

Morphology- SEM

Oxidation state & Coordination

- X-ray absorption spectra
- X-ray photoelectron spectra (XPS & Auger)
- Solid state NMR (mainly coordination)
- IR & Raman (mainly coordination)
- UV-Vis spectra

Elemental analysis- ICP-AES, XPS, EDX
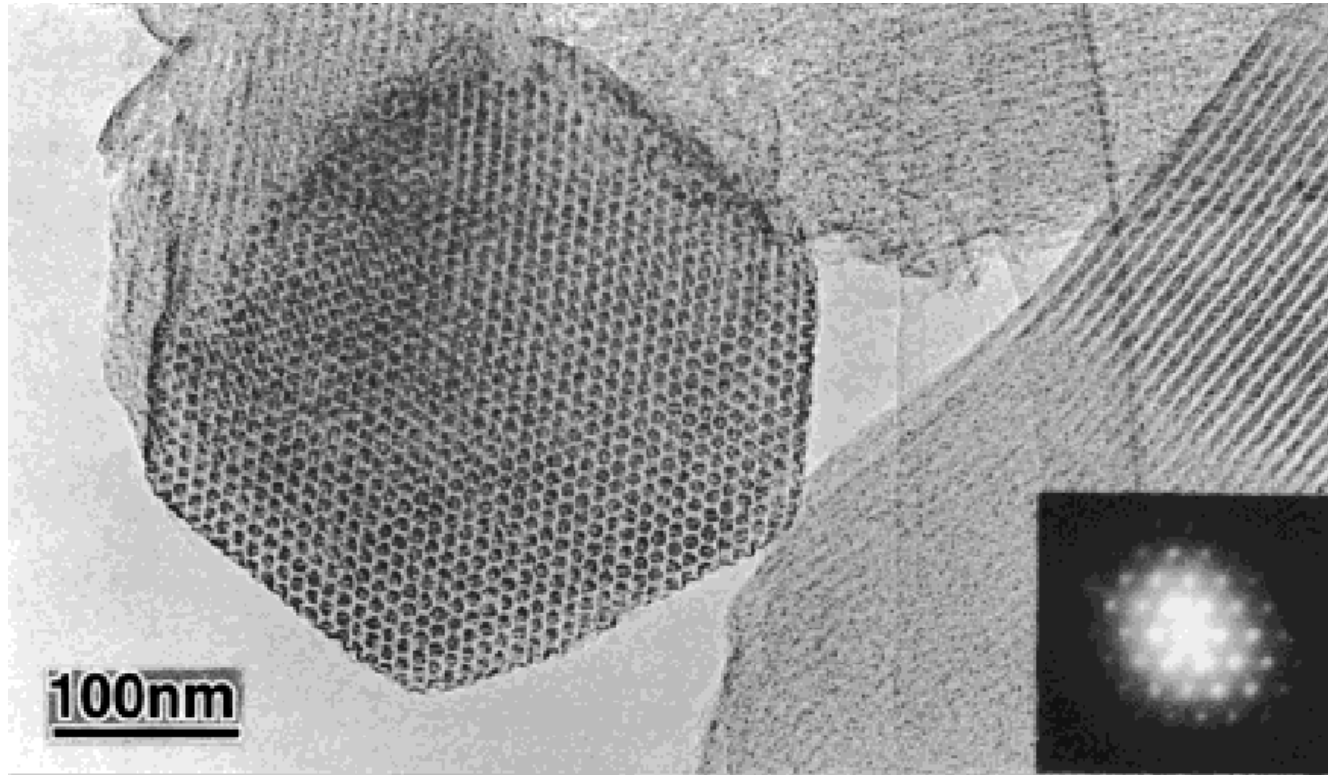
TEM photograph of Hexagonal Mesoporous Material

Synthesis of Zr-Incorporated SBA-15 Mesoporous Materials in a Self-generated Acidic Environment

Shih-Yuan Chen,[†] Ling-Yun Jang,[‡] and Soofin Cheng[*,†]
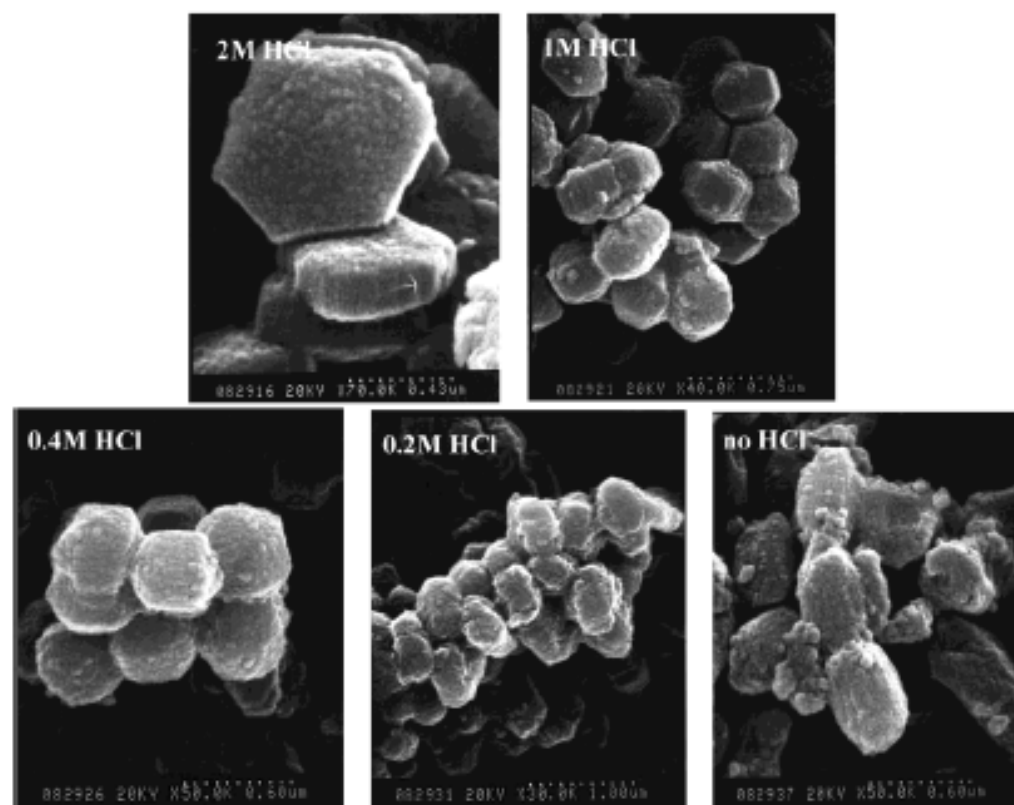
Figure 7. Morphologies of Zr−SBA-15 synthesized in solutions of different acidity; Zr/Si atomic ratio = 0.05, solvent = HCl.
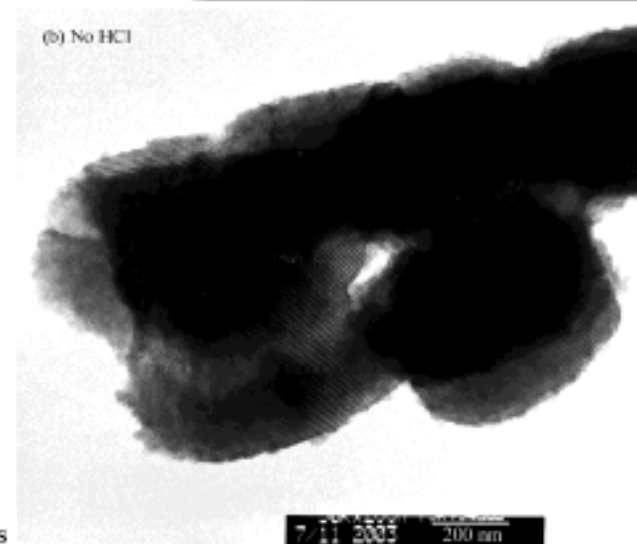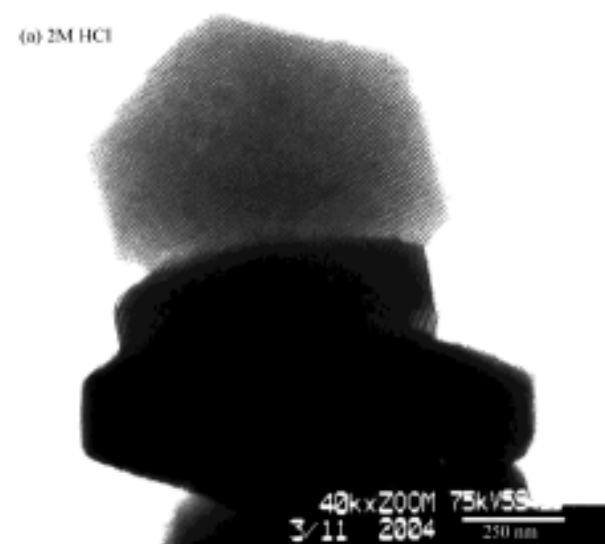
Figure 8. TEM images of Zr−SBA-15 samples

5

Synthesis and characterization of chiral mesoporous silica

Shunai Che[1], Zheng Liu[2,3], Tetsu Ohsuna[3], Kazutami Sakamoto[4],
Osamu Terasaki[3] & Takashi Tatsumi[5]
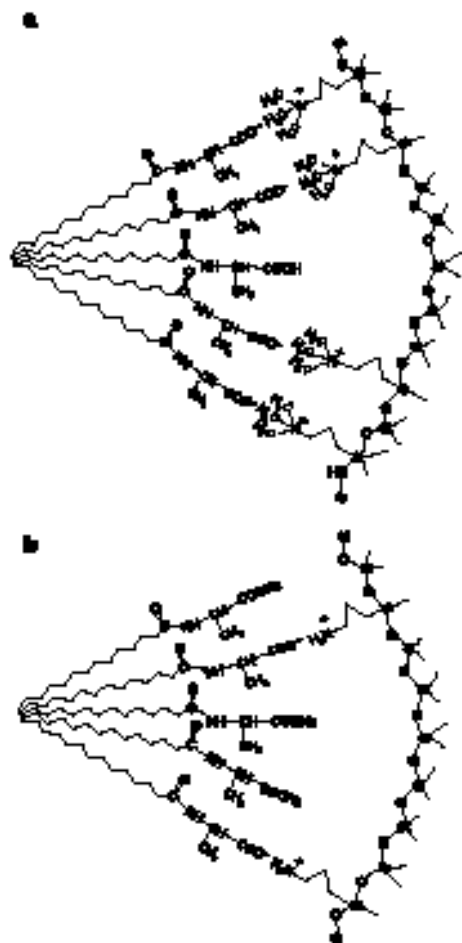
Figure 1 Schematic illustration of the two types of interaction between the head group of C$_{14}$-L-AlaS, its free amino acid C$_{14}$-L-AlaA and amino groups. The two types of interactions are achieved through double decomposition of negatively charged C$_{14}$-L-AlaS with positively charged quaternized aminosilane TMAPS (a), and neutralization of acid C$_{14}$-L-AlaA with primary aminosilane APS (b).
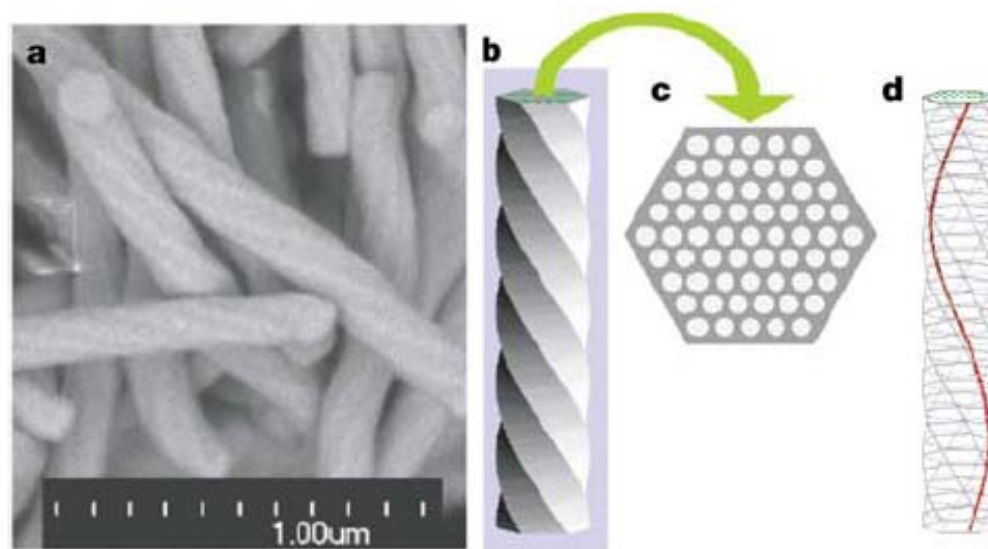
Figure 3 SEM image and schematic drawings of a structural model of chiral mesoporous silica. **a**, SEM image, showing the microscopic features of this sample (Hitachi S-5200 SEM). The samples were observed without any metal coating. **b**, Schematic drawing of a structural model of the chiral mesoporous material for TEM image simulation. **c**, Cross-section. **d**, One of the chiral channels in the material.
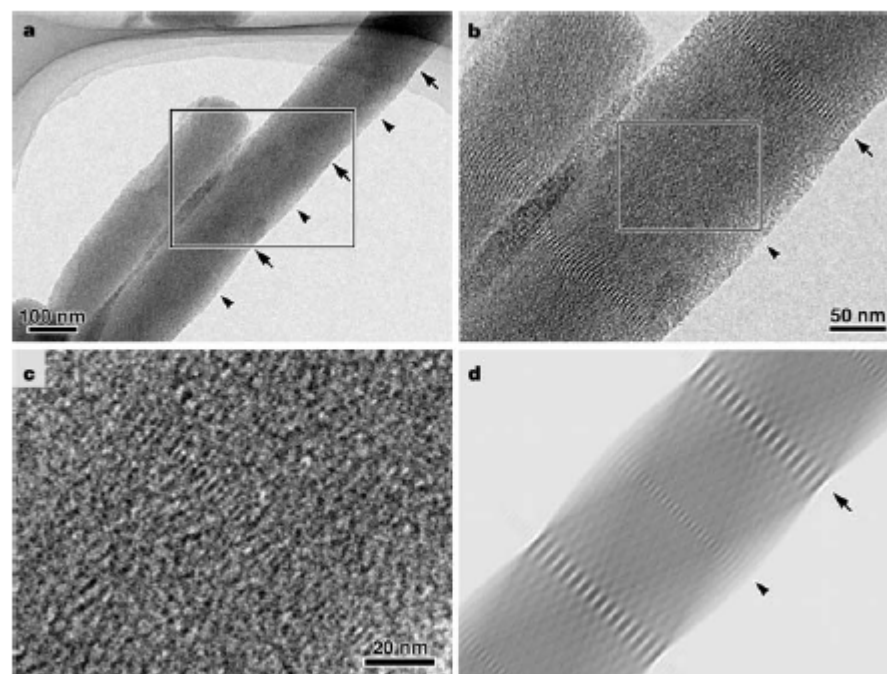
Figure 4 TEM images of chiral mesoporous silica. **a–c**, TEM images with different enlargements, showing two types of fringes (indicated by arrows and arrowheads) with different spacings. **d**, A simulated TEM image, showing good correspondence with the observed image. Owing to the limits on the calculation time, computer memory and image resolution, the rod diameter and the number of channels inside the rod are reduced from those observed. Images were obtained using a JEOL JEM-3010 TEM at 300 kV.
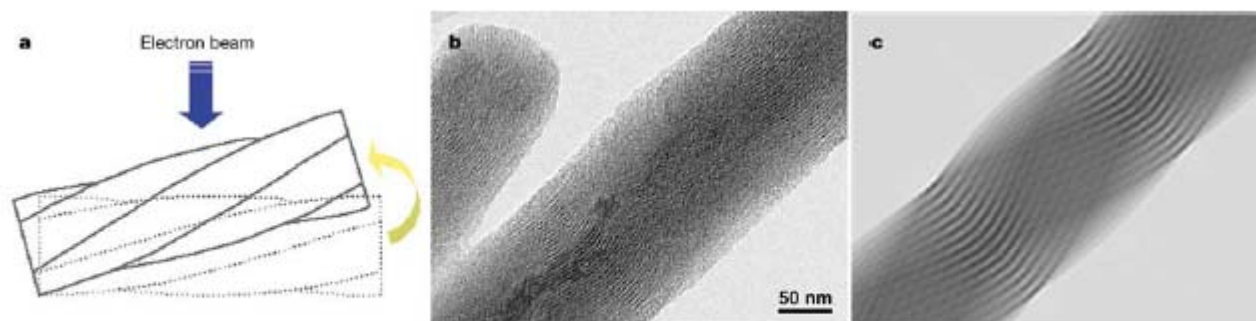
Figure 5 Schematic drawing of chiral mesoporous silica, its TEM image and the computer-simulated TEM image. The schematic drawing (**a**) shows the condition of the incident beam direction relative to the rod direction. The curvature of the (10) fringes can be observed in both the TEM image (**b**) and the simulated image (**c**). In this simulation, the angle between the incident beam direction and the perpendicular direction of the rod was 15°.

Techniques for characterization of nano-porous materials

Crystalline structure

- Single crystal & Powder X-ray diffraction (XRD)
- Electron crystallography

Surface area & Pore size

- N_2 adsorption-desorption isotherm
- Mercury Intrusion Porosimetry

Pore structure- TEM

Morphology- SEM

Oxidation state & Coordination

- X-ray absorption spectra
- X-ray photoelectron spectra (XPS & Auger)
- Solid state NMR (mainly coordination)
- IR & Raman (mainly coordination)
- UV-Vis spectra

Elemental analysis- ICP-AES, XPS, EDX

The Photoelectric Effect

- **Albert Einstein** considered electromagnetic energy to be bundled in to little packets called **photons**.

  Energy of photon = $E = h\nu$

  – Photons of light hit surface electrons and transfer their energy

  $h\nu =$ B.E. + K.E.

  $h\nu$

  $e^- (K.E.)$
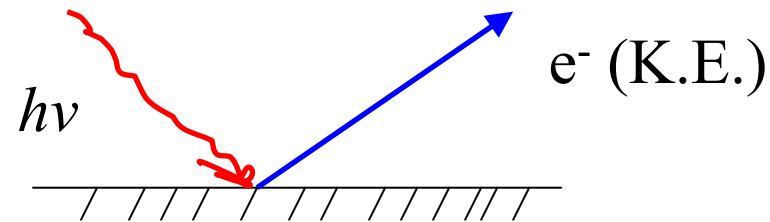
  – The energized electrons overcome their attraction and escape from the surface

- **Photoelectron spectroscopy** detects the kinetic energy of the electron escaped from the surface.

  – **XPS** – X-ray as the light source, core electrons escaped
  – **UPS** – UV as the light source, valence electrons escaped
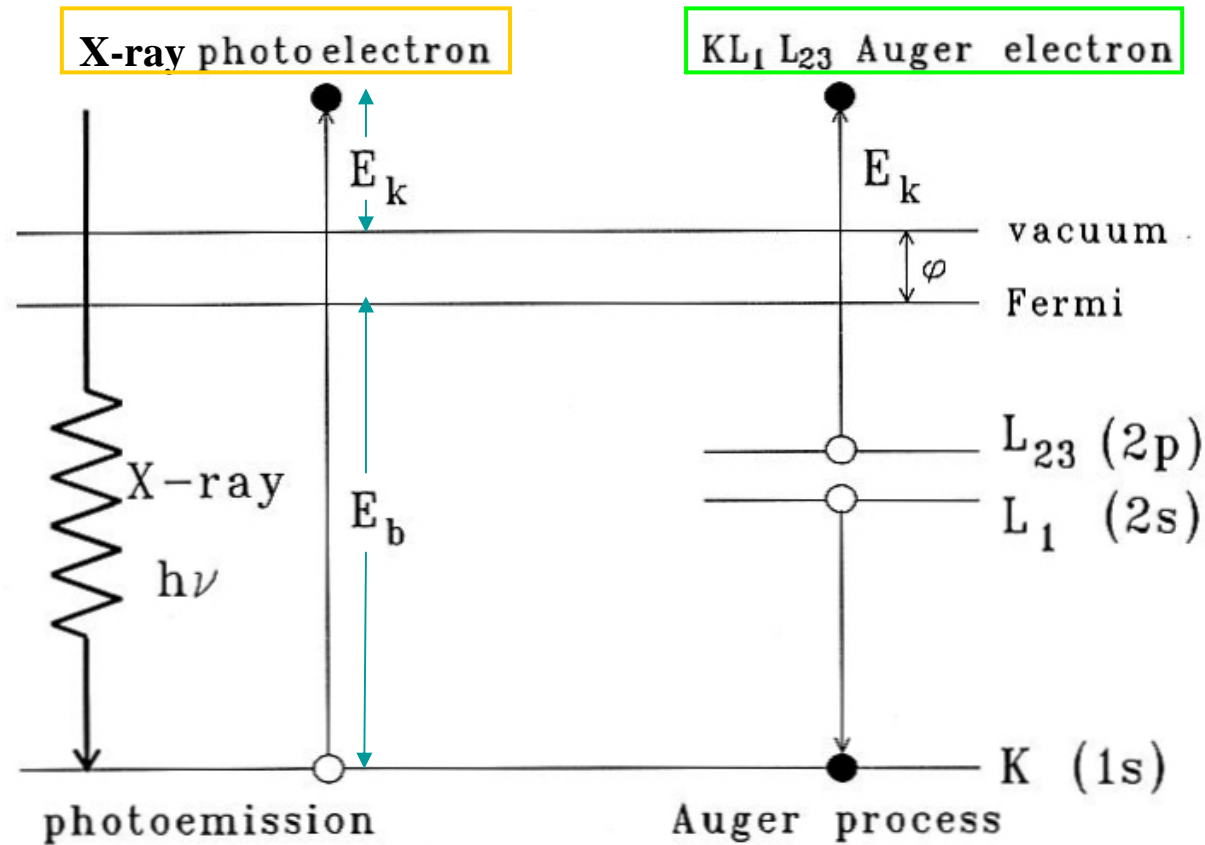
Figure 3.2: Photoemission and the Auger process. Left: An incident X-ray photon is absorbed and a photoelectron emitted. Measurement of its kinetic energy allows one to calculate the binding energy of the photoelectron. The atom stays behind as an unstable ion with a hole in one of the core levels. Right: The excited ion relaxes by filling the core hole with an electron from a higher shell. The energy released by this transition is taken up by another electron, the Auger electron, which leaves the sample with an elementspecific kinetic energy. In Auger spectroscopy the initial core holes are created by a beam of energetic (2-5 keV) electrons.

$$E_k = h\nu - E_b - \varphi$$

φ = work function

$$E_k(KL_1L_2) = [E_b(K) - E_b(L_1)] - E_b(L_2) - \varphi$$
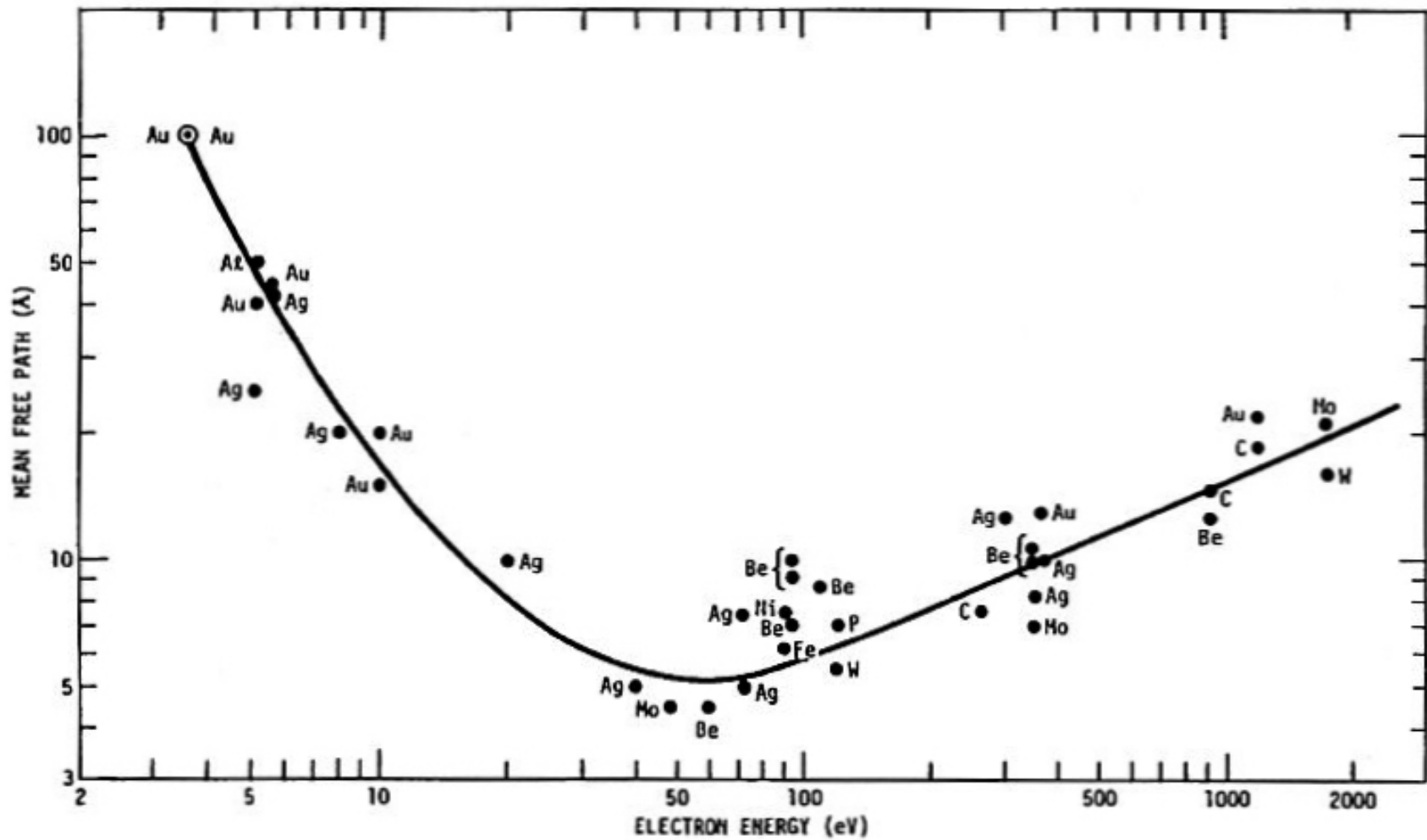
Figure 3.1: The mean free path of an electron depends on its kinetic energy and determines how much surface information it carries. Optimum surface sensitivity is obtained with electrons in the 25 - 200 eV range (from Somorjai, [16]).
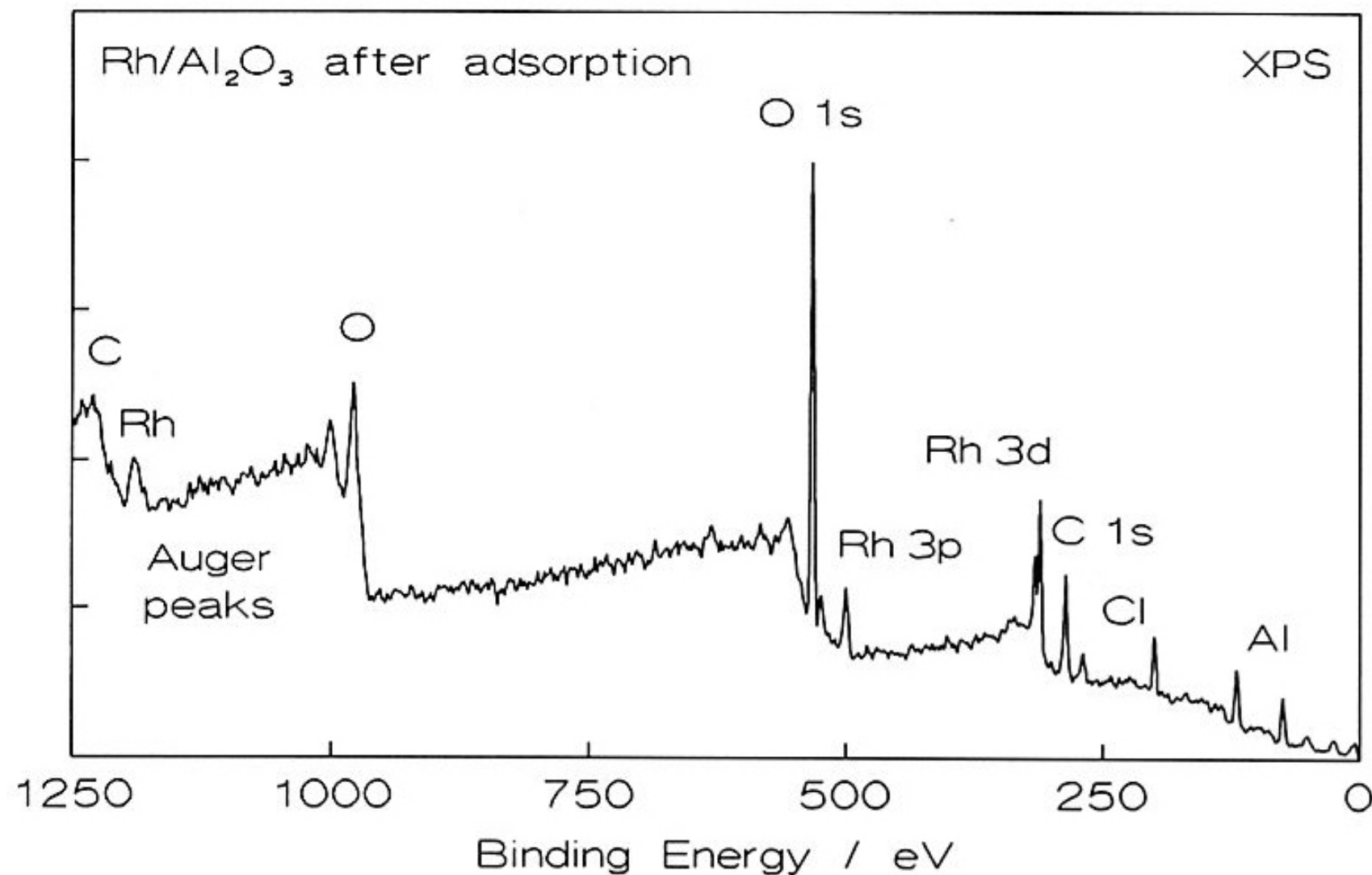
Figure 3.3: XPS spectrum of a Rh/Al$_2$O$_3$ model catalyst prepared by impregnating a thin film of Al$_2$O$_3$ on aluminum with a solution of RhCl$_3$ in water (courtesy of L.C.A. van den Oetelaar, Eindhoven).
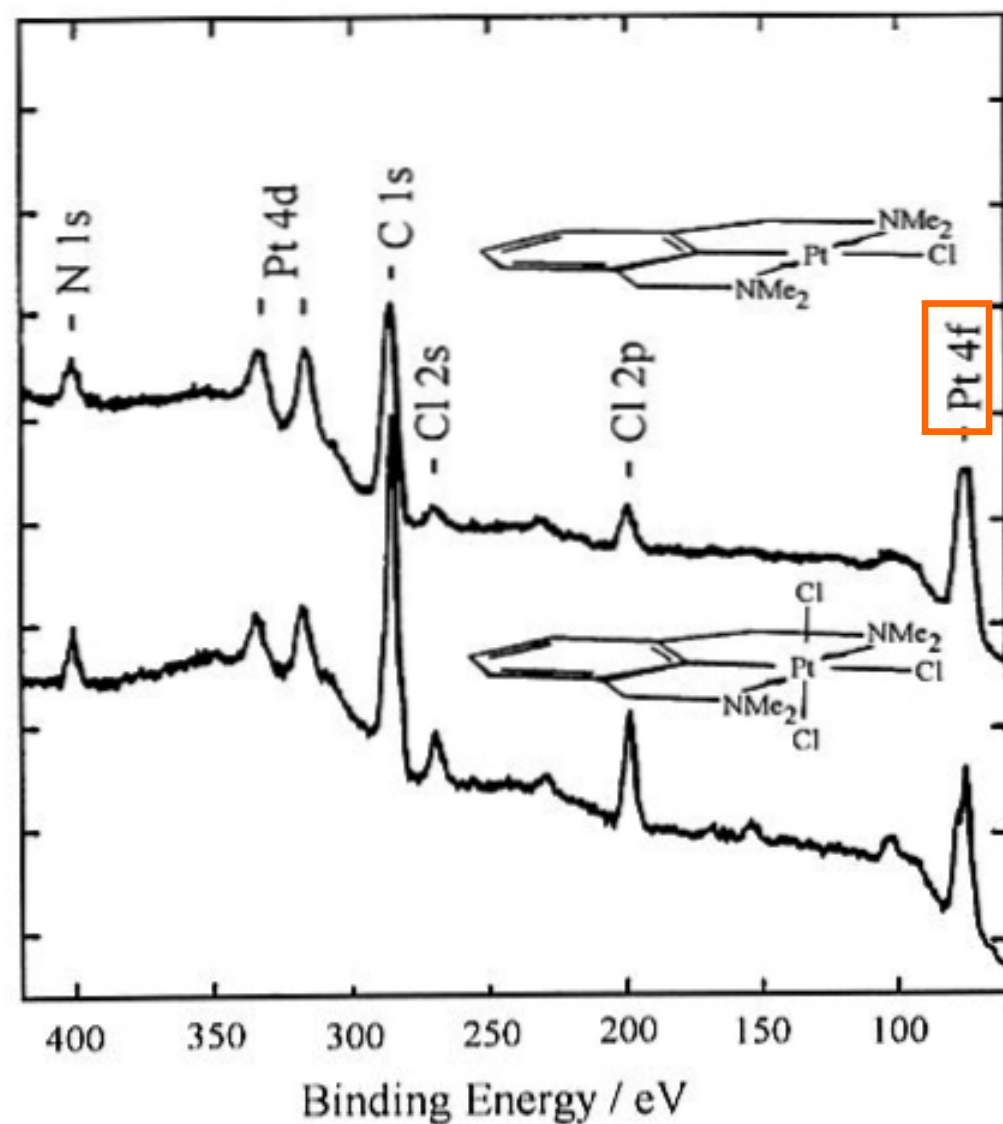
Figure 3.4: XPS scans between 0 and 450 eV of two organoplatinum complexes showing peaks due to Pt, Cl, N and C. The C 1s signal not only represents carbon in the compound but also contaminant hydrocarbon fragments, as on any sample. The abbreviation 'Me' in the structures stands for CH_3 (courtesy of J.C. Muijsers, Eindhoven).

83
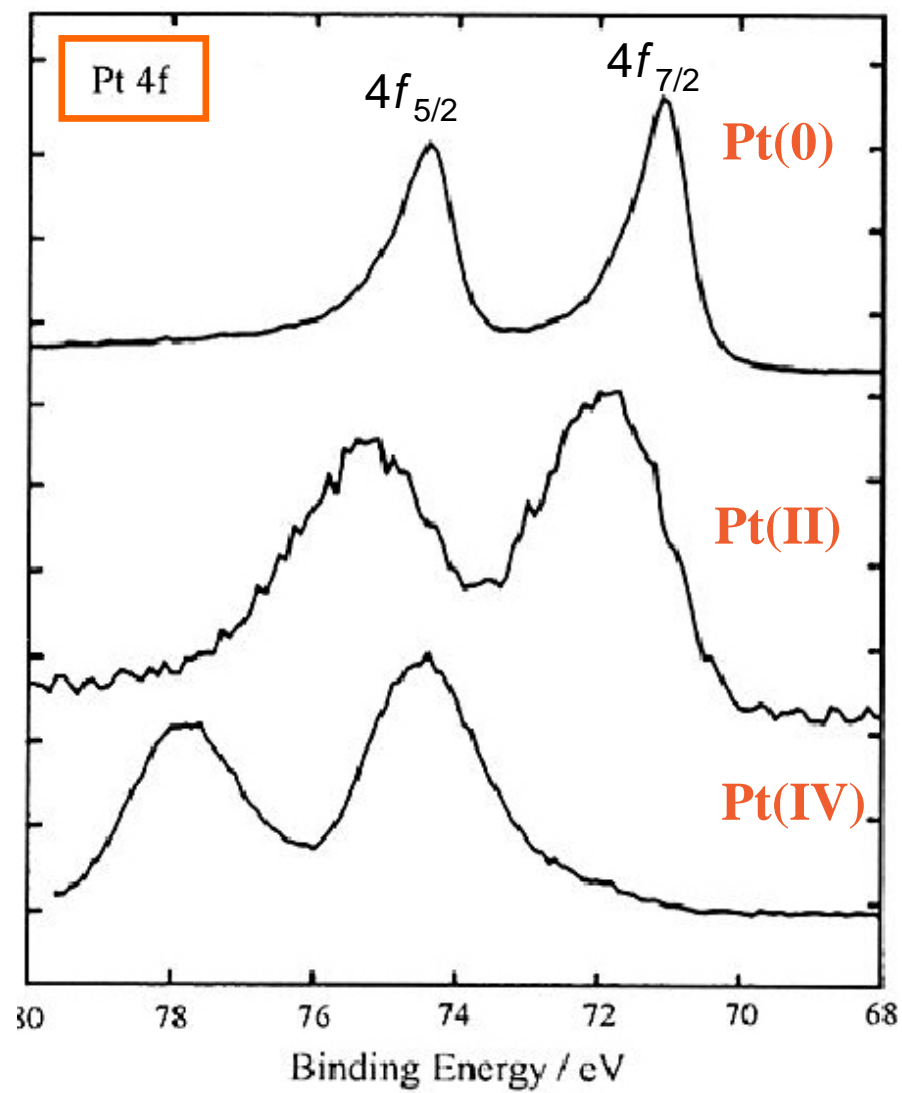
Figure 3.5: Pt 4f XPS spectra

84

TABLE II

Details of the Supported Metal Systems Studies Presented in Fig. 2

Curve (Fig. 2)	Metal and electron	BE^a for bulk (eV)	Support	Reference[b]
1	Pd $3d_{5/2}$	335.0	C	a
2	Pd $3d_{5/2}$	335.0	Y-Zeolite	b
3	Pd $3d_{5/2}$	335.0	SiO_2	c
4	Pt $4f_{7/2}$	71.5	Y-Zeolite	b
5	Pt $4d_{5/2}$	314.5	C	d
6	Pt $4d_{5/2}$	314.0	Al_2O_3	e
7	Pt $4f_{7/2}$	71.3	SiO_2	f
8	Pt $4d_{5/2}$	314.6	Al_2O_3	g

[a] BE = binding energy; ΔBE = BE(observed) − BE(bulk).

[b] References: (a) Takasu, Y., Akimaru, T., Kasahara, K., and Matsuda, Y., *J. Am. Chem. Soc.* **104,** 5249 (1982); (b) Védrine, J. C., Dufaux, M., Naccache, C., and Imelik, B., *J.C.S. Faraday I* **74,** 440 (1978); (c) Takasu, Y., Unwin, R., Tesche, B., Bradshaw, A. M., and Grunze, M., *Surf. Sci.* **77,** 219 (1978); (d) Mason, M. G., Gerenser, L. J., and Lee, S.-T., *Phys. Rev. Lett.* **39,** 288 (1977); (e) Huizinga, T., van't Blick, H. F. J., Vis, J. C., and Prins, R., *Surf. Sci.* **135,** 580 (1983); (f) Masson, A., Bellamy, B., Colomer, G., M'bedi, M., Rabette, P., and Che, M., *Proc. Int. Congr. Catal., 8th* **4,** 333 (1984); (g) Masson, A., Bellamy, B., Hadj Romdhane, Y., Che, M., Roulet, H., and Dufour, G., *Surf. Sci.* **173,** 479 (1986).
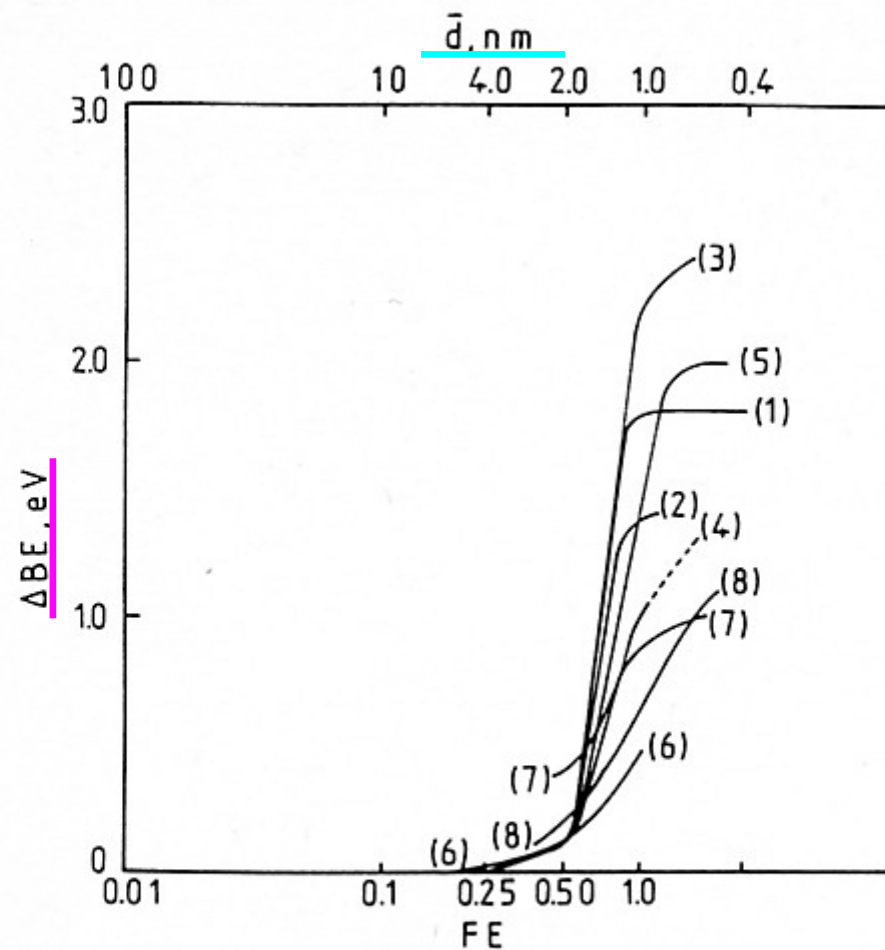
FIG. 2. Binding energy shifts ΔBE of metal core levels measured by photoelectron spectroscopy (XPS) versus fraction exposed FE and mean particle size $\bar{d}$ for various supported metal systems (see Table II for details of the studies).

Techniques for characterization of nano-porous materials

Crystalline structure

- Single crystal & Powder X-ray diffraction (XRD)
- Electron crystallography

Surface area & Pore size

- N_2 adsorption-desorption isotherm
- Mercury Intrusion Porosimetry

Pore structure- TEM

Morphology- SEM

Oxidation state & Coordination

- X-ray absorption spectra
- X-ray photoelectron spectra (XPS & Auger)
- Solid state NMR (mainly coordination)
- IR & Raman (mainly coordination)
- UV-Vis spectra

Elemental analysis- ICP-AES, XPS, EDX

X-ray Absorption Spectroscopy

x

$I(x, \omega)$ $I(0, \omega)$

Beer's Law: $I(x, \omega) = I(0, \omega)\, e^{-\mu(\omega)\, x}$

$-\mu_t x = \ln\left(I(x, \omega) / I(0, \omega)\right)$

XANES | EXAFS

Cu

constructive

Cu

destructive

Absorption

Energy (eV)
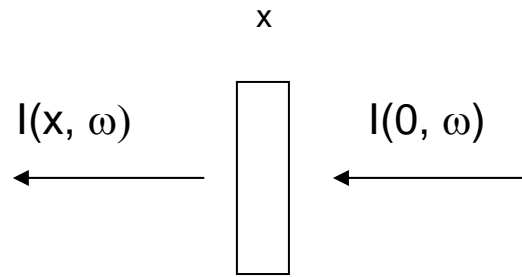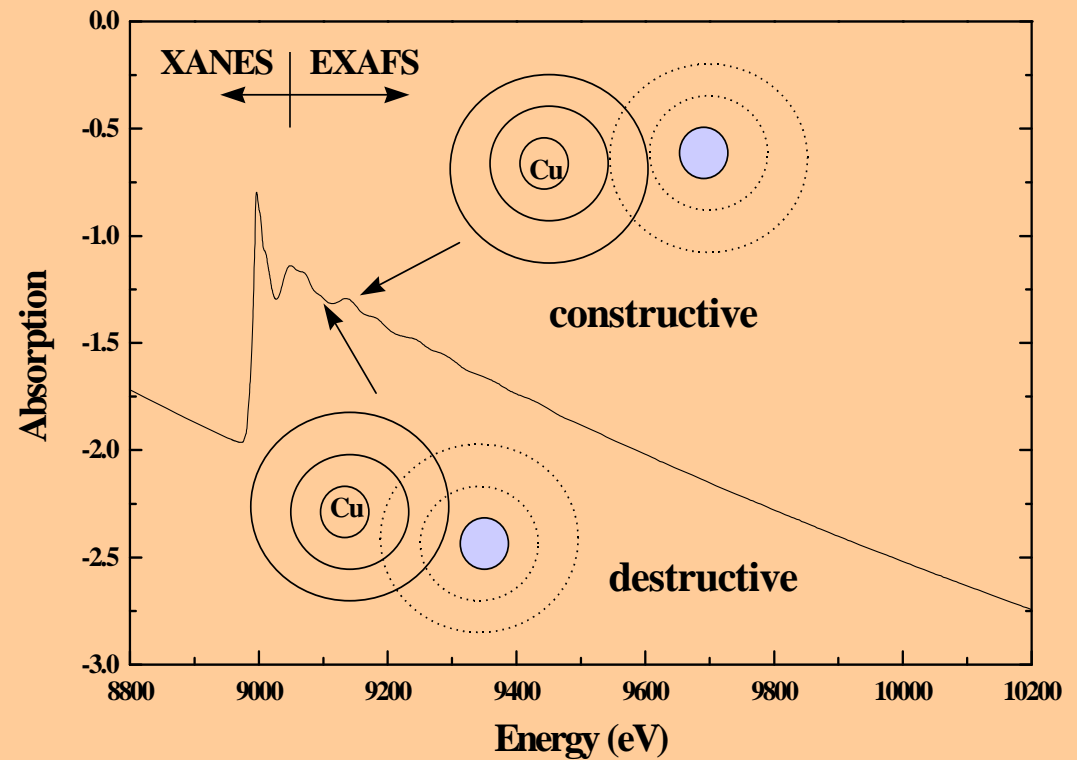
Advantage of X-ray Absorption Spectroscopy

- A powerful structural tool for materials in various forms, including crystalline or amorphous solids, liquids, and gases. Sample is not required to have structure of long-range order.

- XANES reflects effective charge density, electronic structure, and coordination symmetry of the absorber.

- EXAFS provides the information of local (< 10 Å) geometric structure.

- Element specific (element selective).

- Easy to perform in-situ measurements.
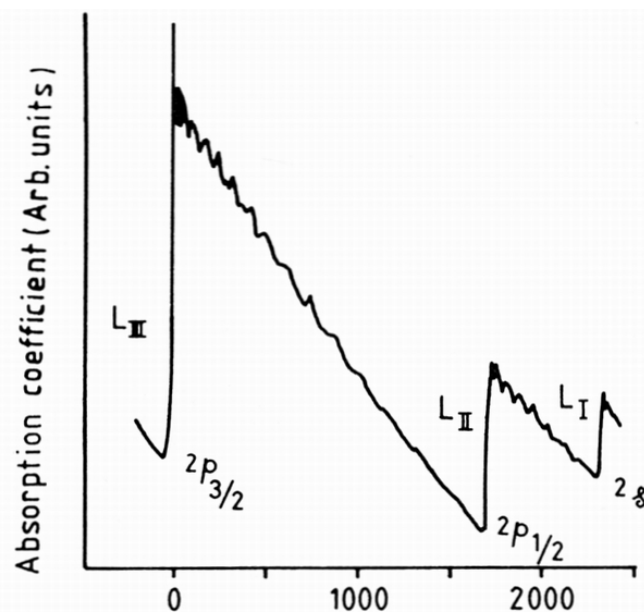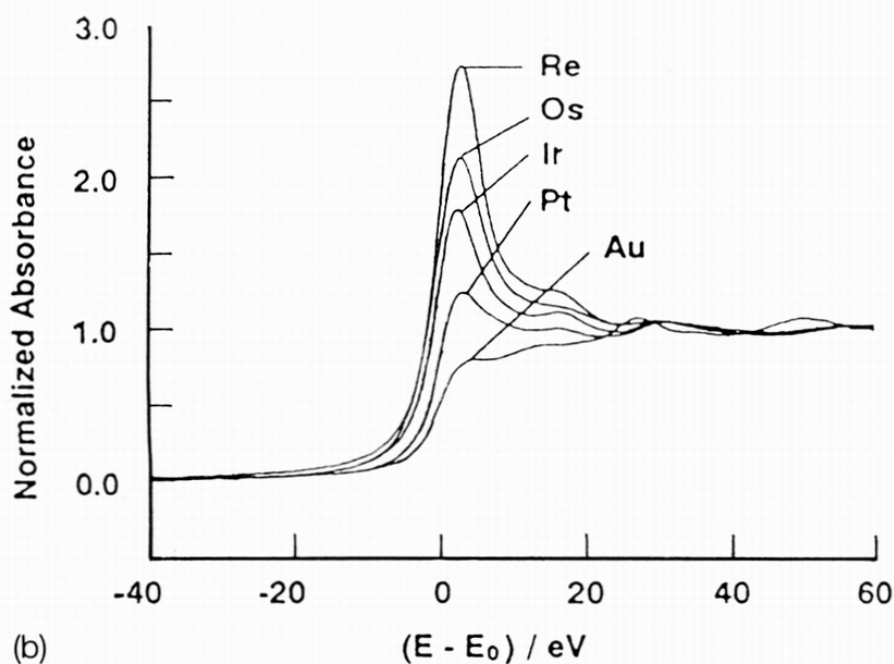
Figure 3.33 (a) Typical L-adsorption EXAFS spectrum of a thin foil of platinum. (b) X-ray spectra comparing the L_{III} absorption edges of the 5d metals (rhenium to gold). With permission from J. H. Sinfelt, G. Meitzner, *Acc. Chem. Res.* **1993**, *26*, 3.

90

Mn XANES AND OXIDATION STATE
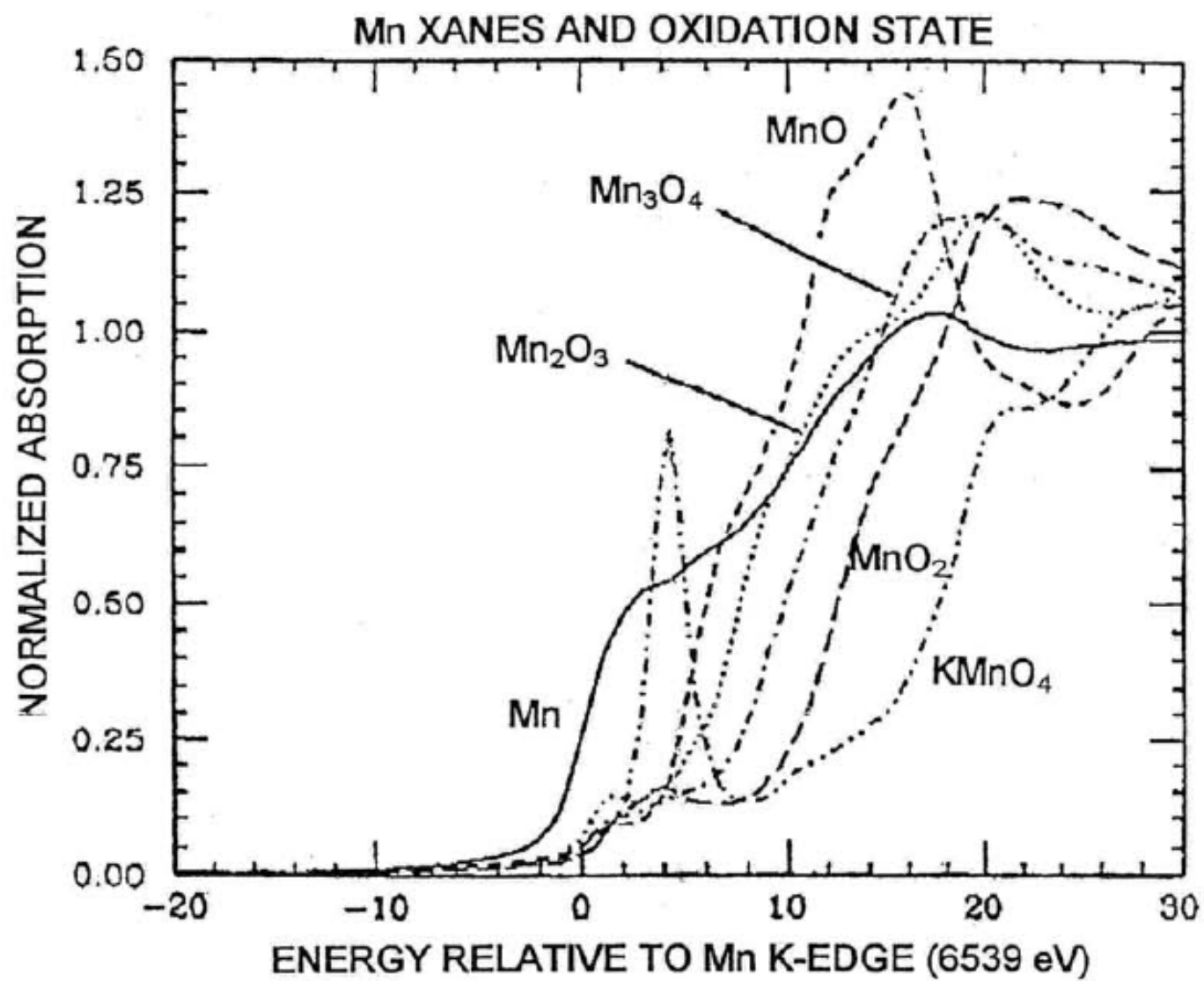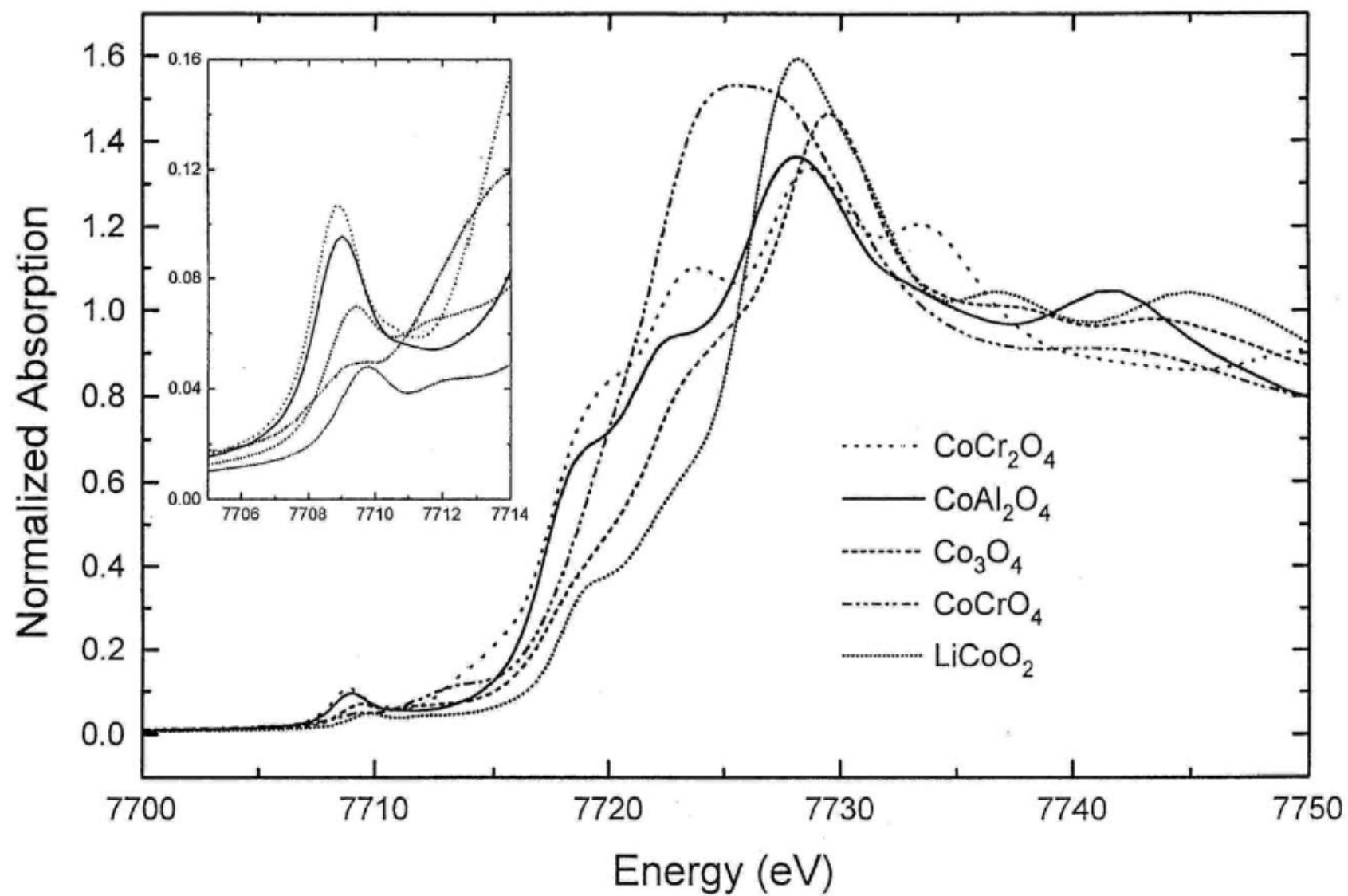
EXAFS: Extended X-ray Absorption Fine Structure

XANES: X-ray Absorption Near-Edge Structure

93
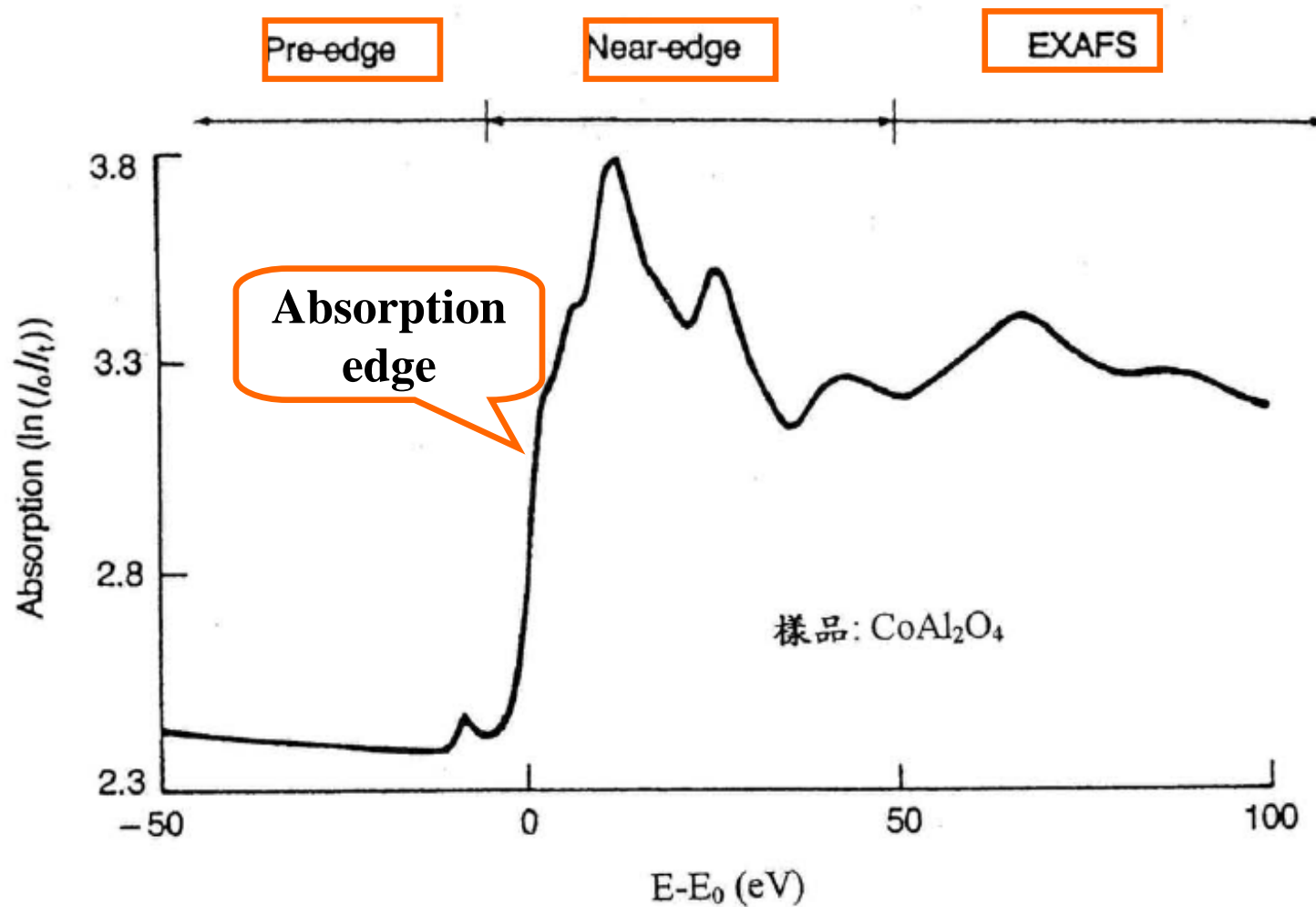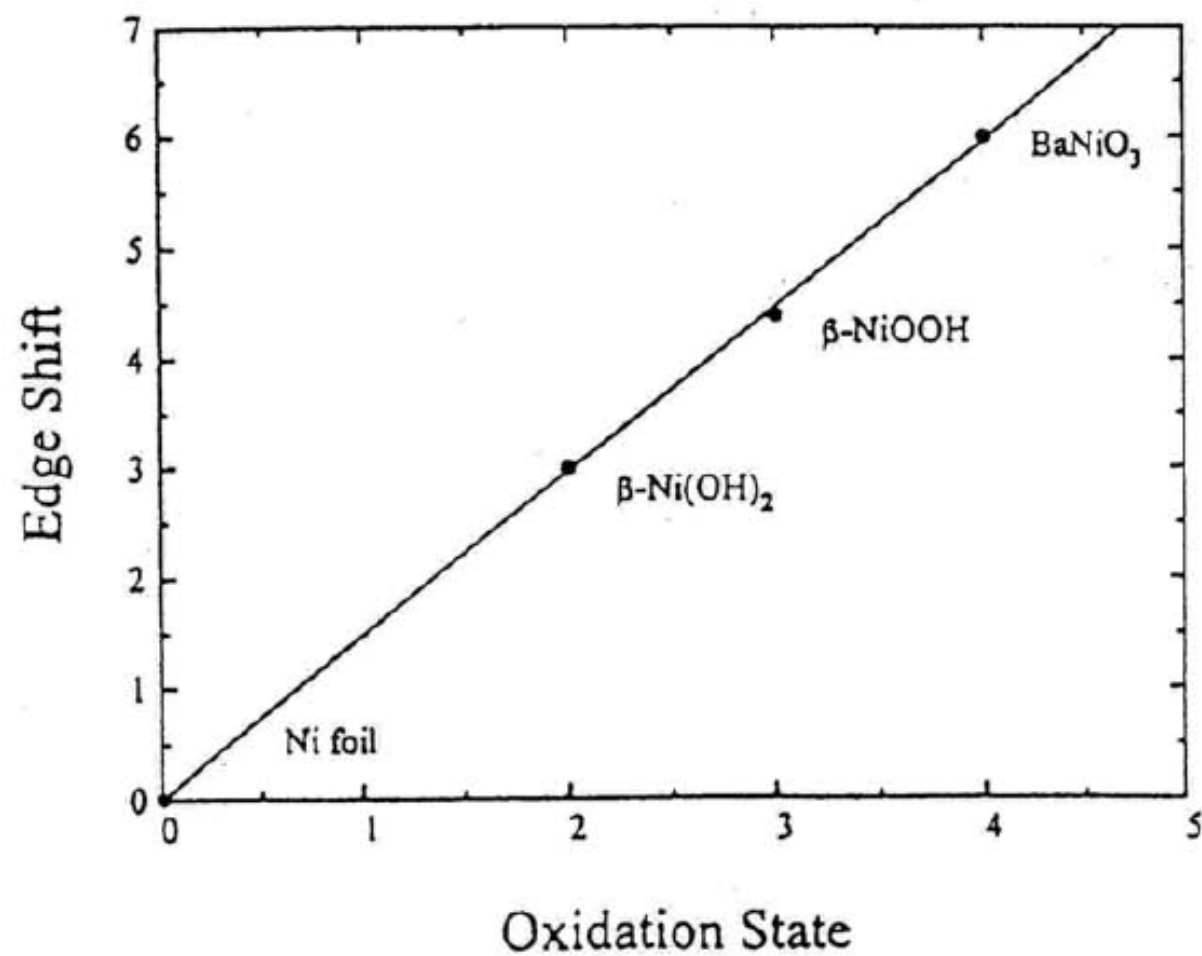
Fig. 3. Plot of the edge shifts in the XANES spectra vs. the increasing oxidation state of nickel.
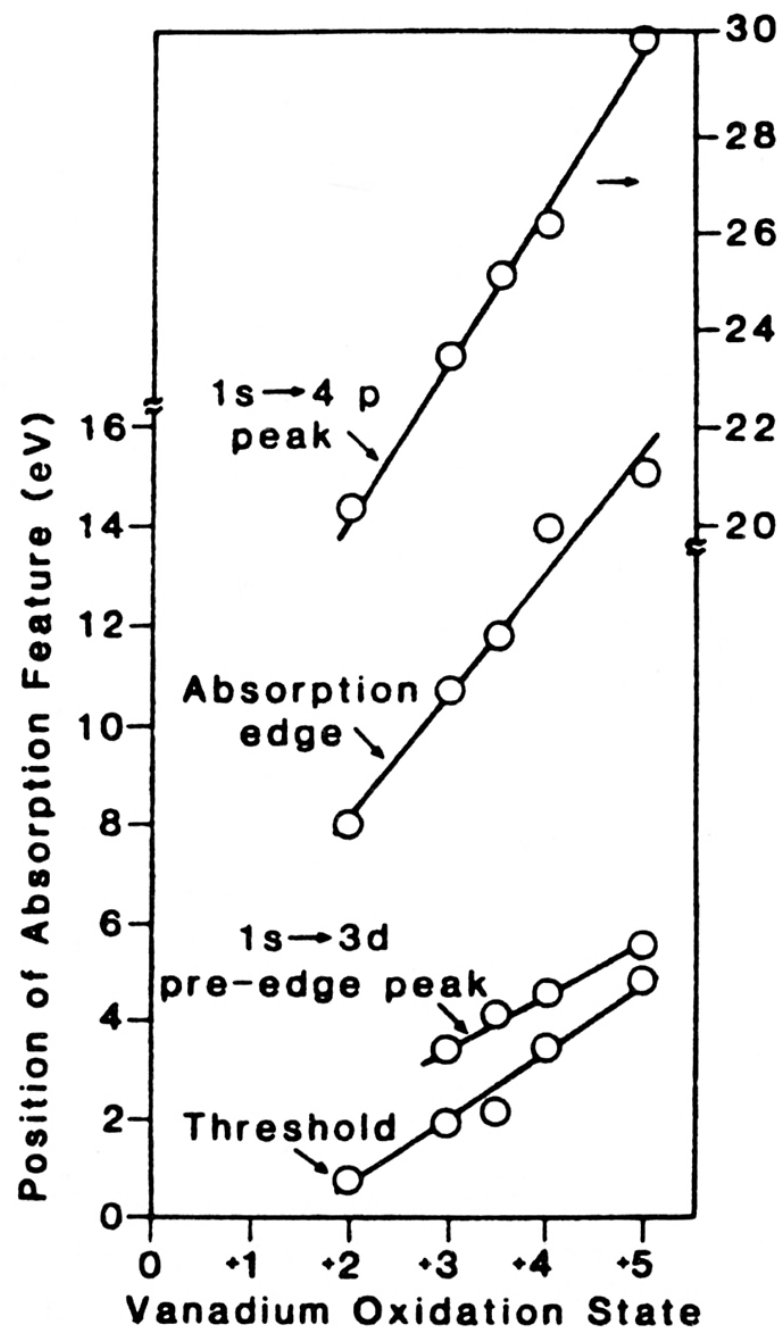
Figure 3.37 A strong correlation exists between the oxidation state of vanadium and the position of its absorption edge. (Courtesy J. Wong – see J. Wong, F. W. Lytle, R. P. Messmer, G. Maylott, *Phys. Rev. B* **1984**, *30*, 5596.)

95

MPTMS

S *K*-edge XANES spectra of (a) MPTMS, (b) dipropyl disulfide, (c) S16-SO3H (10%) 2M HCl, (d) S16-SO3H (20%) 0.5M HCl, (e) S16-SO3H (20%) 1.0M HCl, (f) S16-SO3H (20%) 2.0M HCl and (g) S16-SO3H (30%) 2.0M HCl

96
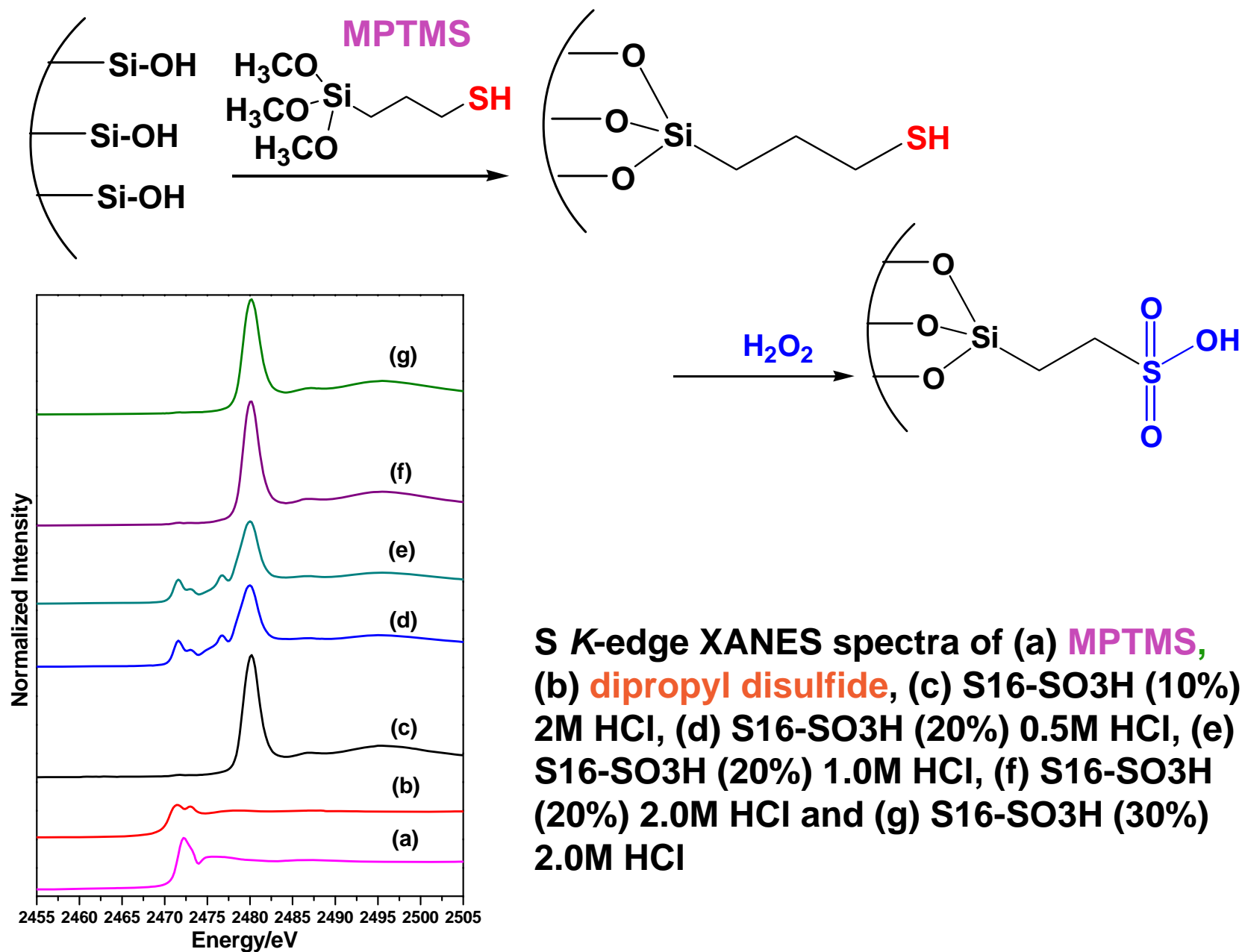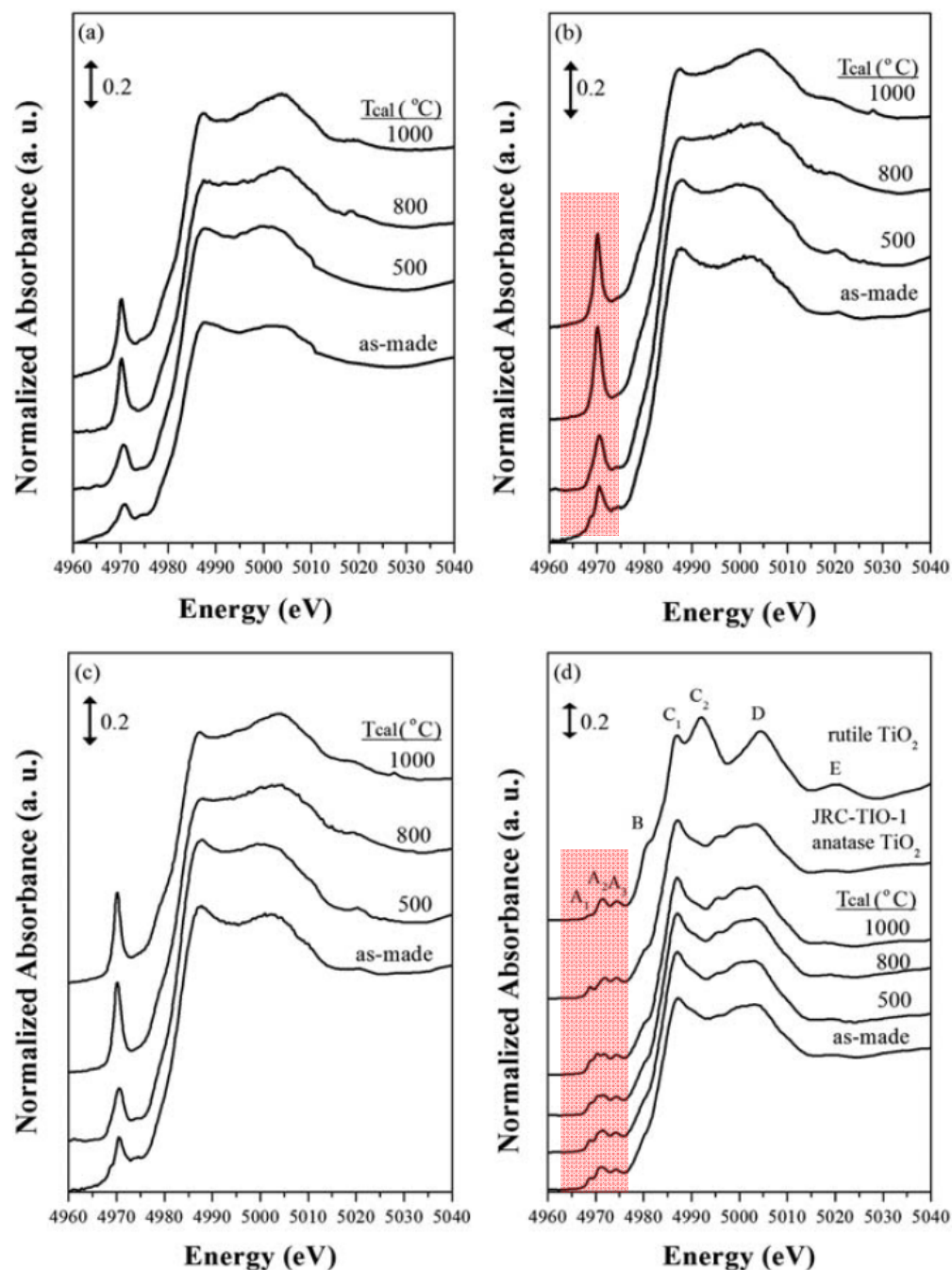
Fig. 6 Ti *K*–edge XANES spectra of the as-made and 500–1000 °C calcined **Ti–SBA-15 materials** with various Ti/Si ratios of (a) 0.01, (b) 0.05, (c) 0.1 and (d) 0.2, in comparison to anatase and rutile TiO_2.

$E_k = h\nu - E_b$
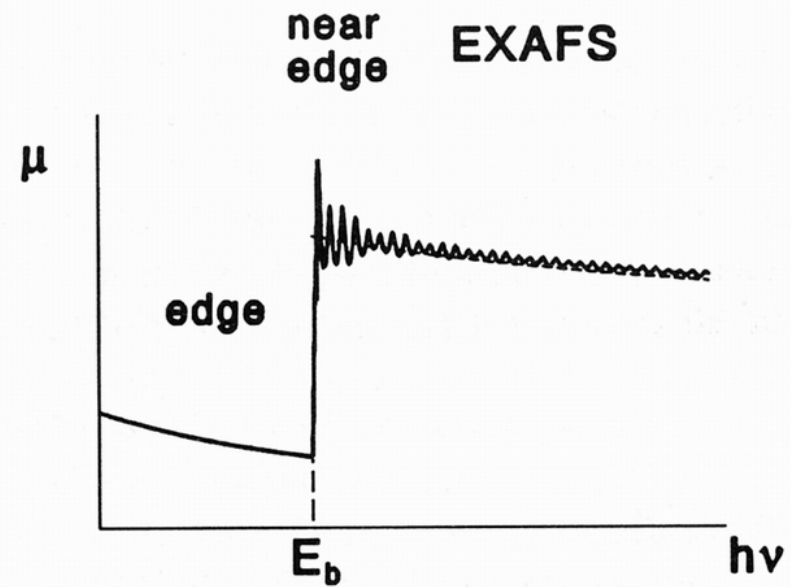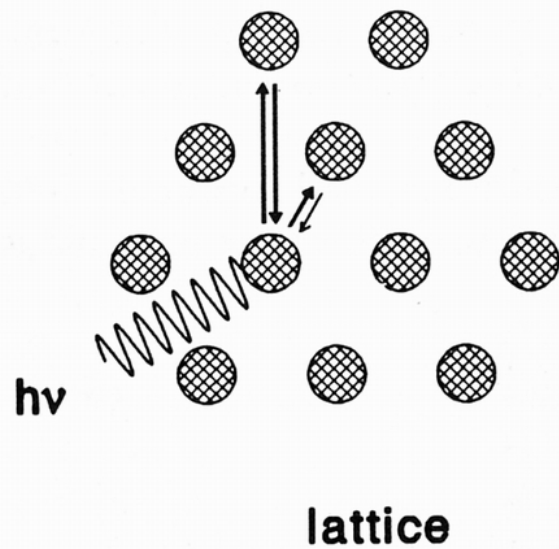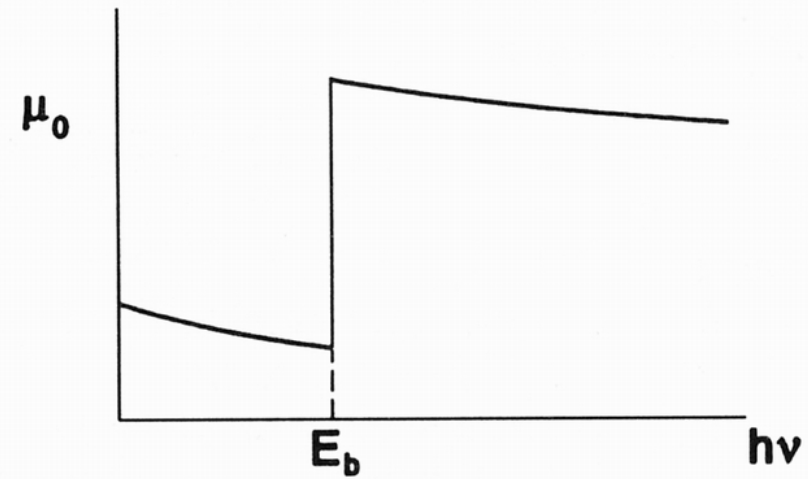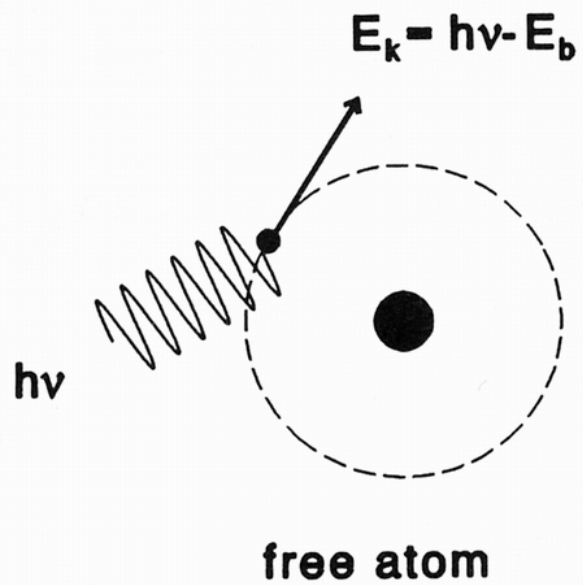
free atom

lattice

Figure 6.12: Absorption of X-rays as a function of photon energy $E = h\nu$ by a free atom and by atoms in a lattice. The fine structure represents the EXAFS function.

98
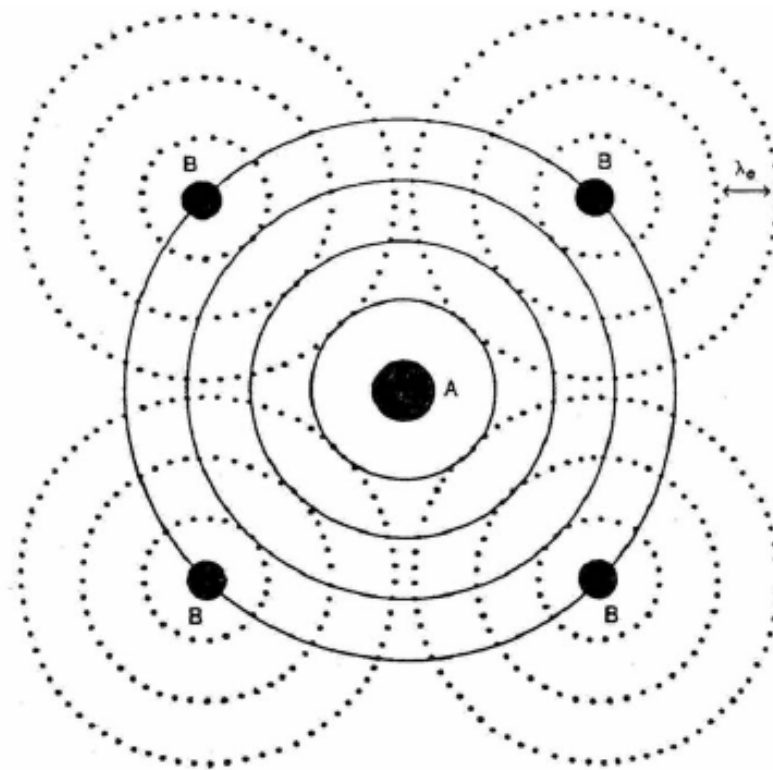
Schematic diagram of the backscattering process. Solid and dotted circles represent wave fronts of outgoing (from A) and backscattered (from B) waves at intervals of the photoelectron wavelength λ_e.
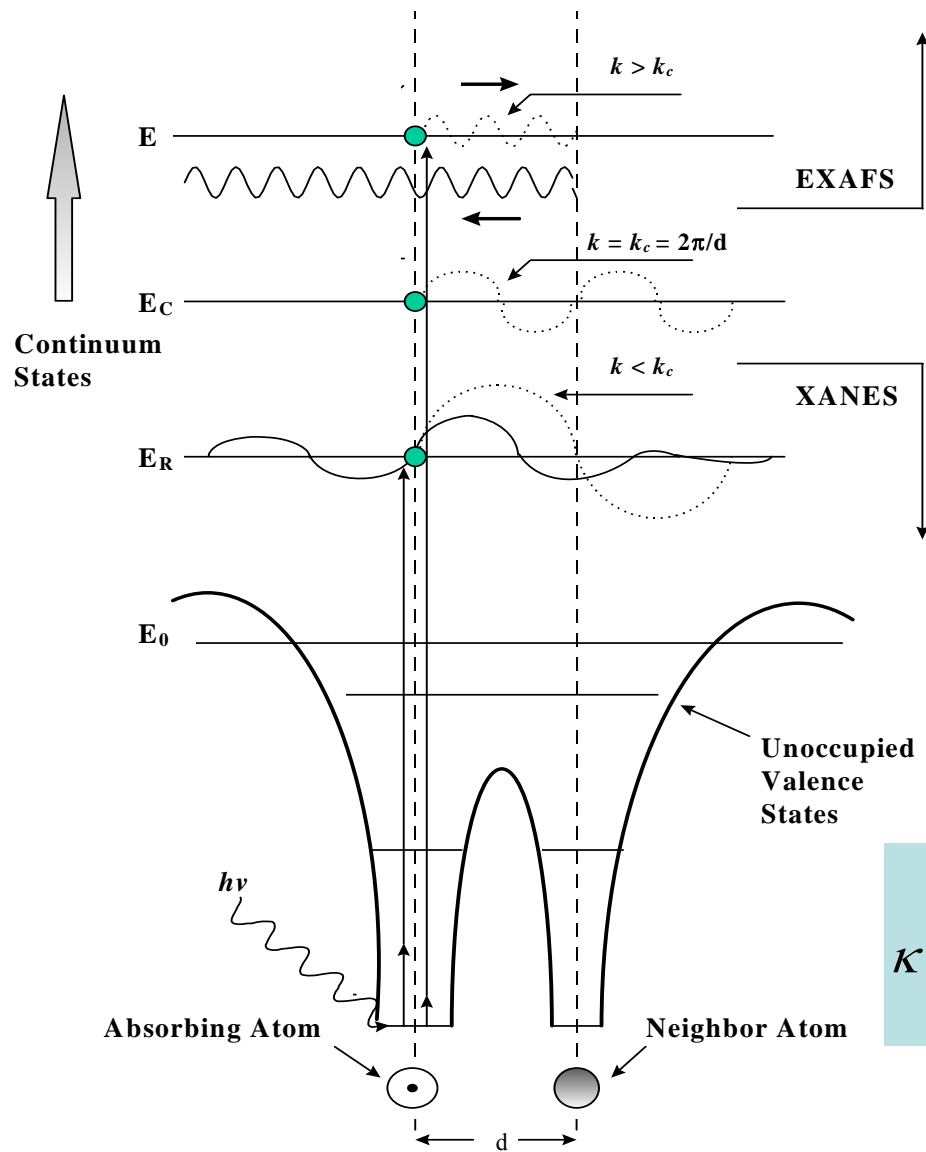
$$E_k = h\nu - E_b = \frac{1}{2}mv^2$$

de Broglie eq.

$$\lambda = \frac{h}{mv} = \frac{h}{\sqrt{2m(h\nu - E_b)}}$$

photoelectron wave vector

$$\kappa = \frac{2\pi}{\lambda} = \left[\left(\frac{8\pi^2 m}{h^2}\right)E_k\right]^{\frac{1}{2}} = \sqrt{\left(\frac{8\pi^2 m}{h^2}\right)(h\nu - E_{edge})}$$

$$\kappa = \frac{2\pi}{\lambda} = \left[\left(\frac{8\pi^2 m}{h^2} \right) E_k \right]^{\frac{1}{2}} = \sqrt{\left(\frac{8\pi^2 m}{h^2} \right) \left(h\upsilon - E_{edge} \right)}$$

m = mass of electron

When the unit of E_k is eV, $\kappa = [0.2625(E-E_0)]^{1/2}$

EXAFS function

$$\chi(E) = \left[\mu(E) - \mu_0(E) \right] / \mu_0(E)$$

μ : measured absorption coeff.
μ_0: no EXAFS

In EXAFS region

Kronig structure – reflected the local structure surrounding the atom under study

Usually taking the spectra 50 – 1000 eV above adsorption edge, then subtract the background, and obtain the spectrum of χ (k) vs. K
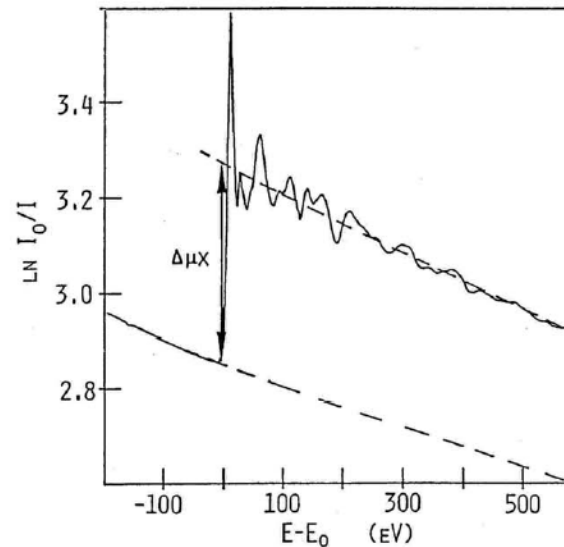
Fig. 6 Illustration of procedure for subtracting the pre-edge and post-edge backgrounds and dividing by the edge jump. The spectrum is measured at Ni K-edge using NiO as the sample.

$$\chi(\kappa) = \sum_j \frac{N_j}{\kappa \cdot R_j^2} \sin\left(2\kappa \cdot R_j + 2\delta + \phi_j\right) \cdot \left|f_j(\kappa)\right| \cdot \exp(-2\sigma_j^2 \kappa^2)$$

$$\cdot \exp\left(\frac{-2V_i R_j}{\kappa}\right)$$

$\kappa \, \alpha \, \sqrt{2E}$ photoelectron wave vector

δ : phase shift of emitting atom

φ_j: phase shift of back scattering atom in j[th] shell

$f_j(K)$: amplitude of the back scattering factor

$\sigma_j{}^2$: Debye-Waller factor → the mean square fluctuation of the interaction distance

v_i: inelastic scattering of photo-electron wave

N_j: coordination no. of jth shell

R_j: interatomic distance of jth shell
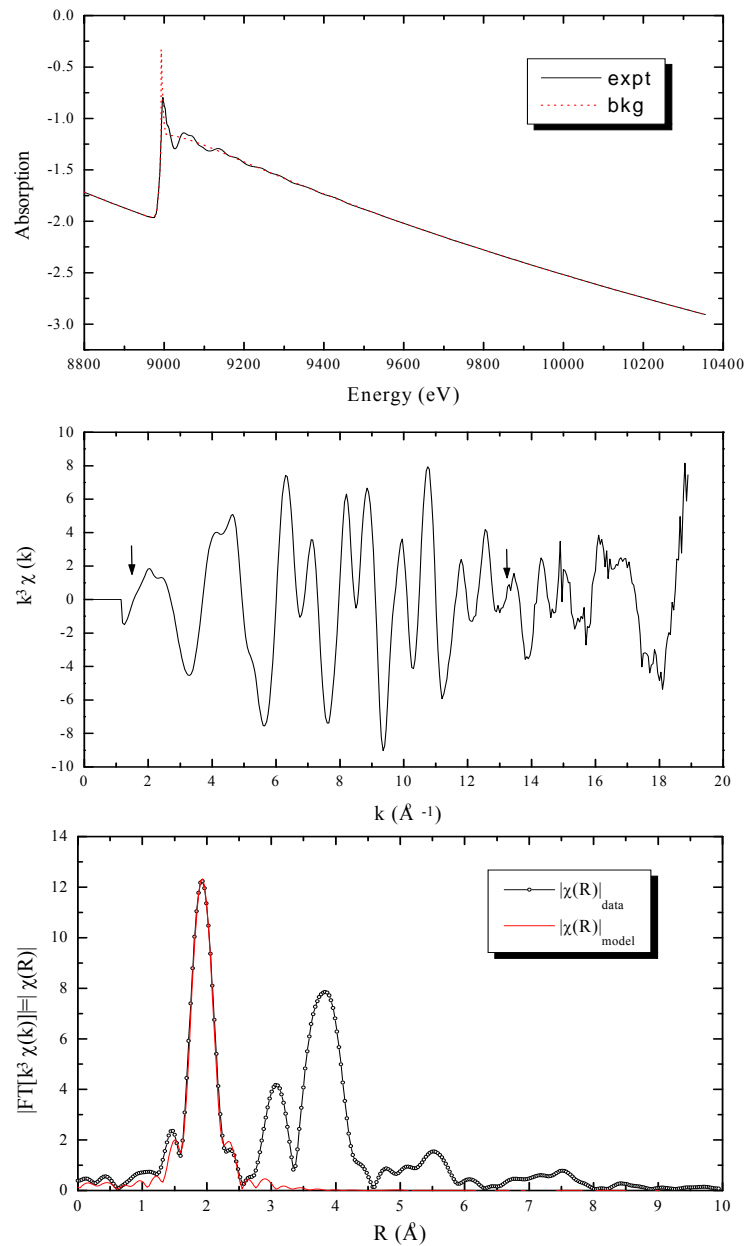
EXAFS

$$\chi(k) = \sum_j \frac{N_j S_0^2(k) F_j(k)}{kR_j^2} \sin[2kR_j + \delta_j(k)] e^{-\frac{2R_j}{\lambda}} e^{-2k^2\sigma_j^2}$$

原始實驗數據

去除不正常的數值點

扣除背景值及規一化

傅立葉轉換

r < 1 Å 之振幅

在r空間進行曲線配適

傅立葉濾波

在k空間進行曲線配適
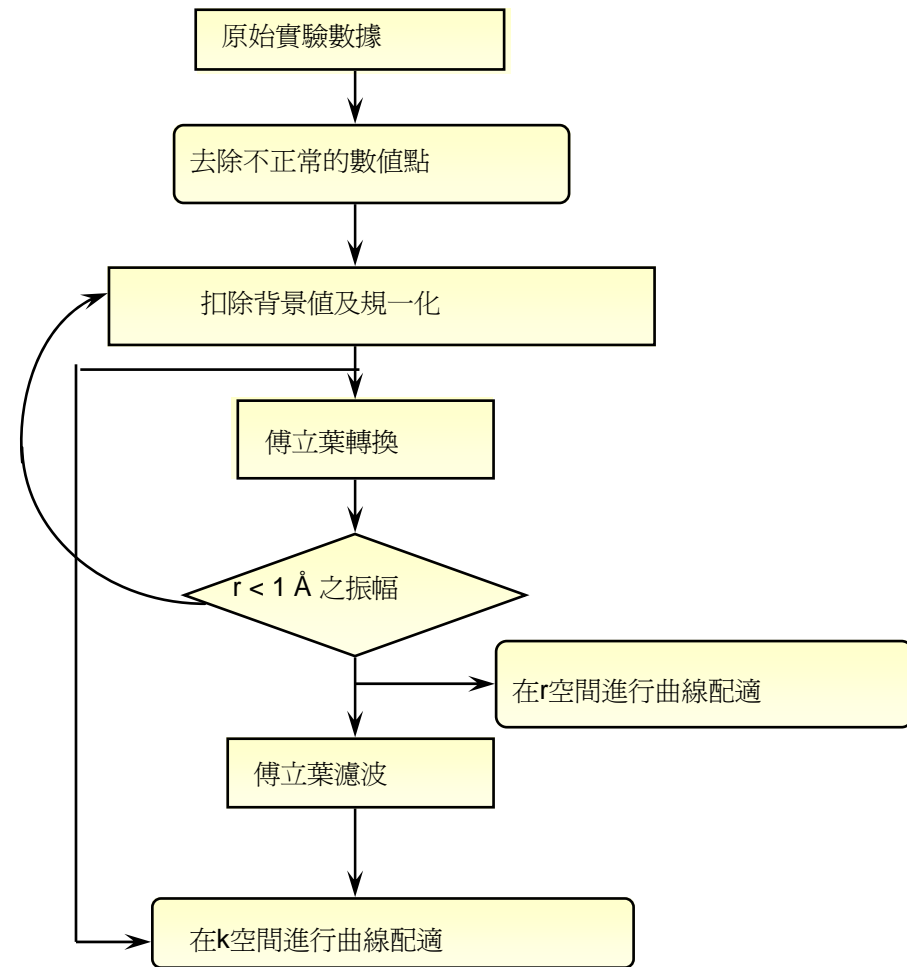
Structural Parameters from EXAFS Analysis

Structural parameter	Accuracy	Observable spectral features
bond length (interatomic distance)	±1%	frequency
coordination number	±20%	magnitude
type of coordination atoms	±4 (in atomic no.)	amplitude envelope and phase shift
Debye-Waller factor $(\sigma^2 = \sigma_s^2 + \sigma_t^2)$	±20% (?)	oscillation damping speed

EXAFS simulation provides informations on
(i) R_j: accurcy ± 0.01 ~ 0.05 Å for the 1st & 2nd shell
(ii) N_j: ± 20% for the 1st shell
(iii) σ_j^2: as small as possible
(iv) r: deviation factor (as small as possible)
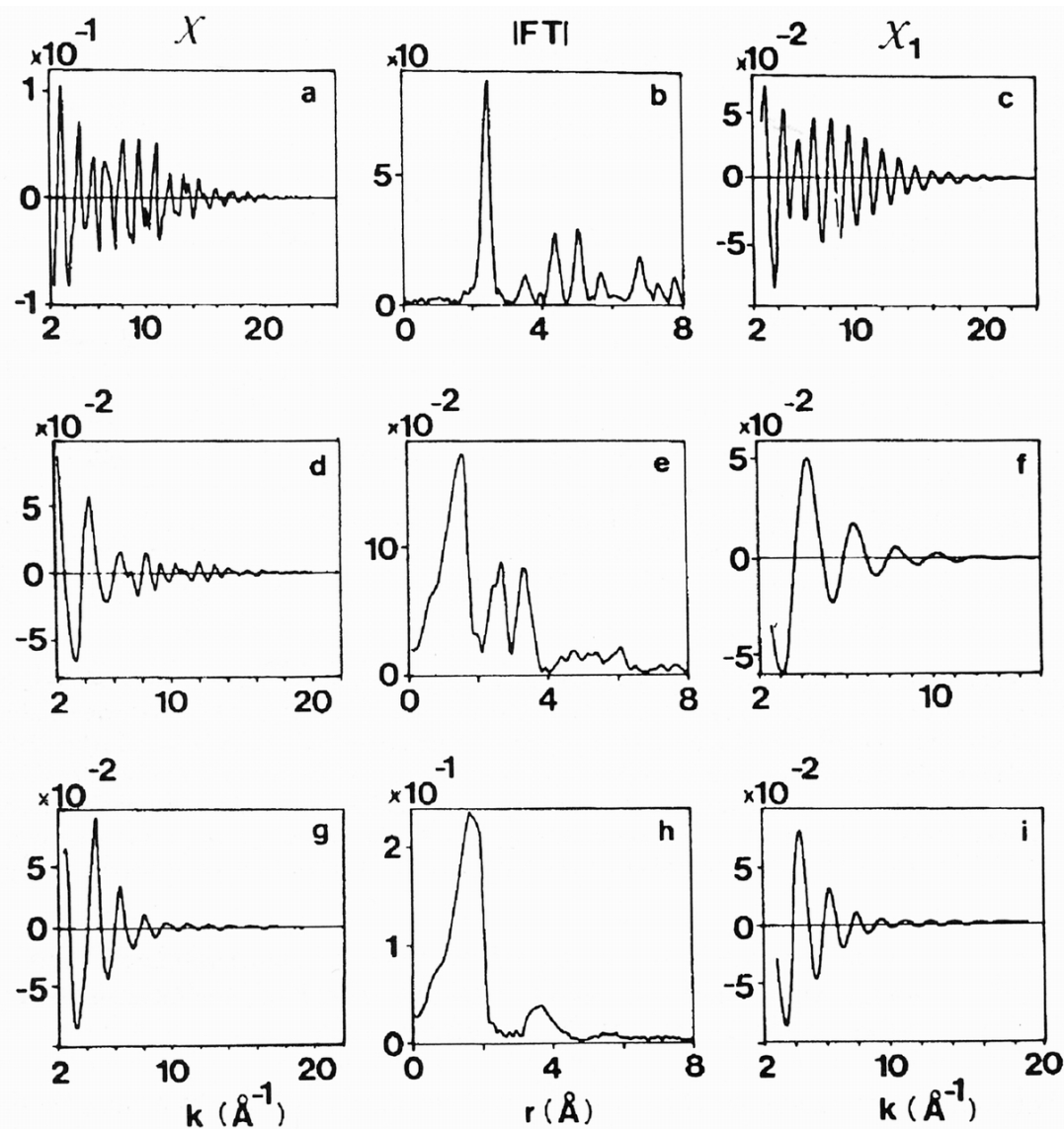
Rh metal

Rh$_2$O$_3$

RhCl$_3$

Figure 6.14: Rh K-edge EXAFS spectra, uncorrected Fourier transforms according to (6-10) and isolated EXAFS contribution from the first neighbour shell of Rh metal (top), Rh$_2$O$_3$ (middle) and RhCl$_3$. The first shell contributions clearly reflect the different backscattering properties of Rh, O and Cl atoms. Note the high number of coordination shells that are visible in Rh bulk metal (from van Zon et al. [27]).

106

Hydrogen Chemisorption and EXAFS Results of Rh, Ir and Pt Nano-Particles Supported on Alumina

Catalyst	Reduction Temp. (K)	H/M	N
4.2% Pt/Al$_2$O$_3$	1100	0.23	10.0
4.2% Pt/Al$_2$O$_3$	1058	0.43	10.2
4.2% Pt/Al$_2$O$_3$	573	0.77	7.6
1.06% Pt/Al$_2$O$_3$	673	1.14	5.2
2.00% Rh/Al$_2$O$_3$	673	1.2	6.6
2.4% Rh/Al$_2$O$_3$	473	1.2	6.3
1.04% Rh/Al$_2$O$_3$	773	1.65	5.8
0.47% Rh/Al$_2$O$_3$	773	1.7	5.1
0.57% Rh/Al$_2$O$_3$	573	1.98	3.8
7.0% Ir/SiO$_2$	773	0.43	11.1
1.5% Ir/SiO$_2$	773	0.83	11.0
5.3% Ir/SiO$_2$	773	1.24	8.6
1.5% Ir/SiO$_2$	773	1.70	8.6
2.4% Ir/Al$_2$O$_3$	773	1.96	7.7
1.5% Ir/Al$_2$O$_3$	773	2.40	7.3
0.8% Ir/Al$_2$O$_3$	773	2.68	6.0

Coordination Number

Liquid phase pinacol pearrangement of 2,3-dimethyl-2,3-butandiol
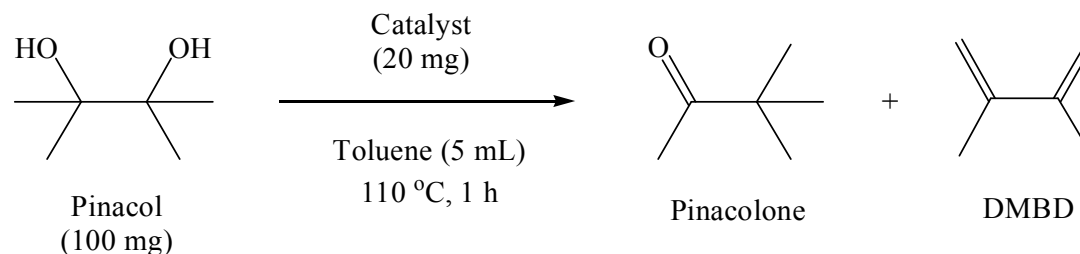
Catalyst	M/Si[a]	NH$_3$-TPD Peak Area Ratio	Conv. (%)	Pinacolone	
				Yield (g/g catal·h)	Select. (%)
None	-	-	0	0	0
Si-SBA-15	-	0.014	0.7	0	0
ZSM-5	0.0087	0.23	6.0	0.1	46
HY-zeolite	0.38	1.0	15	0.5	80
ImZr-SBA-15	0.03	n.d. [b]	0	0	0
	0.10	n.d.	0.5	0	0
Zr-SBA-15	0.017	0.024	8.6	0.2	61
	0.029	0.12	26	0.8	80
	0.044	0.17	54	1.7	79
	0.059	0.21	69	2.2	78
	0.11	0.36	82	2.7	81
Reg-Zr-SBA-15	0.11	0.36	80	2.6	82

[a] M/Si = metal to Si molar ratio. [b] Not detectable.

Pinacol conversions and acidities of Zr–SBA-15 materials as a function of Zr contents
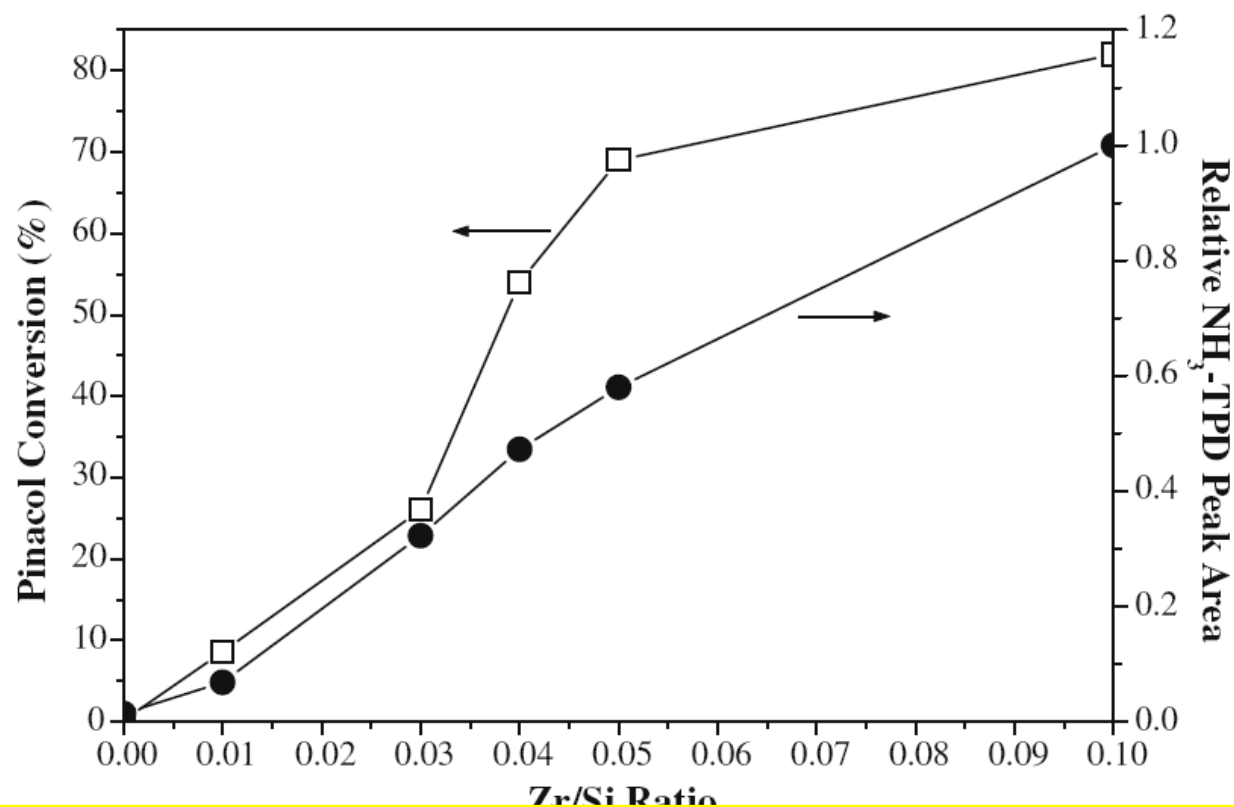
Zr-SBA-15 materials with Zr/Si > 0.03 were the most efficient catalysts!

Zr K-edge X-ray absorption spectroscopy
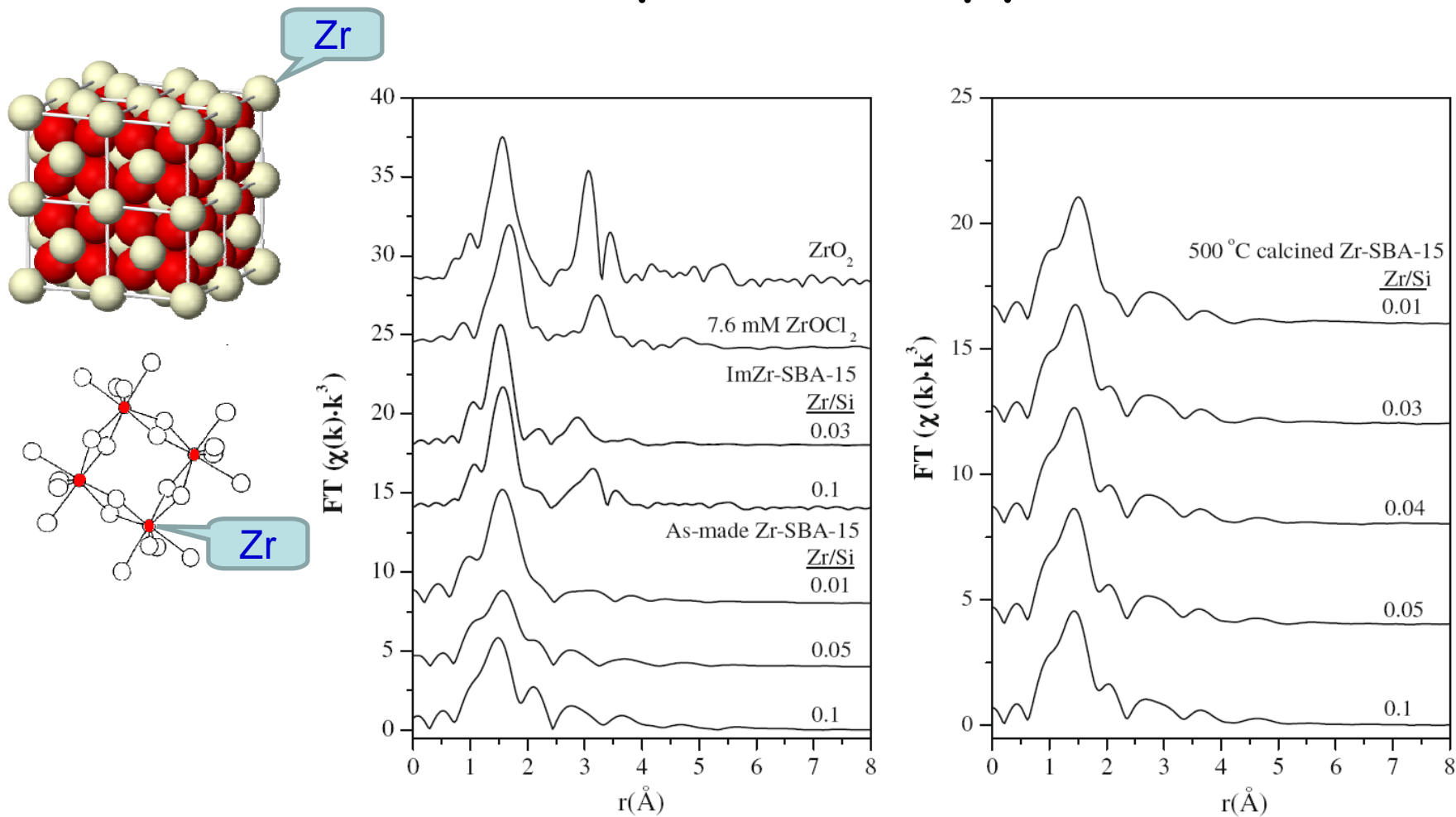
Proposed reaction mechanism of pinacol rearrangement over **Zr–SBA-15** materials
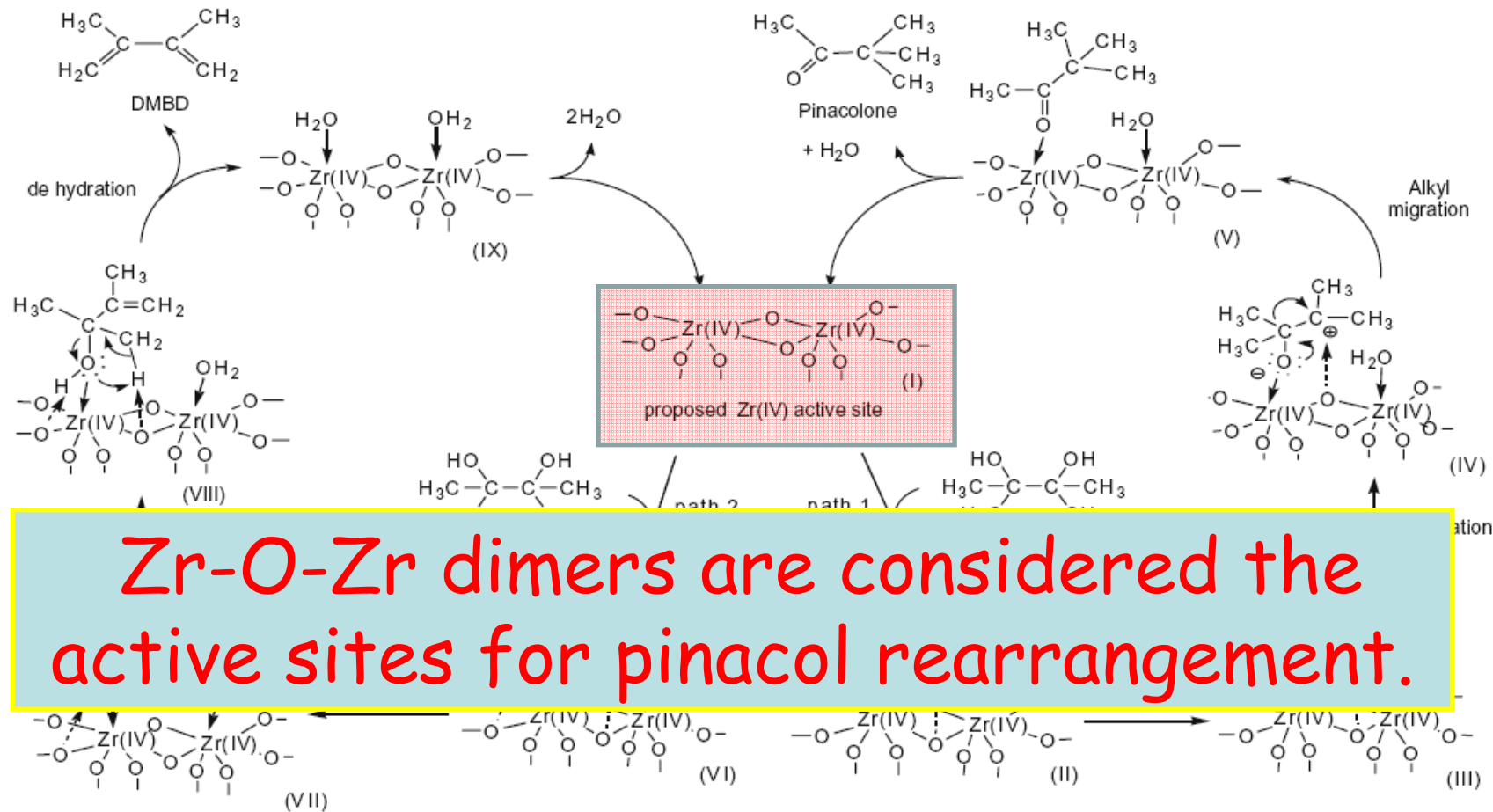
Zr-O-Zr dimers are considered the active sites for pinacol rearrangement.

Techniques for characterization of nano-porous materials

Crystalline structure

- Single crystal & Powder X-ray diffraction (XRD)
- Electron crystallography

Surface area & Pore size

- N_2 adsorption-desorption isotherm
- Mercury Intrusion Porosimetry

Pore structure- TEM

Morphology- SEM

Oxidation state & Coordination

- X-ray absorption spectra
- X-ray photoelectron spectra (XPS & Auger)
- Solid state NMR (mainly coordination)
- IR & Raman (mainly coordination)
- UV-Vis spectra

Elemental analysis- ICP-AES, XPS, EDX

- ## High resolution NMR spectra of solids

A general Hamiltonian for the interactions experienced by a nucleus of spin I

eigenvalue

$$H\psi = E\psi$$

Hamiltonian

Wave function

$$H = H^Z + H^{RF} + H^D + H^J + H^{CS} + H^Q + H^{SR}$$

external Hamiltonian   internal Hamiltonian

H^Z: Zeeman interaction of the nuclear magnetic moment
with the applied field B_0

H^{RF}: interaction between nuclear spin & the time-dependent
radio freq. field $B_1(t)$

not important
in solid $\quad$ H^D: dipolar interaction between nuclear magnetic dipole moments

H^J: e⁻mediacted nuclear spin-spin interaction

H^{CS}: chemical shift associated with electronic screening of nuclei

H^{SR}: spin-rotation interaction; I and molecular angular momentum

H^Q: nuclear spin & quadruple moment

important
for I > 1/2

113

A general Hamiltonian for the interactions experienced by a nucleus of spin I in the solid state may be written as in equation (1.2)

$$H = H_Z + H_D + H_{CS} + H_{SC} + H_Q \qquad (1.2)$$

Table 1.1 Approximate ranges of the different spin interactions (in Hz)

Zeeman	$10^6 \sim 10^8$
Dipolar	$0 \sim 10^5$
Chemical Shift	$0 \sim 10^5$
Scalar Coupling	$0 \sim 10^4$
Quadrupolar	$0 \sim 10^9$

Zeeman interaction

$$H_Z = -\vec{\mu} \cdot \vec{H}_0 = -\left|\mu\right|\left|H_0\right|\cos\theta = -\mu_Z H_0$$

$$H_Z = -\gamma\hbar H_0 I_z = -g_N \beta_N H_0 I_Z$$

$$\mu = \gamma I \hbar = g_N \beta_N I$$

$$= g_N \left(\frac{e\hbar}{2m_P C} \right)$$

nuclear g factor

Bohr magneton of the particular nucleus
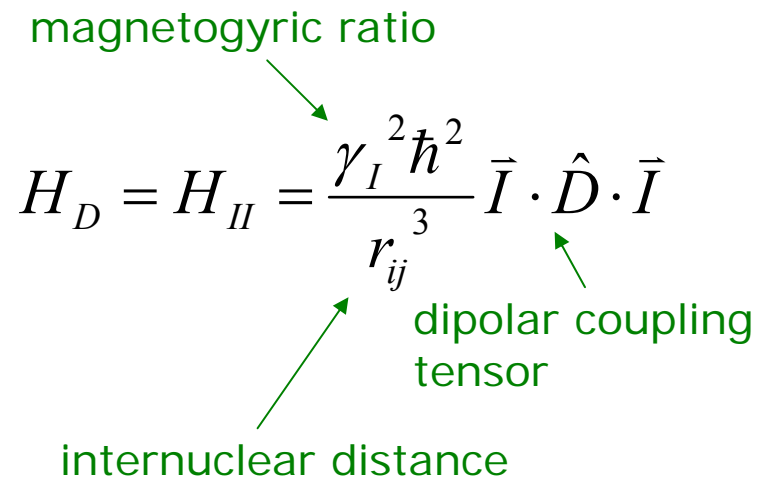
magnetogyric ratio

Dipolar interaction H$_D$

For single type of spin, I

magnetogyric ratio

$$H_D = H_{II} = \frac{\gamma_I^{\,2}\hbar^2}{r_{ij}^{\,3}} \vec{I} \cdot \hat{D} \cdot \vec{I}$$

dipolar coupling tensor

internuclear distance

<u>Chemical shift interaction</u>

$$H_{CS} = \gamma_I \hbar \vec{I} \cdot \hat{\sigma} \cdot \vec{H}_0$$ Proportional linearly to the applied field

Table. Typical values of chemical shift

<u>necleus</u>	<u>Range of common isotropic chemical shift (ppm)</u>
^{1}H	20
^{13}C	250
^{15}N	350
^{19}F	100
^{29}Si	80
^{31}P	200

Spin-spin coupling interaction

$$H_{SC} = \vec{I} \cdot \hat{J} \cdot \vec{S}$$

field independent and is usually smaller than the other interaction

Quadrupolar interaction

nuclear electric quadrupole moment eQ

$$H_Q = \vec{I} \cdot \hat{Q} \cdot \vec{I}$$
only when I > ½
field independent

Table 1.2. NMR parameters and relative detectability of some common nuclei.

Nucleus	$\gamma/2\pi$ (MHz/ Telsa)	Frequency (MHz at field of 4.7T)	Spin (Units of $\hbar$)	Quadrupole Moment	Relative nuclear signal	Isotopic natural abundance (%)	Relative natural abundance signal
^{1}H	42.57	200.00	1/2	-	1.0	99.98	1.0
^{2}H	6.54	30.70	1	2.8×10^{-3}	0.025	0.016	4.0×10^{-6}
^{11}B	13.66	64.17	3/2	3.55×10^{-2}	0.29	81.2	0.24
^{13}C	10.71	50.29	1/2	-	0.032	1.1	3.5×10^{-4}
^{14}N	3.08	14.45	1	1.93×10^{-2}	3.8×10^{-3}	99.64	3.8×10^{-3}
^{15}N	4.31	20.27	1/2	-	3.3×10^{-3}	0.37	1.2×10^{-5}
^{17}O	5.77	27.11	5/2	-2.6×10^{-2}	0.079	0.037	2.9×10^{-5}
^{19}F	40.06	188.15	1/2	-	0.86	100	0.86
^{27}Al	11.09	52.11	5/2	0.149	0.40	100	0.40
^{29}Si	8.46	39.73	1/2	-	0.018	4.7	8.5×10^{-4}
^{31}P	17.24	80.96	1/2	-	0.10	100	0.10
^{195}Pt	9.15	42.00	1/2	-	0.021	33.7	7.1×10^{-3}

ZEEMAN   QUADRUPOLAR

+1

ν ν_1

0

ν ν_2

-1
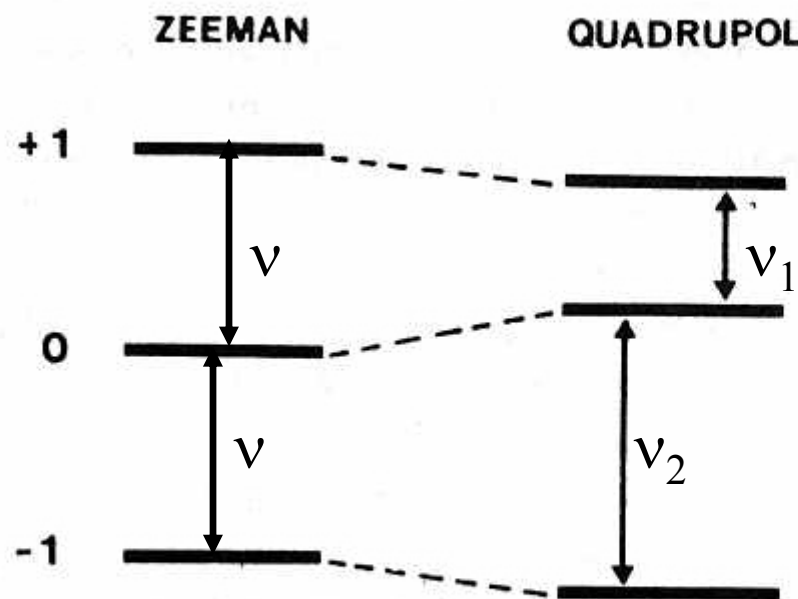
FIGURE 3.1 Schematic representation of the energy levels of a spin I nucleus resulting from the Zeeman interaction with the magnetic field and with the quadrupole moment of the nucleus.

Dipolar Interaction

$$H_D = -\sum_{i<j} g_N^2 \beta_N^2 \frac{1}{r^3_{ij}}(1 - 3\cos^2\theta_{ij})(\vec{l_i}\cdot\vec{l_j} - 3l_{iz}l_{jz}) \qquad (4.2)$$

$$H_D = -\frac{1}{2}\left(\boxed{3\cos^2\theta_{ij} - 1}\right)\sum_{i<j} g_N^2 \beta_N^2 \frac{1}{r^3_{ij}}(1 - 3\cos^2\gamma_{ij}) \qquad (4.3)$$

$H_D = 0$, if $3\cos^2\theta_{ij} - 1 = 0$

FIGURE 4.1 Schematic representation of the geometric arrangement for mechanical sample spinning.

Magic Angle Spinning

(MAS)

A

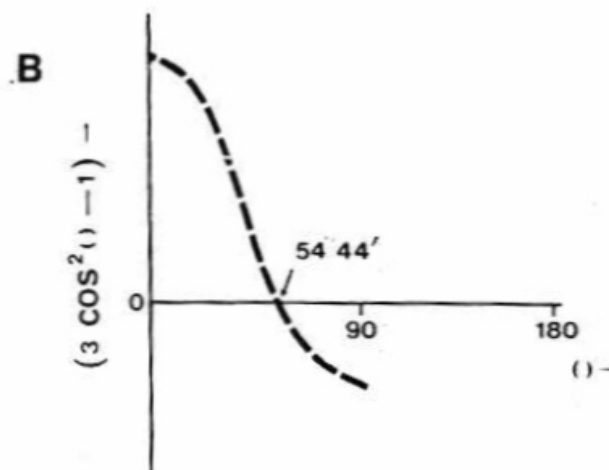**B**

$(3 \cos^2() - 1)$

54 44'

0   90   180

() →
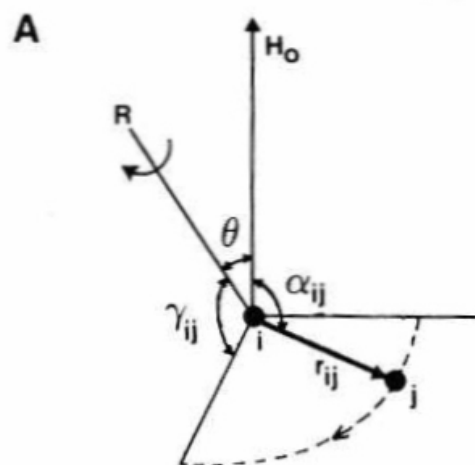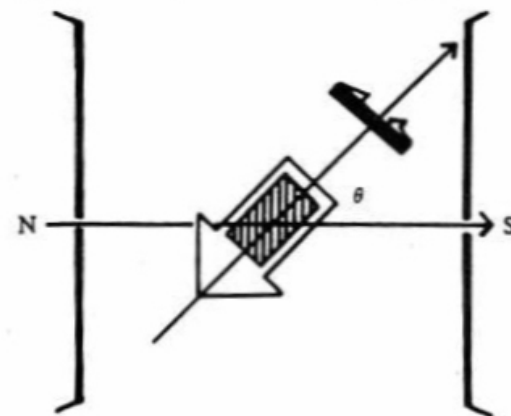
FIGURE 4.2 (A) Definition of the angles used in equation (4.3) to describe the effect of fast sample spinning on the dipolar interaction. The solid specimen is rotated about the axis R inclined at angle θ to H_o. A typical vector r_{ij} joining nuclei i and j is inclined at angle τ_{ij} to the rotation axis; its inclination to H_o varies periodically with time. (Adapted from reference 4 and reproduced by permission of Butterworth Scientific Ltd.). (B) Variation of the term $(3 \cos^2 \theta - 1)$ as a function of θ. The curve crosses the axis at θ = 54° 44'.

121

FIGURE 4.3 ^{19}F NMR spectra of polycrystalline K$^+$PF$_6{}^-$ 1 (A) Static specimen; (B) With MAS specimen spinning at 8 kHz revealing a doublet due to J coupling between ^{19}F and ^{31}P nuclei. (Reproduced by permission of The Royal Society, London, from reference 11 after reference 20).
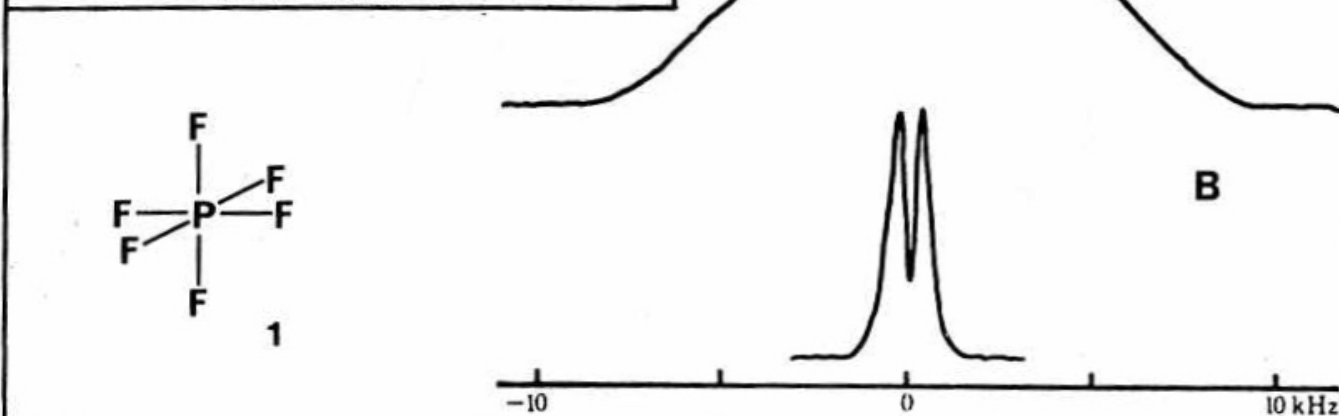
FIGURE 4.4 ^{19}F NMR spectra of polycrystalline K$^+$AsF$_6{}^-$ 2 (A) Static specimen (B) specimen spinning at 5.5 kHz, displaying quartet structure due to J coupling between ^{19}F and ^{75}As nuclei. (Reproduced by permission of The Royal Society, London, from reference 11 after reference 21).

122
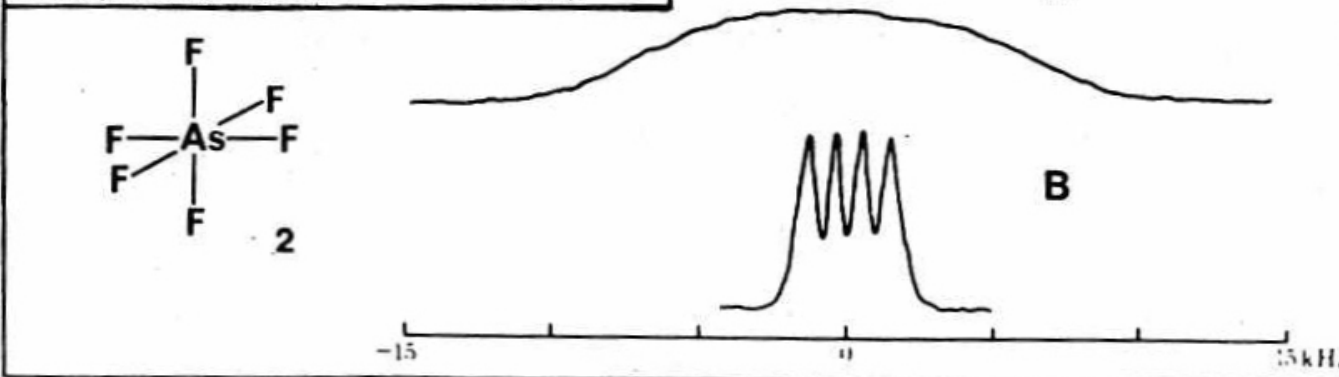
FIGURE 7.42 CP-MAS spectra of the reaction product of $(CH_3)_3SiCl$ with silica gel: (A) ^{13}C spectrum; (B) ^{29}Si spectrum. (The peaks at higher fields are due to the support (see Figures 7.43, 7.44). (Reproduced by permission of Elsevier Scientific Publishing Co., Amsterdam, from reference 146a).

123

FIGURE 7.44   ²⁹Si NMR spectra of Fisher S-157 silica gel (A) before and (B) after reaction with trimethylchlorosilane. Chemical shift scale is in ppm with respect to liquid Me₄Si, with larger numbers corresponding to lower shielding. (Reproduced by permission of the American Chemical Society, from reference 151, cf. Figure 7.42).

124

FIGURE 7.24 ^{29}Si chemical shift ranges of aluminosilicates. Si(nAl) designates the SiO_4 tetrahedron connected through shared oxygen atoms with $nAlO_4$ tetrahedra in the aluminosilicate framework. The dashed lines show the shift values of zeolite ZK-4 as indicated. The inner boxes are the original ranges (ref. 61a) while the outer ones reflect more recent data. (Reproduced by permission of Verlag Chemie GMBH, Germany, from reference 60 after reference 61a).

FIGURE 7.25 Observed and theoretical ^{29}Si MAS NMR spectra of a series of faujasite zeolites of varying Si/Al ratios calculated from Equation 7.8. (Reproduced by permission of The Royal Society of Chemistry, London, adapted from reference 65).

Si/Al

1.19
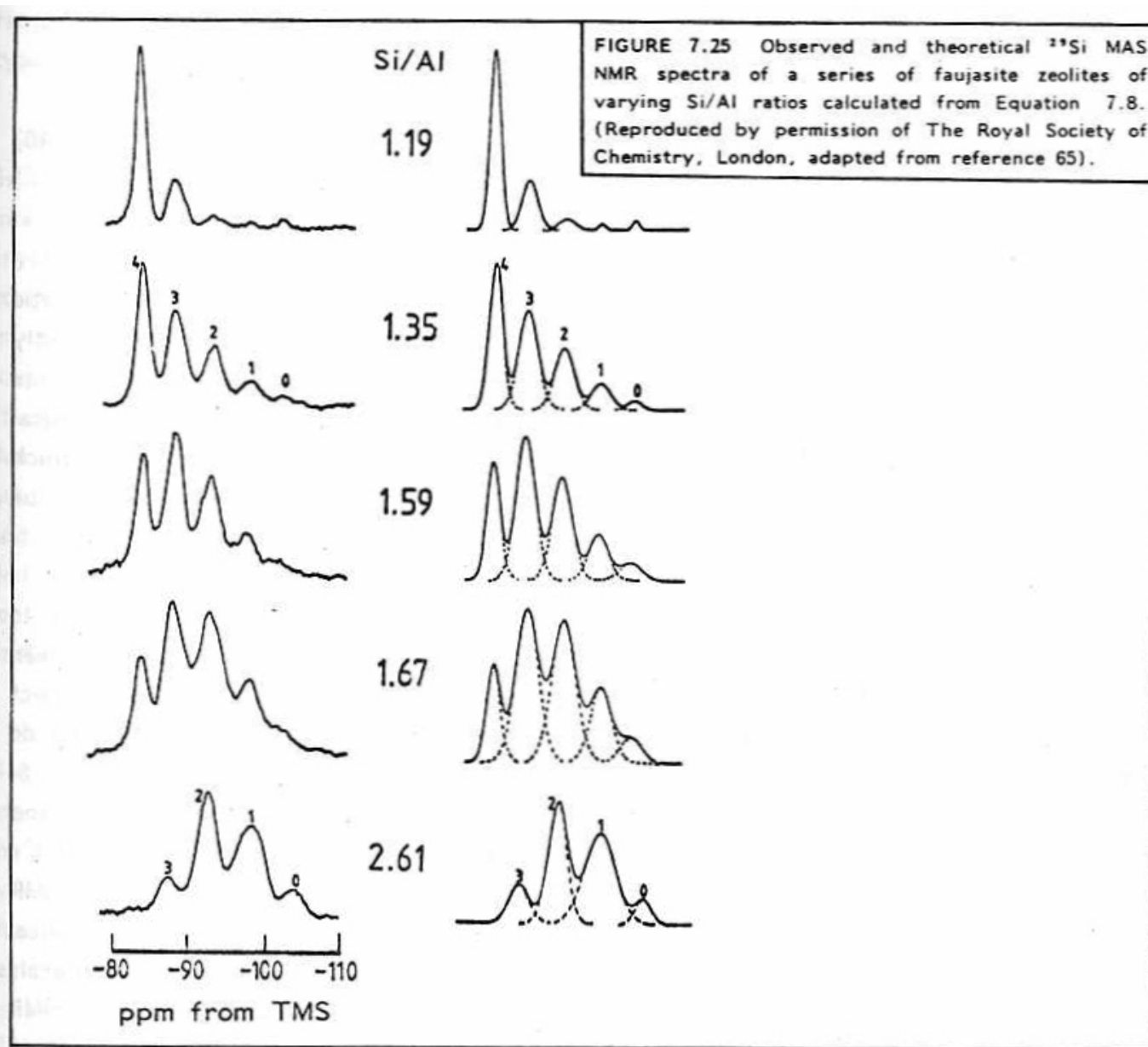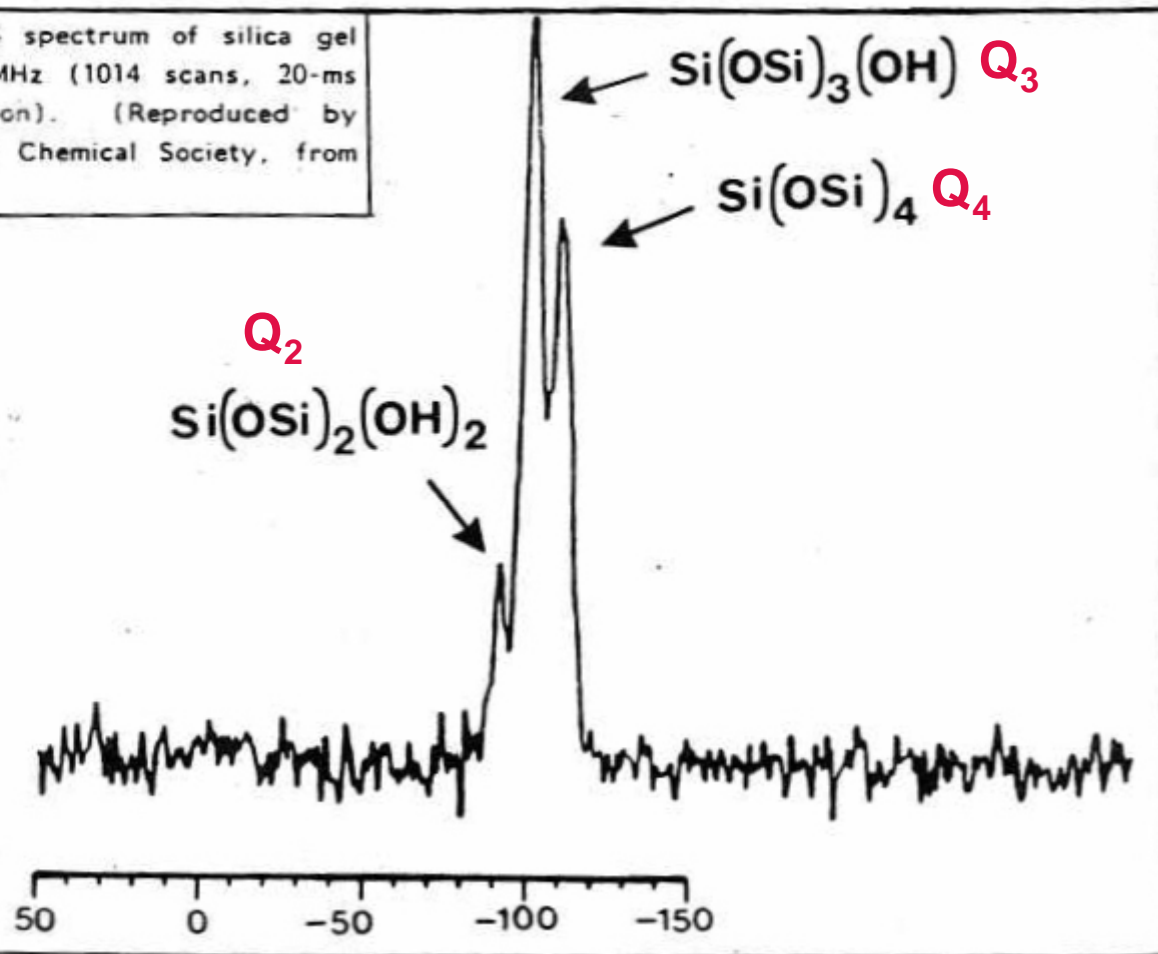
1.35

1.59

1.67

2.61

-80   -90   -100   -110

ppm from TMS

FIGURE 7.43 ^{29}Si CP/MAS spectrum of silica gel (SG-2) obtained at 11.88 MHz (1014 scans, 20-ms contact time, 1-s repetition). (Reproduced by permission of the American Chemical Society, from reference 150).
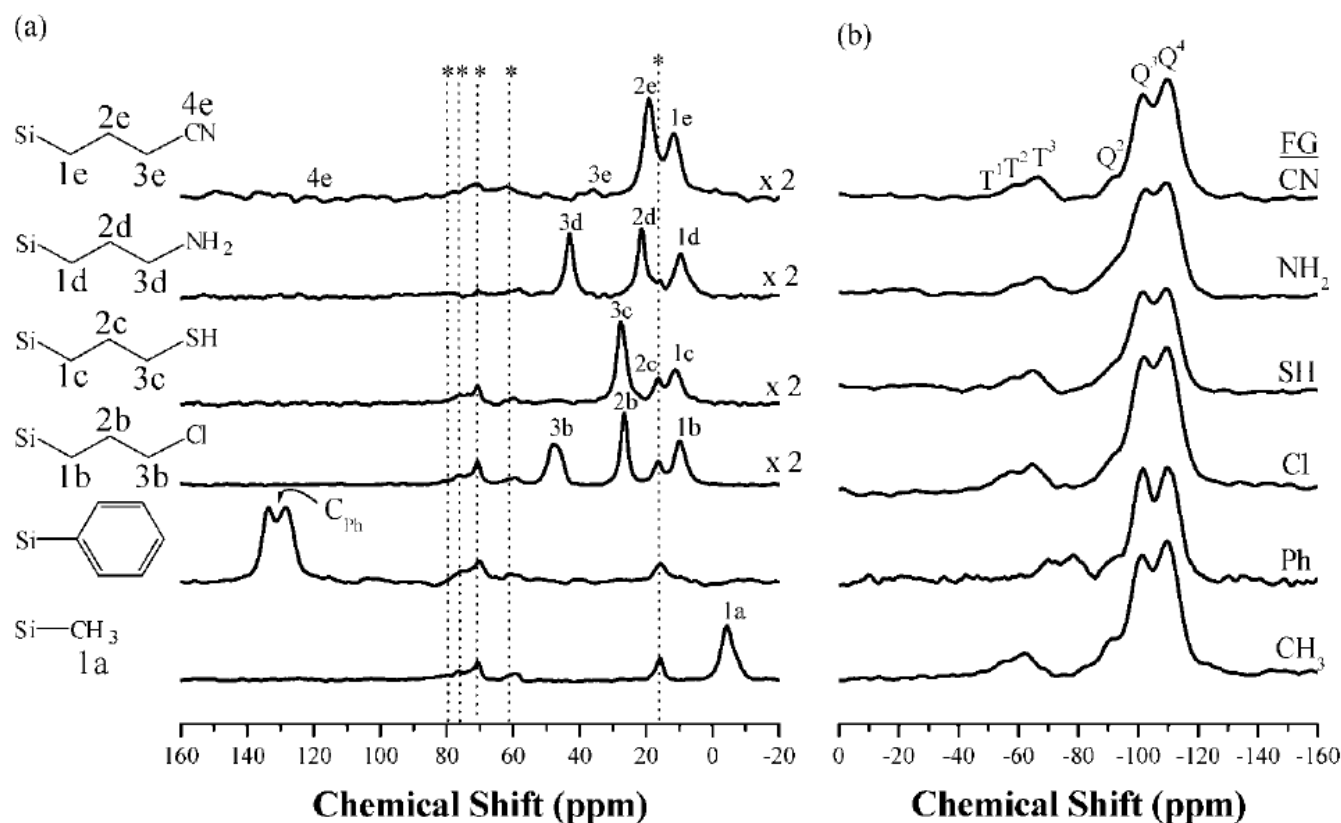
$Si(OSi)_3(OH)$ Q_3

$Si(OSi)_4$ Q_4

Q_2

$Si(OSi)_2(OH)_2$

50   0   −50   −100   −150

Figure 10. (a) Solid-state ^{13}C CP-MAS spectra and (b) ^{29}Si MAS NMR spectra of various extracted organic functionalized SBA-15 with platelet morphology and short mesochannels; Peaks labeled * correspond to carbon atoms from the P123 residue.

Chen et al. Chem. Mater. **2008, 20, 3906–3916**

There are still a huge SPACE in the research of nano-porous materials.